Compact squeezed-light source at 1550 nm

Dissertation
zur Erlangung des Doktorgrades
an der Fakultät für Mathematik, Informatik und Naturwissenschaften
Fachbereich Physik
der Universität Hamburg

vorgelegt von

Axel Schönbeck

Hamburg

2018

Gutachter der Dissertation:	Prof. Dr. Roman Schnabel Prof. Dr. Henning Moritz
Zusammensetzung der Prüfungskomission:	Prof. Dr. Roman Schnabel Prof. Dr. Henning Moritz Prof. Dr. Daniela Pfannkuche Prof. Dr. Günter Huber Prof. Dr. Ludwig Mathey
Vorsitzende der Prüfungskommission:	Prof. Dr. Daniela Pfannkuche
Datum der Disputation:	19.07.2018
Vorsitzender des Fach-Promotionsausschusses PHYSIK:	Prof. Dr. Wolfgang Hansen
Leiter des Fachbereichs PHYSIK:	Prof. Dr. Michael Potthoff
Dekan der Fakultät MIN:	Prof. Dr. Heinrich Graener

Kurzfassung

Gequetschte Zustände des Lichts haben in den vergangenen Jahren in einer Vielzahl von Anwendungen im Bereich der Quantenoptik Verwendung gefunden.
Dazu zählen Graviationswellendetektion [Aas13] [Aba11] [Gro13], Quantenschlüsselverteilung [Geh15], Messungen in der Biologie [Tay13], die Radiometrie zur absoluten Kalibration von Photodioden [Vah16] und die Bestimmung der Linienbreite von Resonatoren [Mik06].
Die Quellen zur Erzeugung von gequetschtem Licht sind in der Vergangenheit ausgereifter geworden, wobei immer höhere Quetschfaktoren erzielt wurden [And16]. Nachdem der erste experimentelle Nachweis gequetschten Lichts einen Quetschfaktor von 0.3 dB aufwies und mit Hilfe von Vier-Wellen-Mischung in Natrium Atomen erzielt wurde [Slu85], erreichte ein auf parametrischer Abkonversion basierender Versuch kurz danach bereits 3 dB [Wu86]. Über zwanzig Jahre später wurden erstmalig 10 dB nachgewiesen, ebenfalls mit Hilfe von parametrischer Abkonversion [Vah08b]. Heute werden Quetschfaktoren von bis zu 15 dB bei 1064 nm erzielt [Vah16]. Um die Integration von gequetschtem Licht in experimentelle Aufbauten zu ermöglichen, wurden entsprechende Regel- und Kontrolltechniken entwickelt [Che07b]. Die vollautomatische Quetschlichtquelle für den Graviationswellendetektor GEO600 wurde auf einem Breadboard von 1.35 m x 1.13 m gebaut und ist damit die weltweit erste portable Quelle ([Kha11], p. 45). Alle übrigen genannten Aufbauten und Experimente wurden in Laboren mit großen optischen Tischen durchgeführt.
Um eine einfachere Anwendung der Quetschlichttechnologie zu ermöglichen, müssen die Aufbauten weiter verkleinert werden. Insbesondere die Wellenlänge von 1550 nm ist als Standartwellenlänge in der Telekommunikation interessant. Diese Überlegungen sind Grundlage und Motivation für die vorliegende Arbeit.
Die im Rahmen dieser Arbeit entworfene und gebaute Quetschlichtquelle wurde auf einem Breadboard von 80 cm x 80 cm realisiert. Über einen externen Faserlaser wurde kohärentes Laserlicht bei 1550 nm zum Betrieb der Quelle eingekoppelt. Mit der Quelle konnte gequetschtes Licht in einem Seitenbandbereich zwischen 1 kHz und 25 MHz nachgewiesen werden, wodurch die Anwendung des Quetschlichts in mehreren Bereichen, zum Beispiel für die Interferometrie, die Radiometrie oder die Quantenschlüsselverteilung, realisiert werden kann. Der Resonator zur parametrischen Abkonversion wurde mit einem Multi-Temperatur-Schema ausgestattet, welches es ermöglicht, unterschiedliche Bereiche des Kristalls unterschiedlich stark zu temperieren. Dies ermöglicht die Einstellung von gleichzeitiger Doppelresonanz und Phasenanpassung im Resonator. Der hier präsentierte Aufbau stellt einen ersten Schritt in der Entwicklung kompakter Quetschlichtquellen bei 1550 nm dar.

Abstract

During the past years, squeezed states of light have become a versatile tool in quantum optics with various applications.
These applications include gravitational-wave detection [Aas13] [Aba11] [Gro13], quantum key distribution [Geh15], experiments in the field of biology [Tay13], the absolute calibration of photo diodes [Vah16] and the measurement of cavity parameters [Mik06].
The sources for squeezed vacuum states have also become more and more mature over time [And16]. The first experimental detection showed a quantum noise reduction of 0.3 dB from four-wave mixing in Na atoms [Slu85]. The first squeezed-light source based on parametric down-conversion already reached 3 dB [Wu86]. More than twenty years later, the milestone of 10 dB was achieved, also based on parametric down-conversion [Vah08b]. Today, it is possible to generate 15 dB at 1064 nm [Vah16].
Apart from work to increase the squeezing strength, technologies like the coherent control scheme to control squeezed states have been developed [Che07b] to enable their integration in experimental setups. The squeezed-light source at 1064 nm for the GEO 600 gravitational-wave detector was the first portable and fully automatic source based on parametric down-conversion set up on a breadboard of 1.35 m x 1.13 m ([Kha11], p. 45) whilst the other results and applications mentioned were demonstrated on tabletop experiments.
To enable a more flexible and widespread application of squeezed states, it is important to reduce the footprint even further and to apply the technology to new wavelengths, especially the telecommunication wavelength of 1550 nm. These requirements motivated the work presented in this thesis.
The squeezed-light source engineered and presented here was set up on a breadboard of 80 cm x 80 cm. Coherent laser light at 1550 nm was injected into the setup via a fiber coupler. This increases the flexibility, since it allows for the usage of the squeezed-light source with existing laser systems. The source produced squeezing in a frequency range from 1 kHz to 25 MHz, which enables its usage in many different applications. In addition, the parametric down-conversion cavity was equipped with a multi-temperature heating scheme, which facilitates the creation of a temperature gradient. This is an approach to adjust the operating point at which simultaneous phase matching and doubly resonance for both the fundamental and second-harmonic field is reached in the cavity. Thus, the setup presented here can be regarded as a first step towards a portable and flexible squeezed-light source at 1550 nm.

Contents

Kurzfassung **i**

Abstract **iii**

1 Introduction **1**

2 Theoretical concepts **5**
2.1 Quantum theory of light 5
2.1.1 Quantization of the electromagnetic field 5
2.1.2 Number states 6
2.1.3 Coherent states 7
2.1.4 Wigner function 8
2.1.5 Minimum uncertainty states 10
2.1.6 Squeezed states 12
2.2 Cavity-enhanced nonlinear processes 14
2.2.1 Second-harmonic generation 15
2.2.2 Squeezing from degenerate parametric down-conversion 18
2.2.3 Effect of optical loss on squeezing 28
2.2.4 Phase matching 31

3 Experimental setup **33**
3.1 Linear filter cavity 36
3.2 Second-harmonic generation and parametric down-conversion cavities . 38
3.2.1 Nonlinear-cavity design 39
3.2.2 Second-harmonic generation 44
3.3 Theory of balanced homodyne detection 47
3.4 Coherent control locking for low frequency squeezing 49

4 Squeezing in the MHz regime **55**
4.1 Detection of 13dB squeezed vacuum states 55
4.2 Spectra and pump power dependence 57
4.3 Loss analysis 59

5 Squeezing in the audioband **63**
5.1 Audioband balanced homodyne detector 63
5.2 Squeezing from 1 kHz to 100 kHz 69
5.3 Loss analysis 71
5.4 Squeezing below 1 kHz 74

6 Outlook 77
6.1 Digital locking scheme for squeezed vacuum states 77
6.2 Reduction of the external pump power for the generation of squeezed states 81

7 Summary 83

Appendix 85
1 Low frequency homodyne detector 85

Resources 93

Acknowledgements 95

Bibliography 99

1 Introduction

In 1927, Werner Heisenberg introduced the uncertainty relation for the position and momentum of a particle [Hei27]. The uncertainty principle is a fundamental property of physics. It states that two hermitian, non-commuting observables cannot be measured with arbitrary precision at the same time and that the product of the variances of the measurement results is always equal or larger than a positive nonzero number ([Sch07], p. 100).

In quantum optics, such a pair of observables is given by the operators that describe the amplitudes of the phase and amplitude quadratures of a quantized electromagnetic field. Fluctuations in the amplitude and phase of an electromagnetic field can have technical reasons and can be eliminated by careful design of the source. The remaining uncertainty, the shot noise, is a fundamental property of nature and cannot be fully eliminated by technical means ([Lou87], p. 709). Shot noise thus limits the level of precision at which the phase and amplitude quadrature of any laser can be resolved. This situation is depicted in figure 1.1. It shows the time dependent oscillation of the electric field of a laser. The uncertainty of the amplitude quadrature is indicated by the red arrow.

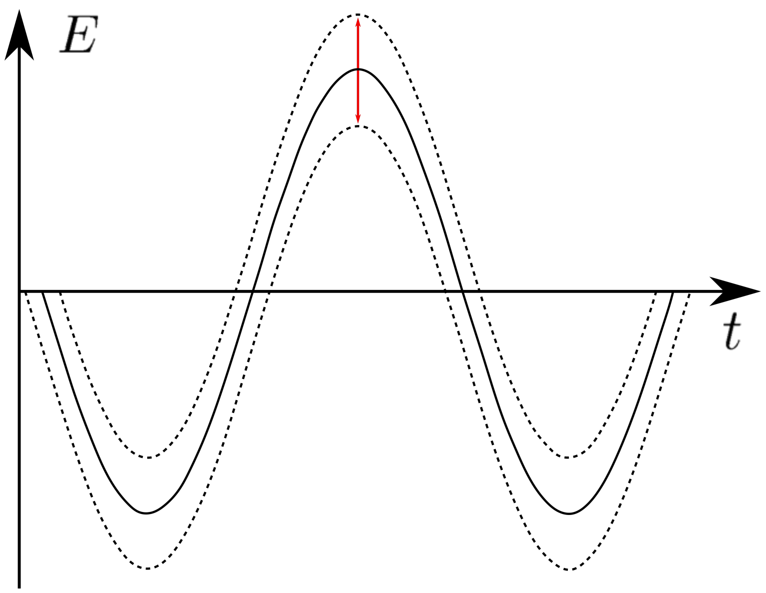

Figure 1.1: The figure illustrates how the uncertainty of the amplitude quadrature limits the level of precision of an amplitude measurement of a laser beam. The uncertainty envelope is indicated by the dashed lines ([Lou87], p. 710).

The quadrature uncertainties can be observed as shot noise by absorbing the light with a photoelectric detector. With a balanced homodyne detector, they can even be observed if the light is in its ground state and does not contain any photons. These vacuum oscillations result from the zero point fluctuations of the quantized harmonic oscillator. However, it is possible to reduce ("squeeze") the uncertainty of one quadrature below the shot noise level at the expense of an increased ("anti-squeezed") variance in the orthogonal quadrature. Quantum optical states with this property are called squeezed states. For squeezed states, the product of the measured uncertainties of two orthogonal quadratures has the lowest value that is allowed by Heisenberg's uncertainty principle. Squeezing can be observed in either coherent or vacuum states ([Sch17], p. 14).

Since squeezed states have been described for the first time in theory, several experiments have been performed to probe their existence [And16]. References to various theoretical works can be found in ([Lou87], p. 710). The first successful demonstration of squeezed states with a noise reduction of 0.3 dB below the shot noise level by four-wave mixing was done by Slusher et al. [Slu85]. They used Na atoms as a nonlinear medium. The squeezing process was enhanced by using cavities for the pump field and the squeezed field, a technique that was also applied in the experiment presented in this thesis. Shortly after this result, Wu et al. generated squeezed states with a noise reduction of more than 3 dB by parametric down-conversion [Wu86]. In this case, the nonlinear material was a MgO:$LiNbO_3$ crystal. The squeezing was observed at a wavelength of 1.06 μm. Significant technical improvements related to the technique of squeezing generation from parametric down-conversion have led to very high squeeze factors of 10 dB in 2008 [Vah08b]. This result was achieved with a laser wavelength of 1064 nm. Further developments have made values of 15 dB at 1064 nm [Vah16] possible and extended the range of wavelengths at which strong squeezing can be observed to 1550 nm with 12.3 dB [Meh11] and 532 nm with 5.5 dB [Bau15]. Over time, not only the squeeze factors have been extended to larger values, but also the frequency range in which squeezing can be observed has been increased from frequencies of a few Hz [Vah10, Wad15] to GHz [Ast13].

The work on the generation of high squeeze factors, especially at acoustic frequencies, has been driven by their proposed application in gravitational-wave detectors by Caves [Cav81]. Gravitational-wave detectors perform laser interferometric measurements and have directly observed gravitational waves for the first time in 2015 [Abb16]. A proof of principle experiment has demonstrated that the LIGO detectors that performed the measurements can be improved with squeezing in the shot noise limited frequency range from 150 Hz to 5 kHz [Aas13]. Alternatively, the laser power in the interferometer could be increased to decrease the shot noise spectral density ([Sch17], p. 30). However, higher laser powers introduce other problems, such as the heating of coatings or substrates, which, in turn, leads to an increased coating thermal noise ([Bas14], p. 242) or thermal lensing in the beam splitter or arm cavities [Win91]. For that reason, the laser power cannot be increased to arbitrary high levels. The gravitational-wave detector GEO600 has already been equipped with a squeezed-light source to improve its sensitivity in 2011 [Aba11] and has used this technology during operation ever since [Gro13]. For example, squeezing was applied for 205.2 days during a time in which the detector generated scientific data from November 2011 till October 2012. It led to an improved performance above a frequency of 400 Hz, proving the maturity of the technology in scientific applications. An upgrade of the VIRGO detector in Italy with a squeezed-light source is in progress [Leo16, Kni18] and a future upgrade of the LIGO detectors will also include squeezing ([Mü17], p. 71). While all of these detectors use lasers with a wavelength of 1064 nm, the Einstein Telescope, a planned European detector, might be operated with interferometers at both 1064 nm and 1550 nm and will incorporate squeezing at both wavelengths ([Abe11], pp. 230 – 231).

Apart from gravitational-wave detection, several other applications for squeezed states of light have been identified: Squeezing can enhance the measurement sensitivity in biological measurements such as laser-based microparticle tracking [Tay13]. In this case, the shot noise reduction by increasing the light power is not feasible since it would destroy the probe. Apart from that, squeezed states can be used to measure cavity parameters of high Q cavities by partially destroying the quantum correlations within a squeezed laser beam and measuring the resulting squeezing spectrum. Squeezed states hardly contain any photons. Thus, their optical power is very small. For that reason, they are optimal to probe high Q cavities. Even for weak coherent states, the large power built-up in those cavities leads to nonlinear processes and increased absorption and scattering, which would increase the uncertainty in the corresponding measurements [Mik06]. Because of their responsivity to losses, squeezed states with high squeeze factors can be used for the calibration of photo detectors. By careful characterization of the inefficiencies of the optical setup, the detection efficiency of a photo detector can be deduced by comparing the measured squeezing with the anti-squeezing level. This was demonstrated in [Vah16]. Another interesting application of squeezed states is quantum key distribution. Overlaying two squeezed states on a beam splitter results in an entangled state, which can be used to distribute a quantum key, as experimentally shown in [Geh15].

However, the experiments described above were conducted on large optical tables and the squeezed-light sources were set up on theses tables as well. The source for GEO600 was the first source for strong squeezing that was built with the intention of being portable. It was not assembled at the detector site, but in a special laboratory and brought to the detector after its completion. It was set up on a breadboard of 1.35 m x 1.13 m which has a weight of about 70 kg ([Kha11], p. 45). To allow for a more widespread use of squeezed-light sources, the footprint and the weight have to be reduced even further in future.

Thus, the aim of this thesis was to develop a more compact setup and to reduce the footprint to 80 cm x 80 cm while maintaining strong squeeze factors. The experiment was performed at the telecommunication wavelength of 1550 nm and designed to produce squeezed vacuum states at MHz frequencies and in the audioband. Thus, the squeezed-light laser developed here can serve as a source for quantum key distribution experiments, can be used to reduce the shot noise in laser interferometric experiments and can be regarded as a proof-of-concept setup for the application in gravitational-

wave detectors like the Einstein Telescope that are operated at 1550 nm.
The thesis is structured as follows: Chapter two introduces the theoretical concepts that underlie the generation of squeezed states of light and the characterization of a squeezed-light laser. The experimental setup is described in chapter three. Chapter four presents the measured squeezing at MHz frequencies and chapter five the results that were achieved in the audioband. The thesis ends with a summary and suggestions of improvements that can be implemented in future developments.

2 Theoretical concepts

2.1 Quantum theory of light

In classical physics, the electromagnetic field is described by Maxwell's equations. This description explains classical electrodynamics ([Dem06], pp. 136ff.). To describe squeezed states of light, this classical theory is not sufficient and a quantum mechanical explanation is required. This quantum mechanical picture will be reviewed in the following sections.

2.1.1 Quantization of the electromagnetic field

To introduce the quantum theory of light, we follow the procedure described in the book of C.C. Gerry and P.L. Knight ([Ger05], pp. 10ff.). We assume a cavity of length L with perfectly conducting walls located at $z = 0$ and $z = L$ in which the electric and the corresponding magnetic single mode fields $\vec{E} = (E_x, 0, 0)$ and $\vec{B} = (0, B_y, 0)$ with components

$$E_x(z,t) = \sqrt{\frac{2\nu^2}{V\epsilon_0}}\, q(t) \sin(kz)\,, \tag{2.1}$$

$$B_y(z,t) = \left(\frac{\mu_0\epsilon_0}{k}\right) \sqrt{\frac{2\nu^2}{V\epsilon_0}}\, p(t) \cos(kz) \tag{2.2}$$

are propagating along the z direction. Here, ν is the frequency of the cavity mode and $k = \frac{\nu}{c}$ the wave number, V is the effective volume of the cavity, ϵ_0 is the electric permittivity and μ_0 is the magnetic permeability of free space. $q(t)$ and $p(t)$ are the canonical position and momentum with the relationship $p(t) = \dot{q}(t)$. The Hamiltonian of this system, which corresponds to the field's energy, is given by

$$\begin{aligned} H &= \frac{1}{2}\int dV \left[\epsilon_0 E_x^2(z,t) + \frac{1}{\mu_0} B_y^2(z,t)\right] && (2.3)\\ &= \frac{1}{2}\left(p^2 + \nu^2 q^2\right). && (2.4) \end{aligned}$$

This Hamiltonian is formally equivalent to the one of a classical harmonic oscillator. We now quantize the electromagnetic field, introduce the operators $\hat{q}$ and $\hat{p}$ with the commutation relation $[\hat{q}, \hat{p}] = i\hbar$ and obtain

$$\hat{H} = \frac{1}{2}\left(\hat{p}^2 + \nu^2 \hat{q}^2\right). \tag{2.5}$$

Furthermore, we define the creation operator $\hat{a}^\dagger$ and the annihilation operator $\hat{a}$:

$$\hat{a} = \frac{1}{\sqrt{2\hbar\nu}} \left(\nu\hat{q} + \mathrm{i}\hat{p}\right), \tag{2.6}$$

$$\hat{a}^\dagger = \frac{1}{\sqrt{2\hbar\nu}} \left(\nu\hat{q} - \mathrm{i}\hat{p}\right). \tag{2.7}$$

With this definition, the Hamiltonian becomes

$$\hat{H} = \hbar\nu \left(\hat{a}^\dagger\hat{a} + \frac{1}{2}\right). \tag{2.8}$$

It allows us to introduce the number states in the following chapter and to find a physical interpretation for the annihilation and creation operators.

2.1.2 Number states

We now introduce number states, which are denoted $|n\rangle$ ([Wal08], pp. 10ff., [Ger05], pp. 13ff.) and are eigenstates of the number operator $\hat{n} = \hat{a}^\dagger\hat{a}$. They satisfy the equation

$$\hat{a}^\dagger\hat{a}|n\rangle = \hat{n}|n\rangle = n|n\rangle, \tag{2.9}$$

with $n \in 0, 1, 2 \ldots \infty$. The annihilation and creation operators act on the number states in the following way:

$$\hat{a}|n\rangle = \sqrt{n}|n-1\rangle, \tag{2.10}$$

$$\hat{a}^\dagger|n\rangle = \sqrt{n+1}|n+1\rangle. \tag{2.11}$$

The creation operator increases n by one, while the annihilation operator decreases n by one. The ground state, corresponding to $n = 0$, is defined by $\hat{a}|0\rangle = 0$. From that ground state, every number state can be generated by applying the creation operator n times:

$$|n\rangle = \frac{\left(\hat{a}^\dagger\right)^n}{\sqrt{n!}}|0\rangle. \tag{2.12}$$

The number states are also eigenstates of the Hamiltonian (2.8):

$$\hat{H}|n\rangle = \hbar\nu \left(\hat{a}^\dagger\hat{a} + \frac{1}{2}\right)|n\rangle = \hbar\nu \left(n + \frac{1}{2}\right)|n\rangle = E_n|n\rangle. \tag{2.13}$$

The eigenvalues $E_n = \hbar\nu\left(n + \frac{1}{2}\right)$ correspond to the energy of the number state $|n\rangle$. The physical meaning of the annihilation and creation operator becomes apparent if we calculate the eigenvalues of $\hat{a}^\dagger|n\rangle$ and $\hat{a}|n\rangle$. They are given by

$$\hat{H}\hat{a}^\dagger|n\rangle = \hbar\nu \left(\hat{a}^\dagger\hat{a} + \frac{1}{2}\right)\hat{a}^\dagger|n\rangle = \left(E_n + \hbar\nu\right)\hat{a}^\dagger|n\rangle, \tag{2.14}$$

$$\hat{H}\hat{a}|n\rangle = \hbar\nu \left(\hat{a}^\dagger\hat{a} + \frac{1}{2}\right)\hat{a}|n\rangle = \left(E_n - \hbar\nu\right)\hat{a}|n\rangle. \tag{2.15}$$

As equations (2.10) and (2.11) show, n can be increased or decreased by applying $\hat{a}^\dagger$ or $\hat{a}$. Equations (2.14) and (2.15) imply that changing n by ± 1 corresponds to the creation or destruction of a quanta of energy $\hbar\nu$, that is to say a photon is created or annihilated. Thus, n can be interpreted as a number of particles. The ground state $|0\rangle$, also called vacuum state, does not contain any photons. However, it has a zero point energy of $\frac{1}{2}\hbar\nu$. The eigenvalues $E_n = \hbar\nu\left(n + \frac{1}{2}\right)$ can also be understood as energy levels in a quantized harmonic oscillator of frequency ν. Furthermore, the number states form an orthogonal, complete set with

$$\langle m|n\rangle = \delta_{mn}, \tag{2.16}$$

$$\sum_{n=0}^{\infty} |n\rangle \langle n| = 1 \tag{2.17}$$

and can be used as a basis ([Ger05], p. 15). Apart from number states, laser light can be described by coherent states. They will be introduced in the following section.

2.1.3 Coherent states

A laser beam does not contain a well-defined number of photons. For that reason, it is not adequate to describe it with number states. Coherent states, as introduced in this section, offer a more suitable formalism ([Ger05], pp. 43ff., [Wal08], pp. 12ff.). They are generated by the displacement operator, which is defined as

$$\hat{D}(\alpha) = \mathrm{e}^{\alpha\hat{a}^\dagger - \alpha^*\hat{a}} \tag{2.18}$$

with α being a complex number. A coherent state $|\alpha\rangle$ is generated if the displacement operator acts on the vacuum state:

$$|\alpha\rangle = \hat{D}(\alpha)|0\rangle. \tag{2.19}$$

The state can be expressed in terms of the number states:

$$|\alpha\rangle = \mathrm{e}^{-\frac{|\alpha|^2}{2}} \sum_{n=0}^{\infty} \frac{\alpha^n}{\sqrt{n!}}|n\rangle. \tag{2.20}$$

This equation shows that the concept of coherent states accounts for the indefinite photon number in an actual laser beam ([Wal08], pp. 12ff.). The probability distribution of the photon number contained in a coherent state is given by

$$P(n) = |\langle n|\alpha\rangle|^2 = \frac{|\alpha|^{2n}\mathrm{e}^{-|\alpha|^2}}{n!}, \tag{2.21}$$

which is a Poissonian distribution. The mean photon number is given by

$$\bar{n} = \langle\alpha|\hat{a}^\dagger\hat{a}|\alpha\rangle = |\alpha|^2. \tag{2.22}$$

Thus, $|\alpha|$ can be understood as the classical amplitude of a bright laser beam. A graphical picture of coherent states in phase space that underlines their properties can be developed after the Wigner function has been introduced in the following section.

2.1.4 Wigner function

To visualize a quantum state, it is useful to introduce the Wigner function. Defining the density operator $\hat{\rho}$ as $\hat{\rho} = \sum_{n=0}^{\infty} \rho_n |\psi_n\rangle \langle\psi_n|$ with ρ_n being the probability of $|\psi_n\rangle$, we can write

$$W\big(q,p\big) = \frac{1}{2\pi\hbar} \int_{-\infty}^{\infty} \Big\langle q + \frac{1}{2}x \Big| \hat{\rho} \Big| q - \frac{1}{2}x \Big\rangle \mathrm{e}^{\frac{-\mathrm{i}px}{\hbar}} dx \tag{2.23}$$

for the Wigner function ([Fur15], p. 33), which is normalized to unity:

$$\int_{-\infty}^{\infty} \int_{-\infty}^{\infty} dq\, dp\, W\big(q,p\big) = 1. \tag{2.24}$$

However, it can also take on negative values, for example for the number state $|1\rangle$ ([Fur15], p. 42). Since classical physics does not allow for negative probabilities, the Wigner function is not a probability distribution in the classical sense. Probability densities for q and p of a state $|\psi\rangle$ that are non negative for all q and p are given by the projections of the Wigner function on the corresponding plane ([Ger05], p. 64)

$$\int_{-\infty}^{\infty} W\big(q,p\big) dp = |\psi\left(q\right)|^2, \tag{2.25}$$

$$\int_{-\infty}^{\infty} W\big(q,p\big) dq = |\varphi\left(p\right)|^2. \tag{2.26}$$

As an example, we show how a vacuum state $|0\rangle$ and a coherent state $|\alpha\rangle$ are visualized in phase space with the help of the Wigner function. First, we simplify equations (2.6) and (2.7) by renormalizing $\hat{q}$ and $\hat{p}$ according to $\hat{q} \rightarrow \sqrt{\frac{\nu}{2\hbar}}\hat{q}$ and $\hat{p} \rightarrow \frac{1}{\sqrt{2\hbar\nu}}\hat{p}$, which results in $[\hat{p}, \hat{q}] = \frac{\mathrm{i}}{2}$ for the commutator ([Fur15], pp. 3–4) and get

$$\hat{a} = \hat{q} + \mathrm{i}\hat{p}, \tag{2.27}$$

$$\hat{a}^\dagger = \hat{q} - \mathrm{i}\hat{p}, \tag{2.28}$$

and thus

$$\hat{q} = \frac{1}{2}\left(\hat{a} + \hat{a}^\dagger\right), \tag{2.29}$$

$$\hat{p} = \frac{1}{2\mathrm{i}}\left(\hat{a} - \hat{a}^\dagger\right). \tag{2.30}$$

With $\hat{a}\,|\alpha\rangle = \alpha\,|\alpha\rangle$ and $\langle\alpha|\,\hat{a}^\dagger = \langle\alpha|\,\alpha^*$, the expectation values of $\hat{q}$ and $\hat{p}$ of the coherent state are:

$$\langle\alpha\,|\hat{q}|\,\alpha\rangle = \frac{\alpha + \alpha^*}{2} = \Re\left(\alpha\right), \tag{2.31}$$

$$\langle\alpha\,|\hat{p}|\,\alpha\rangle = \frac{\alpha - \alpha^*}{2\mathrm{i}} = \Im\left(\alpha\right). \tag{2.32}$$

Here, we also used $\langle \alpha | \alpha \rangle = 1$. For the vacuum state $|0\rangle$, we obtain

$$\langle 0 |\hat{q}| 0\rangle = 0, \tag{2.33}$$
$$\langle 0 |\hat{p}| 0\rangle = 0. \tag{2.34}$$

The Wigner functions of the states are given by ([Fur15], pp. 35–36):

$$W_{|\alpha\rangle}(q,p) = \frac{2}{\pi} \mathrm{e}^{-2(q-q_0)^2 - 2(p-p_0)^2} \tag{2.35}$$

and

$$W_{|0\rangle}(q,p) = \frac{2}{\pi} \mathrm{e}^{-2\left(q^2+p^2\right)}. \tag{2.36}$$

Both distributions are depicted in figure 2.1. Since the expectation values of $\hat{q}$ and $\hat{p}$ are zero for the vacuum state $|0\rangle$, its Wigner function corresponds to a gaussian distribution centered at $(0,0)$. The coherent state $|\alpha\rangle = |4+\mathrm{i}4\rangle$ is displaced from the center to $(4,4)$, as expected from the calculation of the expectation values (2.31) and (2.32). The shift results from the coherent amplitude of the state. As we have seen in equation (2.22), the absolute value of $|\alpha\rangle$ is proportional to the square root of the mean photon number. The distance from the origin to the center of the distribution is given by $|\alpha|$ and can be thought of as a representation of the amplitude of a bright laser field containing $\bar{n}$ photons. In the next section, we will examine the variances of both states in detail.

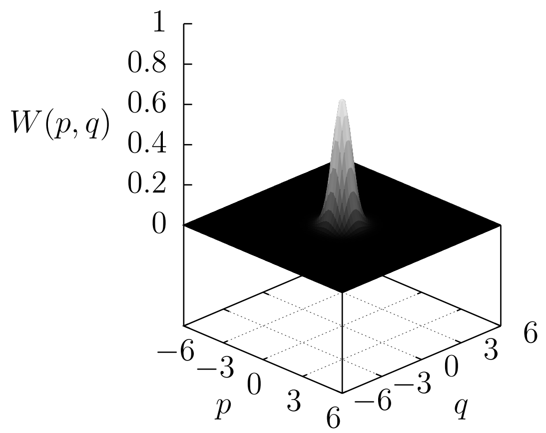

Figure 2.1: Wigner functions of a vacuum state (left) and coherent state $|\alpha\rangle = |4+\mathrm{i}4\rangle$ (right). The vacuum state is centered at $(0,0)$, while the center of the coherent state is moved to $(q_0,p_0) = (4,4)$. Those numbers were chosen as an example, any other values are possible. The shift results from the coherent amplitude α of the state.

2.1.5 Minimum uncertainty states

Since the normalized operators $\hat{p}$ and $\hat{q}$ do not commute, it is impossible to measure them simultaneously with arbitrary precision. Non-commuting observables $\hat{A}$ and $\hat{B}$ fulfill the Heisenberg commutation relation ([Sch07], p. 100)

$$\Delta^2\hat{A}\Delta^2\hat{B} \geq \frac{1}{4}\left|\left\langle\left[\hat{A},\hat{B}\right]\right\rangle\right|^2. \tag{2.37}$$

Thus, a measurement of the observables is always connected with an uncertainty. The accuracy of the measurement can be calculated from an ensemble of measurements. Before we calculate the variances, we define the quadrature operators $\hat{X}_1$ and $\hat{X}_2$ by ([Wal08], p. 16)

$$2\hat{a} = \hat{X}_1 + \mathrm{i}\hat{X}_2. \tag{2.38}$$

This definition rescales $\hat{p}$ and $\hat{q}$ and normalizes the variance of the vacuum to one, as we will see in the following. From the definition, we get

$$\hat{X}_1 = \hat{a} + \hat{a}^\dagger = 2\hat{q}, \tag{2.39}$$

$$\hat{X}_2 = \mathrm{i}\left(\hat{a}^\dagger - \hat{a}\right) = 2\hat{p}. \tag{2.40}$$

Thus, we can calculate the commutator to be

$$\begin{aligned}
\left[\hat{X}_1,\hat{X}_2\right] &= \hat{X}_1\hat{X}_2 - \hat{X}_2\hat{X}_1 \\
&= \mathrm{i}\left(\hat{a}+\hat{a}^\dagger\right)\left(\hat{a}^\dagger-\hat{a}\right) - \mathrm{i}\left(\hat{a}^\dagger-\hat{a}\right)\left(\hat{a}+\hat{a}^\dagger\right) \\
&= 2\mathrm{i}\left(\hat{a}\hat{a}^\dagger - \hat{a}^\dagger\hat{a}\right) \\
&= 2\mathrm{i}\left[\hat{a},\hat{a}^\dagger\right] = 2\mathrm{i} = 4\left[\hat{q},\hat{p}\right],
\end{aligned}$$

and the uncertainty relation becomes

$$\Delta^2\hat{X}_1\Delta^2\hat{X}_2 \geq 1. \tag{2.41}$$

Since no assumption about the actual quantum state that is investigated was made to calculate the commutator $\left[\hat{X}_1,\hat{X}_2\right]$, the result holds for all quantum states. To determine the individual variance of the two operators for a coherent state and a vacuum state, we use the fact that the variance $\Delta^2\hat{A}$ of an operator $\hat{A}$ can be calculated as ([Wal08], p. 15)

$$\Delta^2\hat{A} = \left\langle\hat{A}^2\right\rangle - \left\langle\hat{A}\right\rangle^2. \tag{2.42}$$

For the coherent state, we get

$$\begin{aligned}
\left\langle\hat{X}_1^2\right\rangle &= \left\langle\alpha\right|\left(\hat{a}+\hat{a}^\dagger\right)^2\left|\alpha\right\rangle \\
&= \left\langle\alpha\middle|\hat{a}^2 + 1 + 2\hat{a}^\dagger\hat{a} + \hat{a}^{\dagger 2}\middle|\alpha\right\rangle \\
&= 1 + \alpha^2 + 2\alpha\alpha^* + \alpha^{*2}, \\
\left\langle\hat{X}_1\right\rangle^2 &= \left(\left\langle\alpha\middle|\hat{a}+\hat{a}^\dagger\middle|\alpha\right\rangle\right)^2 \\
&= \alpha^2 + 2\alpha\alpha^* + \alpha^{*2}, \\
\Delta^2\hat{X}_1 &= 1.
\end{aligned} \tag{2.43}$$

In a similar way, we obtain

$$\begin{aligned}\langle \hat{X}_2^2 \rangle &= -\alpha^{*2} + 2\alpha\alpha^* + 1 - \alpha^2,\\ \langle \hat{X}_2 \rangle^2 &= -\alpha^{*2} + 2\alpha\alpha^* - \alpha^2,\\ \Delta^2 \hat{X}_2 &= 1.\end{aligned}$$

Apart from that, we see that

$$\begin{aligned}&\langle \hat{X}_1 \rangle^2 + \langle \hat{X}_2 \rangle^2 = 4|\alpha|^2\\ &\to |\alpha| = \frac{1}{2}\sqrt{\langle \hat{X}_1 \rangle^2 + \langle \hat{X}_2 \rangle^2}.\end{aligned}$$

For the vacuum state, we calculate

$$\begin{aligned}\langle \hat{X}_1^2 \rangle &= \langle 0| \left(\hat{a} + \hat{a}^\dagger\right)^2 |0\rangle = 1,\\ \langle \hat{X}_1 \rangle^2 &= \langle 0|\hat{a} + \hat{a}^\dagger|0\rangle^2 = 0,\\ \Delta^2 \hat{X}_1 &= 1\end{aligned}$$

and

$$\begin{aligned}\langle \hat{X}_2^2 \rangle &= \langle 0| \left(\mathrm{i}\left(\hat{a}^\dagger - \hat{a}\right)\right)^2 |0\rangle = 1,\\ \langle \hat{X}_2 \rangle^2 &= \langle 0|\mathrm{i}\left(\hat{a}^\dagger - \hat{a}\right)|0\rangle^2 = 0,\\ \Delta^2 \hat{X}_2 &= 1.\end{aligned}$$

The results are visualized in figure 2.2. The red circles can be understood as projections of the Wigner functions shown in figure 2.1 on the rescaled (X_1,X_2) plane. As expected, the coherent state on the left side is shifted away from the origin due to the coherent amplitude of the state while the vacuum state is centered at the origin. The variance in each quadrature of the states is equal to one. Thus both states have the smallest possible uncertainty product of

$$\Delta^2 \hat{X}_1 \Delta^2 \hat{X}_2 = 1. \tag{2.44}$$

For that reason, the coherent state and the vacuum are minimum uncertainty states. In the next section, we will introduce a third kind of minimum uncertainty state that has a variance $\Delta^2 \hat{X}_{1,2} < 1$ in one quadrature. However, since the uncertainty principle still holds, the variance increases in the orthogonal quadrature. These states are called squeezed states.

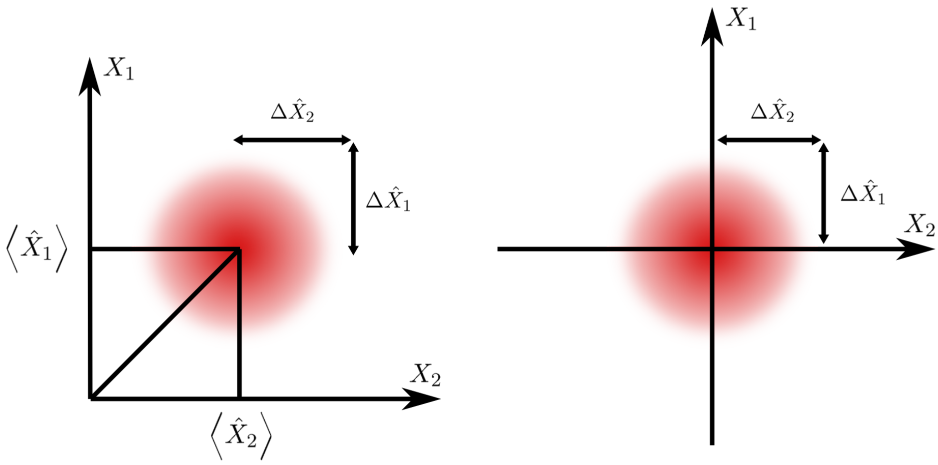

Figure 2.2: Visualization of a coherent and a vacuum state. On the left, the coherent state is depicted. The actual position in phase space cannot be determined with absolute precision due to the Heisenberg uncertainty principle, which is indicated by the red circular area. For example, the uncertainty of a measurement of $\hat{X}_1$ is given by $\Delta\hat{X}_1$. The same holds for the vacuum state on the right. The coherent state is displaced in phase space and the distance to the origin is given by $|\alpha| = \frac{1}{2}\sqrt{\left\langle\hat{X}_1\right\rangle^2 + \left\langle\hat{X}_2\right\rangle^2}$. Since a vacuum has no coherent amplitude, the ball is centered at the origin.

2.1.6 Squeezed states

A special class of minimum uncertainty states are squeezed states. They obey the Heisenberg uncertainty relation (2.44), but have a variance smaller than one in either of their quadratures. A squeezed vacuum state is created by the application of the squeezing operator on the vacuum $|0\rangle$. Subsequent application of the displacement operator (2.18) leads to a squeezed coherent state ([Wal08], p. 17). The squeezing operator is defined as

$$\hat{S} = \exp\left[\frac{1}{2}\xi^*\hat{a}^2 - \frac{1}{2}\xi\hat{a}^{\dagger 2}\right], \tag{2.45}$$

with $\xi = r\mathrm{e}^{\mathrm{i}2\Theta}$ where r is the squeeze parameter and Θ determines the orientation of the quadrature in which the variance will be reduced below one and thus the squeezing will be apparent ([Bac04], p. 242). To simplify the calculations, we assume $\Theta = 0$. To calculate the effect of the squeezing operator on a vacuum state we use the relations ([Ger05], p. 153)

$$\hat{S}^\dagger(\xi)\,\hat{a}\hat{S}(\xi) = \hat{a}\cosh r - \hat{a}^\dagger\sinh r, \tag{2.46}$$

$$\hat{S}^\dagger(\xi)\,\hat{a}^\dagger\hat{S}(\xi) = \hat{a}^\dagger\cosh r - \hat{a}\sinh r. \tag{2.47}$$

Using equation (2.42) again, we obtain

$$\begin{aligned}
\langle \hat{X}_1^2 \rangle &= \left\langle \left(\hat{a} + \hat{a}^\dagger\right)^2 \right\rangle \\
&= \langle \hat{S}^\dagger \hat{a} \hat{S} \hat{S}^\dagger \hat{a} \hat{S} \rangle + \langle \hat{S}^\dagger \hat{a} \hat{S} \hat{S}^\dagger \hat{a}^\dagger \hat{S} \rangle + \langle \hat{S}^\dagger \hat{a}^\dagger \hat{S} \hat{S}^\dagger \hat{a} \hat{S} \rangle + \langle \hat{S}^\dagger \hat{a}^\dagger \hat{S} \hat{S}^\dagger \hat{a}^\dagger \hat{S} \rangle \\
&= -2 \sinh r \cosh r + \sinh^2 r + \cosh^2 r, \\
\langle \hat{X}_1 \rangle^2 &= \left\langle \left(\hat{a} + \hat{a}^\dagger\right) \right\rangle^2 \\
&= \left(\langle 0 | \hat{S}^\dagger \hat{a} \hat{S} | 0 \rangle + \langle 0 | \hat{S}^\dagger \hat{a}^\dagger \hat{S} | 0 \rangle \right)^2 = 0.
\end{aligned}$$

Thus, the variance of $\hat{X}_1$ is squeezed (decreased) with a factor of e^{-2r}:

$$\begin{aligned}
\Delta^2 \hat{X}_1 &= \sinh^2(r) + \cosh^2(r) - 2\sinh(r)\cosh(r) \\
&= \cosh(2r) - \sinh(2r) \\
&= \frac{1}{2}\left(\mathrm{e}^{2r} + \mathrm{e}^{-2r}\right) - \frac{1}{2}\left(\mathrm{e}^{2r} - \mathrm{e}^{-2r}\right) = \mathrm{e}^{-2r}.
\end{aligned}$$

For $\hat{X}_2$, we get an anti-squeezed (increased) variance of

$$\begin{aligned}
\Delta^2 \hat{X}_2 &= 2\sinh(r)\cosh(r) + \sinh^2(r)\cosh^2(r) \\
&= \sinh(2r) + \cosh(2r) = \mathrm{e}^{2r}.
\end{aligned}$$

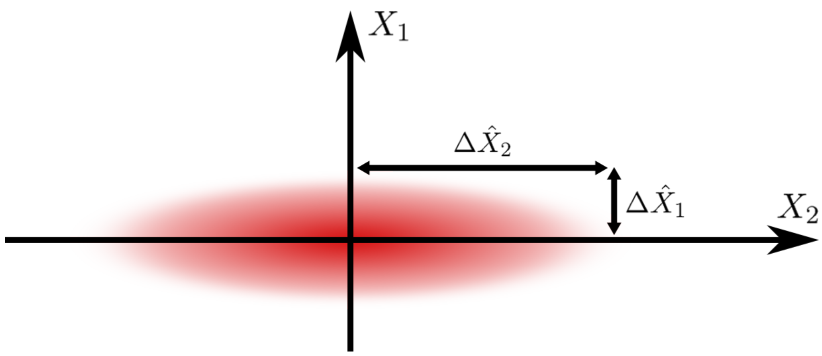

Figure 2.3: Phase space representation of an amplitude squeezed vacuum state. The reduction of the variance in $\hat{X}_1$ leads to an increased variance in $\hat{X}_2$. However, the uncertainty relation (2.44) is still fullfilled. Thus, the squeezed state is a minimum uncertainty state.

However, the uncertainty relation (2.44) is still fulfilled since $\Delta^2\hat{X}_1\Delta^2\hat{X}_2 = \mathrm{e}^{-2r}\mathrm{e}^{2r} = 1$. Here, the special properties of squeezed vacuum states become apparent. Our calculation shows that the variance of the amplitude quadrature can be reduced below the value that the uncertainty relation (2.41) allows for minimum uncertainty states with equal variance in both quadratures. This situation is illustrated in figure 2.3. It shows the projection of the Wigner function of a squeezed vacuum state on the (X_1, X_2) plane. However, the variance can be squeezed along an axis different than

X_1. The ellipse can be rotated by changing the squeeze angle Θ. Another special property of squeezed vacuum states is apparent in their photon number distribution. The probability to detect m photons is given by ([Ger05], p. 163)

$$P_{\mathrm{m}} = \frac{\left(\frac{1}{2}\tanh\left(r\right)\right)^m}{m!\cosh\left(r\right)}\left|H_{\mathrm{m}}\left(0\right)\right|^2. \tag{2.48}$$

A squeezed vacuum state only contains photon pairs and multiples thereof. This property is depicted in figure 2.4 for a state with 4.3 dB squeezing ($r = 0.51$) ([Sch17], p. 19) and 10 dB ($r = 1.15$).

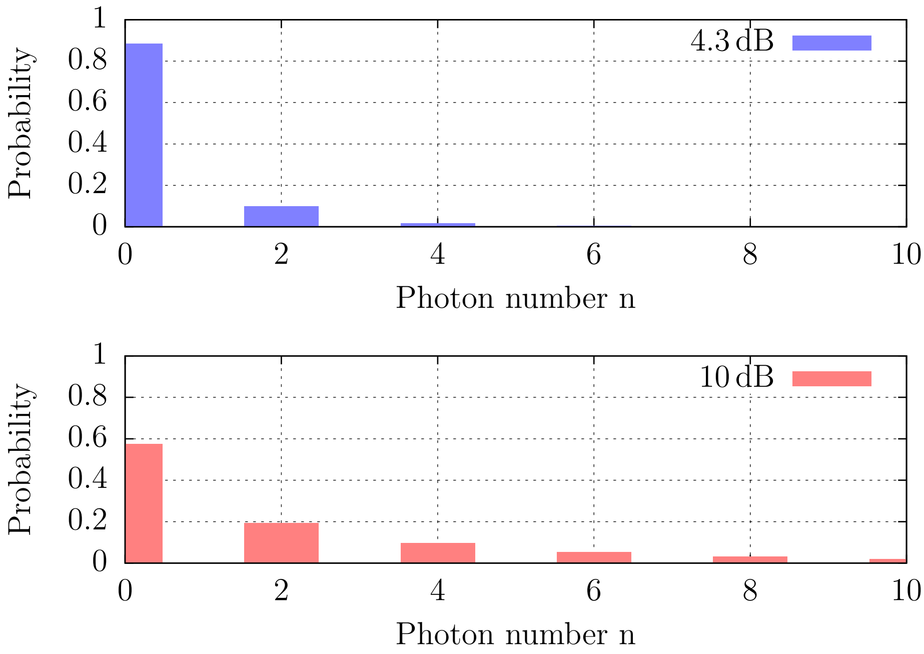

Figure 2.4: Photon number distribution of a 4.3 dB and 10 dB squeezed vacuum state. Squeezed vacuum states only contain even photon numbers, since the squeezing operator given in equation (2.45) only creates photon pairs. The stronger the squeezing, the higher the probability for even photon numbers > 2.

2.2 Cavity-enhanced nonlinear processes

Within this thesis, the nonlinear processes of second-harmonic generation and parametric down-conversion as shown in figure 2.5 are of importance. Both effects exploit the second order optical susceptibility $\chi^{(2)}$ of a nonlinear material. The time dependent polarization of the material can be decomposed in a Taylor series that reads ([Boy08], p. 2)

$$P\left(t\right) = \epsilon_0\left[\chi^{(1)}E\left(t\right) + \chi^{(2)}E^2\left(t\right) + \chi^{(3)}E^3\left(t\right) + ...\right] \tag{2.49}$$

with the permittivity of free space ϵ_0 and the electric field $E(t)$. The nonlinear terms $P^{\mathrm{NL}} = \chi^{(2)} E^2(t) + \chi^{(3)} E^3(t) + ...$ give rise to new frequency components of the electric field ([Boy08], pp. 1–11). In second-harmonic generation, the input pump field at frequency ν_1 is converted to the signal at ν_2. Due to energy conservation, $\nu_2 = 2\nu_1$ holds. In parametric down-conversion, the inverse process takes place and can be used to generate a squeezed vacuum state. Both effects will be explained in detail in the following sections.

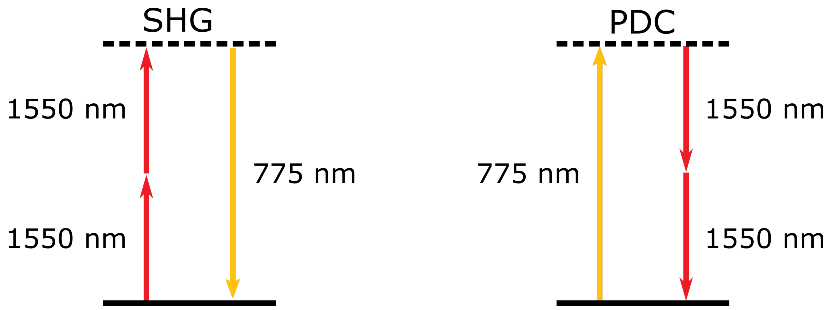

Figure 2.5: Energy level diagrams of the nonlinear processes that are of importance within this thesis. In second-harmonic generation (SHG), two photons at 1550 nm are converted to one photon at 775 nm. In parametric down-conversion (PDC), the inverse process generates two photons at 1550 nm from one at 775 nm.

2.2.1 Second-harmonic generation

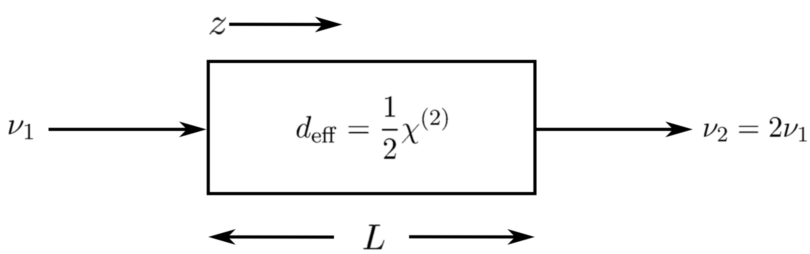

Figure 2.6: Second-harmonic generation within a nonlinear medium. Light with the frequency ν_1 enters a crystal of length L with an effective second order nonlinearity d_{eff} and is converted to $\nu_2 = 2\nu_1$ ([Boy08], p. 97).

To describe the effect of second-harmonic generation, which is exploited to generate the pump field for the parametric down-conversion cavity from the master laser in this thesis, we follow the procedure presented in ([Boy08], pp. 96–105). The theory describes the interaction of the electric fields with a nonlinear medium for a single pass assuming plane waves and shows how the coupling via the nonlinear polarization results in new frequency components of the electric field. For each frequency component ν_1, ν_2 of the process, the field can be expressed by

$$E_j(z,t) = A_j(z)\,\mathrm{e}^{\mathrm{i}k_j z}\mathrm{e}^{-\mathrm{i}\nu_j t} + c.c. \tag{2.50}$$

with $k_j = \frac{n_j \nu_j}{c}$, where c is the speed of light in vacuum and n_j the refractive index of the nonlinear medium for the corresponding frequency. $A_j(z)$ represents the amplitude of the field. E_1 refers to the pump and E_2 to the second-harmonic field. The total electric field of the process is given by

$$E(z,t) = E_1(z,t) + E_2(z,t). \tag{2.51}$$

The interaction of the fields with the nonlinear medium can be described by the wave equation

$$\frac{\partial^2 E_j}{\partial z^2} - \frac{n_j^2}{c^2}\frac{\partial^2 E_j}{\partial t^2} = \frac{1}{\epsilon_0 c^2}\frac{\partial^2 P_j^{\mathrm{NL}}}{\partial t^2}. \tag{2.52}$$

The term on the right side acts as the source for the new frequency components at ν_2. It is given by $P_j^{\mathrm{NL}} = P_j(z)\,\mathrm{e}^{-\mathrm{i}\nu_j t} + c.c.$ with

$$\begin{aligned} P_1(z) &= 4\epsilon_0 d_{\mathrm{eff}} E_2 E_1^* \\ P_2(z) &= 2\epsilon_0 d_{\mathrm{eff}} E_1^2. \end{aligned}$$

Here, we introduced the effective second order nonlinearity $d_{\mathrm{eff}} = \frac{1}{2}\chi^{(2)}$. From the wave equation, we can obtain the coupled differential equations describing the field amplitudes in the nonlinear medium

$$\frac{d}{dz}A_1 = \frac{2\mathrm{i}\nu_1^2 d_{\mathrm{eff}}}{k_1 c^2} A_2 A_1^* \mathrm{e}^{-\mathrm{i}\Delta k z}, \tag{2.53}$$

$$\frac{d}{dz}A_2 = \frac{\mathrm{i}\nu_2^2 d_{\mathrm{eff}}}{k_2 c^2} A_1^2 \mathrm{e}^{\mathrm{i}\Delta k z}, \tag{2.54}$$

with the phase mismatch $\Delta k = 2k_1 - k_2$. We now redefine the field amplitudes and use

$$A_1 = \left(\frac{I}{2n_1\epsilon_0 c}\right)^{\frac{1}{2}} u_1 \mathrm{e}^{\mathrm{i}\phi_1} \tag{2.55}$$

$$A_2 = \left(\frac{I}{2n_2\epsilon_0 c}\right)^{\frac{1}{2}} u_2 \mathrm{e}^{\mathrm{i}\phi_2} \tag{2.56}$$

with the total intensity $I = I_1 + I_2$ and $I_j = 2n_j\epsilon_0 c\,|A_j|^2$. Within this definition, the real, normalized field amplitudes u_1 and u_2 with phases ϕ_1 and ϕ_2 fulfill the condition

$$u_1(z)^2 + u_2(z)^2 = 1 \tag{2.57}$$

and are thus conserved at every point in the nonlinear medium. The relative phase of the fields is given by $\Theta = 2\phi_1 - \phi_2 + \Delta k z$. We also introduce the normalized distance parameter $\zeta = \frac{z}{l}$, with $l = \sqrt{\frac{2n_1^2 n_2}{\epsilon_0 c I}}\frac{c}{2\nu_1 d_{\mathrm{eff}}}$. With these definitions, the differential equations (2.53) and (2.54) become

$$\frac{d}{d\zeta}u_1 = u_1 u_2 \sin(\Theta), \tag{2.58}$$

$$\frac{d}{d\zeta}u_2 = -u_1^2 \sin(\Theta), \tag{2.59}$$

$$\frac{d}{d\zeta}\Theta = \Delta k l + \frac{\cos(\Theta)}{\sin(\Theta)}\frac{d}{d\zeta}\ln\left(u_1^2 u_2\right). \tag{2.60}$$

If we assume that no second-harmonic light is incident on the nonlinear medium, we get the inital conditions $u_1(0) = 1$ and $u_2(0) = 0$. We further assume perfect phase matching, leading to $\Delta k = 0$. In this case, the solution of the differential equations is given by

$$u_1(\zeta) = \frac{1}{\cosh(\zeta)}, \tag{2.61}$$

$$u_2(\zeta) = \tanh(\zeta). \tag{2.62}$$

The solutions are depicted in figure 2.7. Since the nonlinear medium is assumed to be lossless, the second-harmonic power increases with $\zeta \to \infty$ until the field has completely been converted. The derivations in this chapter do not take into consideration that a laser beam has to be described as a gaussian beam. In practice, this is important because the nonlinear medium is placed in a cavity that is resonant for the fundamental wavelength to enhance the interaction length and power and the laser is focused within that cavity to further increase the nonlinear coupling, which is proportional to $E^2(t)$. High conversion efficiencies of 95 % are possible with such a setup [Ast11]. Furthermore, the assumption that $\Delta k = 0$ is optimal for perfect phase matching is not valid for focused gaussian beams due to the Gouy phase shift [Las07].

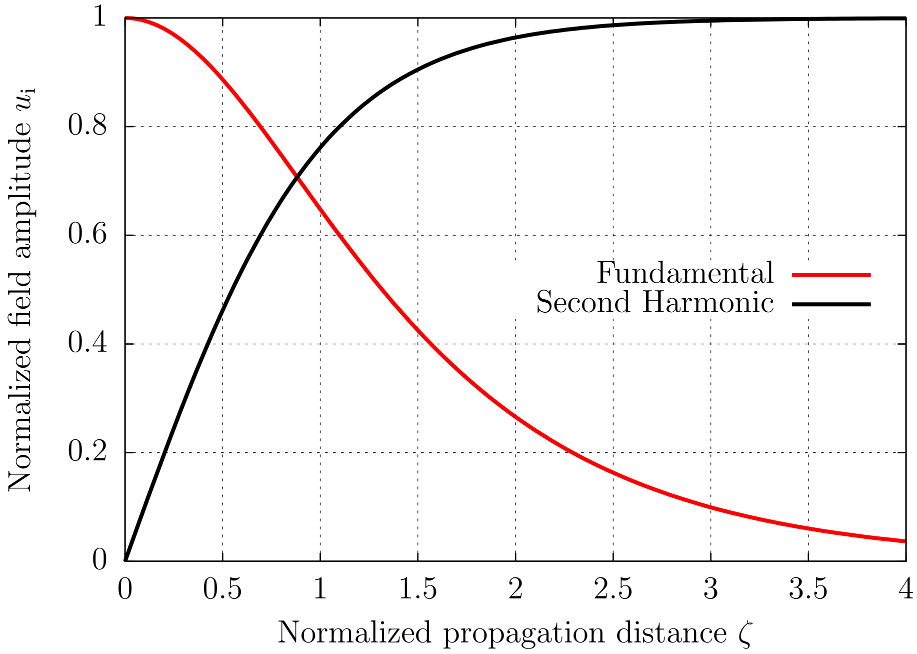

Figure 2.7: Conversion of the fundamental field at ν_1 to the second-harmonic field at $\nu_2 = 2\nu_1$. The amplitude of the second-harmonic and thus its power increases with the propagation distance in the nonlinear medium. For a sufficiently long distance, all the power of the fundamental field is converted to the second-harmonic.

2.2.2 Squeezing from degenerate parametric down-conversion

There exist several ways to generate squeezed vacuum states of light, for example four-wave mixing in atomic vapor as well as technologies exploiting optical fibers [And16]. In this thesis, squeezed vacuum states were generated with a second order nonlinear crystal placed in a cavity to exploit the effect of parametric down-conversion from 775 nm to 1550 nm. The squeezing spectrum that can be expected from such a setup can be calculated with the input-output theory that is presented in various sources. Our description in this chapter follows [Col84], [Gar85], [Dru14], [Mey07], [Wal08], [Bau16] and [NN08]. We will first derive the relations between modes entering and leaving a cavity. Afterwards, we will apply these relations to model our squeezed-light source.

Cavity input output formalism

To model the squeezed-light source used in this thesis and calculate the output spectra of the quadratures, we first consider an empty cavity interacting with a heat bath. The hamiltonian $\hat{H} = \hat{H}_{\text{sys}} + \hat{H}_{\text{bath}} + \hat{H}_{\text{int}}$ describes this model. $\hat{H}_{\text{sys}}$ is the system hamiltonian and is describing a cavity. $\hat{H}_{\text{bath}}$ describes the heat bath and $\hat{H}_{\text{int}}$ the interaction of the cavity with the bath. The Hamiltonians for the bath and the interaction are given by:

$$\hat{H}_{\text{bath}} = \int_{-\infty}^{\infty} d\omega\, \hbar\omega \hat{b}^{\dagger}(\omega, t)\, \hat{b}(\omega, t), \tag{2.63}$$

$$\hat{H}_{\text{int}} = \mathrm{i}\hbar \int_{-\infty}^{\infty} d\omega\, \kappa(\omega) \left[\hat{a}(t)\, \hat{b}^{\dagger}(\omega, t) - \hat{a}^{\dagger}(t)\, \hat{b}(\omega, t)\right]. \tag{2.64}$$

$\hat{H}_{\text{sys}}$ will be defined later when our parametric down-conversion cavity is modeled in detail. $\hat{a}(t)$ and $\hat{a}^{\dagger}(t)$ describe a single mode of this cavity and are thus frequency independent. The mode is coupled to the continuum of the heat bath, described by the frequency dependent operators $\hat{b}(\omega, t)$ and $\hat{b}^{\dagger}(\omega, t)$, via the coupling constant $\kappa(\omega)$. In the following, we make the Markovian approximation that the coupling of the cavity modes to the bath does not depend on the frequency and set $\kappa^2(\omega) = \frac{\gamma}{2\pi}$ [Gar85]. With this assumption, we also introduced the cavity linewidth γ. In equation (2.64), we integrate over all frequencies ranging from $-\infty$ to ∞, despite the fact that the physical range is $(0, \infty)$. However, quantum optical measurements are performed at a sideband frequency $\Omega = \omega - \nu$, this is to say with respect to some very large optical frequency ν in a rotating frame. As a result, the physical limit becomes $(-\nu, \infty)$. Since the optical frequencies are very large compared to the typical bandwidths that can be obtained in quantum optical experiments, extending the limit to $(-\infty, \infty)$ is a valid approximation ([Gar85],[Dru14], pp. 199ff.). The annihilation and creation operators describing the intracavity field and the external field obey the commutation relations

$$\left[\hat{a}(t), \hat{a}^{\dagger}(t)\right] = 1, \tag{2.65}$$

$$\left[\hat{b}(\omega, t), \hat{b}^{\dagger}(\omega', t)\right] = \delta(\omega - \omega'), \tag{2.66}$$

$$\left[\hat{a}(t), \hat{b}(\omega, t)\right] = 0. \tag{2.67}$$

To calculate the dynamics of this system, we make use of the Heisenberg equation of motion. For a hamiltonian $\hat{H}$ and operator $\hat{A}(t)$, it is given by ([Fur15], p. 2):

$$\frac{d}{dt}\hat{A}(t) = \frac{\mathrm{i}}{\hbar}\left[\hat{H}, \hat{A}(t)\right] \tag{2.68}$$

For the operator $\hat{b}(\omega, t)$ of the external bath, we obtain

$$\begin{aligned} \frac{d}{dt}\hat{b}(\omega, t) &= \frac{\mathrm{i}}{\hbar}\left[\hat{H}, \hat{b}(\omega, t)\right] \\ &= \frac{\mathrm{i}}{\hbar}\left[\hat{H}_{\text{bath}}, \hat{b}(\omega, t)\right] + \frac{\mathrm{i}}{\hbar}\left[\hat{H}_{\text{int}}, \hat{b}(\omega, t)\right]. \end{aligned}$$

The hamiltonian that describes the cavity gives a zero contribution, since it is independent of the modes of the bath. Using the general relation $\left[\hat{a}\hat{b}, \hat{c}\right] = \hat{a}\left[\hat{b}, \hat{c}\right] + \left[\hat{a}, \hat{c}\right]\hat{b}$, we get

$$\begin{aligned}\left[\hat{H}_{\text{bath}}, \hat{b}\left(\omega, t\right)\right] &= \int_{-\infty}^{\infty} d\omega' \hbar\omega' \left[\hat{b}^{\dagger}\left(\omega', t\right) \hat{b}\left(\omega', t\right), \hat{b}\left(\omega, t\right)\right] \\ &= \int_{-\infty}^{\infty} d\omega' \hbar\omega' \left(\hat{b}^{\dagger}\left(\omega', t\right) \left[\hat{b}\left(\omega', t\right), \hat{b}\left(\omega, t\right)\right] + \left[\hat{b}^{\dagger}\left(\omega', t\right), \hat{b}\left(\omega, t\right)\right] \hat{b}\left(\omega', t\right)\right) \\ &= -\hbar\omega \hat{b}\left(\omega, t\right)\end{aligned}$$

and

$$\begin{aligned}\left[\hat{H}_{\text{int}}, \hat{b}\left(\omega, t\right)\right] &= \mathrm{i}\hbar \int_{-\infty}^{\infty} d\omega' \sqrt{\frac{\gamma}{2\pi}} \left[\hat{a}\left(t\right) \hat{b}^{\dagger}\left(\omega', t\right) - \hat{a}^{\dagger}\left(t\right) \hat{b}\left(\omega', t\right), \hat{b}\left(\omega, t\right)\right] \\ &= -\mathrm{i}\hbar \sqrt{\frac{\gamma}{2\pi}} \hat{a}\left(t\right)\end{aligned}$$

and finally

$$\frac{d}{dt} \hat{b}\left(\omega, t\right) = \sqrt{\frac{\gamma}{2\pi}} \hat{a}\left(t\right) - \mathrm{i}\omega \hat{b}\left(\omega, t\right). \tag{2.69}$$

The differential equation (2.69) can be solved by integration ([Bau16], p. 81). It has two solutions, one for given initial conditions at times $t_0 < t$ and one for final conditions at times $t < t_1$ ([Wal08], p. 129). They are given by

$$\hat{b}\left(\omega, t\right) = \mathrm{e}^{-\mathrm{i}\omega(t-t_0)} \hat{b}\left(\omega, t_0\right) + \sqrt{\frac{\gamma}{2\pi}} \int_{t_0}^{t} dt' \mathrm{e}^{-\mathrm{i}\omega(t-t')} \hat{a}\left(t'\right), \tag{2.70}$$

$$\hat{b}\left(\omega, t\right) = \mathrm{e}^{-\mathrm{i}\omega(t-t_1)} \hat{b}\left(\omega, t_1\right) - \sqrt{\frac{\gamma}{2\pi}} \int_{t}^{t_1} dt' \mathrm{e}^{-\mathrm{i}\omega(t-t')} \hat{a}\left(t'\right). \tag{2.71}$$

We also need to calculate the equation of motion for the internal cavity modes. It is given by

$$\begin{aligned}\frac{d}{dt} \hat{a}\left(t\right) =& \frac{\mathrm{i}}{\hbar} \left[\hat{H}, \hat{a}\left(t\right)\right] \\ =& \frac{\mathrm{i}}{\hbar} \left(\left[\hat{H}_{\text{sys}}, \hat{a}\left(t\right)\right] + \left[\hat{H}_{\text{bath}}, \hat{a}\left(t\right)\right] + \left[\hat{H}_{\text{int}}, \hat{a}\left(t\right)\right]\right).\end{aligned}$$

With

$$\left[\hat{H}_{\text{bath}}, \hat{a}\left(t\right)\right] = 0$$

and

$$\begin{aligned}\left[\hat{H}_{\text{int}}, \hat{a}\left(t\right)\right] &= \mathrm{i}\hbar \int_{-\infty}^{\infty} d\omega \sqrt{\frac{\gamma}{2\pi}} \left[\left(\hat{a}\left(t\right) \hat{b}^{\dagger}\left(\omega, t\right) - \hat{a}^{\dagger}\left(t\right) \hat{b}\left(\omega, t\right)\right), \hat{a}\left(t\right)\right] \\ &= \mathrm{i}\hbar \int_{-\infty}^{\infty} d\omega \sqrt{\frac{\gamma}{2\pi}} \hat{b}\left(\omega, t\right)\end{aligned}$$

for the commutators, we get

$$\frac{d}{dt}\hat{a}(t) = -\frac{\mathrm{i}}{\hbar}\left[\hat{a}(t), \hat{H}_{\mathrm{sys}}\right] - \int_{-\infty}^{\infty} d\omega \sqrt{\frac{\gamma}{2\pi}}\hat{b}(\omega, t) \tag{2.72}$$

in total. We now define the operators of the fields entering the cavity and leaving it by

$$\hat{a}_{\mathrm{in}}(t) = -\frac{1}{\sqrt{2\pi}}\int_{-\infty}^{\infty} d\omega\, \mathrm{e}^{-\mathrm{i}\omega(t-t_0)}\hat{b}(\omega, t_0), \tag{2.73}$$

$$\hat{a}_{\mathrm{out}}(t) = \frac{1}{\sqrt{2\pi}}\int_{-\infty}^{\infty} d\omega\, \mathrm{e}^{-\mathrm{i}\omega(t-t_1)}\hat{b}(\omega, t_1). \tag{2.74}$$

Here, we used the convention that the incoming fields propagating to the left have a negative sign while the outgoing ones propagating to the right have a positive sign. This situation is depicted in figure 2.8. The picture also shows that we assume our cavity to be single sided: the back mirror is perfectly reflective, thus no light can leave the cavity through it. This approximation is also valid for the experimental system presented in this thesis, where the back mirror is highly reflective.

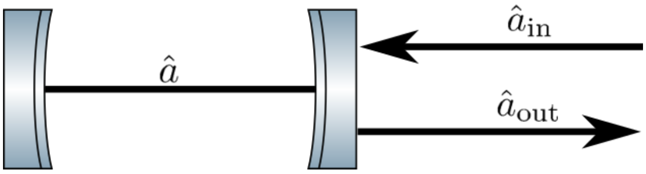

Figure 2.8: Model that is used to describe the coupling of a single sided cavity to an external bath. The left mirror is assumed to be highly reflective, thus no modes can enter or leave the cavity from this side. Only the right mirror is partially transmissive and allows for a coupling of the internal cavity modes $\hat{a}$ to the external bath via the input and output modes $\hat{a}_{\mathrm{in}}$ and $\hat{a}_{\mathrm{out}}$.

To get a relation between the internal cavity modes and the input field at times $t_0 < t$, we insert equation (2.70) into equation (2.72) and make use of the definition (2.73) to obtain

$$\begin{aligned}
\frac{d}{dt}\hat{a}(t) =& -\frac{\mathrm{i}}{\hbar}\left[\hat{a}(t), \hat{H}_{\mathrm{sys}}\right] \\
& - \int_{-\infty}^{\infty} d\omega \sqrt{\frac{\gamma}{2\pi}}\left(\mathrm{e}^{-\mathrm{i}\omega(t-t_0)}\hat{b}(\omega, t_0) + \sqrt{\frac{\gamma}{2\pi}}\int_{t_0}^{t} dt' \mathrm{e}^{-\mathrm{i}\omega(t-t')}\hat{a}(t')\right) \\
=& -\frac{\mathrm{i}}{\hbar}\left[\hat{a}(t), \hat{H}_{\mathrm{sys}}\right] \\
& - \sqrt{\frac{\gamma}{2\pi}}\int_{-\infty}^{\infty} d\omega \mathrm{e}^{-\mathrm{i}\omega(t-t_0)}\hat{b}(\omega, t_0) - \int_{-\infty}^{\infty} d\omega \frac{\gamma}{2\pi}\int_{t_0}^{t} dt' \mathrm{e}^{-\mathrm{i}\omega(t-t')}\hat{a}(t') \\
=& -\frac{\mathrm{i}}{\hbar}\left[\hat{a}(t), \hat{H}_{\mathrm{sys}}\right] + \sqrt{\gamma}\hat{a}_{\mathrm{in}}(t) - \frac{\gamma}{2\pi}\int_{-\infty}^{\infty} d\omega \int_{t_0}^{t} dt' \mathrm{e}^{-\mathrm{i}\omega(t-t')}\hat{a}(t').
\end{aligned}$$

Using the relation

$$\int_{-\infty}^{\infty} d\omega\, \mathrm{e}^{-\mathrm{i}\omega(t-t')} = 2\pi\delta\left(t-t'\right) \tag{2.75}$$

and

$$\int_{t_0}^{t} dt' f\left(t'\right)\delta\left(t-t'\right) = \int_{t}^{t_1} dt' f\left(t'\right)\delta\left(t-t'\right) = \frac{1}{2} f\left(t\right) \tag{2.76}$$

which holds for $t_0 < t < t_1$, we get

$$\frac{d}{dt}\hat{a}\left(t\right) = -\frac{\mathrm{i}}{\hbar}\left[\hat{a}\left(t\right), \hat{H}_{\mathrm{sys}}\right] + \sqrt{\gamma}\hat{a}_{\mathrm{in}}\left(t\right) - \frac{\gamma}{2}\hat{a}\left(t\right). \tag{2.77}$$

In a similar way, we can insert equation (2.71) into (2.72) and use (2.74) to get a connection between the output modes and the internal modes and obtain

$$\frac{d}{dt}\hat{a}\left(t\right) = -\frac{\mathrm{i}}{\hbar}\left[\hat{a}\left(t\right), \hat{H}_{\mathrm{sys}}\right] - \sqrt{\gamma}\hat{a}_{\mathrm{out}}\left(t\right) + \frac{\gamma}{2}\hat{a}\left(t\right). \tag{2.78}$$

Substracting equation (2.78) from (2.77) yields

$$\sqrt{\gamma}\hat{a}\left(t\right) = \hat{a}_{\mathrm{in}}\left(t\right) + \hat{a}_{\mathrm{out}}\left(t\right) \tag{2.79}$$

and relates the input of the cavity with the output from it. The connection is given by the internal cavity modes. In the next chapter, we will use these results to derive the spectrum of a squeezed vacuum source which consists of a cavity with a nonlinear medium inside.

Squeezing spectra

The Hamiltonian that describes our squeezing cavity with a nonlinear crystal inside is given by the sum of a Hamiltonian describing the empty cavity and an interaction Hamiltonian that describes how the pump field interacts with the cavity modes ([Wal08], p. 136)

$$\hat{H}_{\mathrm{sys}} = \hbar\nu\hat{a}^{\dagger}\left(t\right)\hat{a}\left(t\right) + \frac{\mathrm{i}}{2}\hbar\left[\epsilon\hat{a}^{\dagger 2}\left(t\right) - \epsilon^{*}\hat{a}^{2}\left(t\right)\right]. \tag{2.80}$$

Here, the pump field $\epsilon = |\epsilon|\,\mathrm{e}^{-\mathrm{i}(\nu_{\mathrm{p}}t+\phi)}$ with $\nu_{\mathrm{p}} = 2\nu$ and phase ϕ is treated classically. This approximation is justified by the assumption that the pump is not depleted by the nonlinear interaction that generates the squeezed vacuum. Using equation (2.77), we obtain for the commutator

$$\begin{aligned}
-\frac{\mathrm{i}}{\hbar}\left[\hat{a}\left(t\right), \hat{H}_{\mathrm{sys}}\right] &= -\frac{\mathrm{i}}{\hbar}\left[\hat{a}\left(t\right)\hat{H}_{\mathrm{sys}} - \hat{H}_{\mathrm{sys}}\hat{a}\left(t\right)\right] \\
&= -\frac{\mathrm{i}}{\hbar}\Big[\hat{a}\left(t\right)\left(\hbar\nu\hat{a}^{\dagger}\left(t\right)\hat{a}\left(t\right) + \frac{\mathrm{i}}{2}\hbar\left(\epsilon\hat{a}^{\dagger 2}\left(t\right) - \epsilon^{*}\hat{a}^{2}\left(t\right)\right)\right) \\
&\qquad - \left(\hbar\nu\hat{a}^{\dagger}\left(t\right)\hat{a}\left(t\right) + \frac{\mathrm{i}}{2}\hbar\left(\epsilon\hat{a}^{\dagger 2}\left(t\right) - \epsilon^{*}\hat{a}^{2}\left(t\right)\right)\right)\hat{a}\left(t\right)\Big] \\
&= -\mathrm{i}\nu\hat{a}\left(t\right) + \epsilon\hat{a}^{\dagger}\left(t\right)
\end{aligned}$$

and in total

$$\frac{d}{dt}\hat{a}\left(t\right) = -\mathrm{i}\nu\hat{a}\left(t\right) + \epsilon\hat{a}^{\dagger}\left(t\right) - \frac{\gamma}{2}\hat{a}\left(t\right) + \sqrt{\gamma}\hat{a}_{\mathrm{in}}\left(t\right). \tag{2.81}$$

Transforming this equation to a frame rotating with ν yields:

$$\frac{d}{dt}\hat{a}\left(t\right) = \epsilon\hat{a}^{\dagger}\left(t\right) - \frac{\gamma}{2}\hat{a}\left(t\right) + \sqrt{\gamma}\hat{a}_{\mathrm{in}}\left(t\right) \tag{2.82}$$

Since $\omega = \Omega + \nu$ and $\nu \gg \Omega$, we substitute $\omega \to \Omega$ in the rotating frame. We define the intracavity modes to be ([Bau16], p. 85)

$$\hat{a}\left(t\right) = \frac{1}{\sqrt{2\pi}}\int_{-\infty}^{\infty} d\omega\, \mathrm{e}^{-\mathrm{i}\omega t}\hat{a}\left(\omega\right) \tag{2.83}$$

$$\begin{aligned}\hat{a}^{\dagger}\left(t\right) &= \frac{1}{\sqrt{2\pi}}\int_{-\infty}^{\infty} d\omega\, \mathrm{e}^{\mathrm{i}\omega t}\hat{a}^{\dagger}\left(\omega\right)\\ &= \frac{1}{\sqrt{2\pi}}\int_{-\infty}^{\infty} d\omega\, \mathrm{e}^{-\mathrm{i}\omega t}\hat{a}^{\dagger}\left(-\omega\right).\end{aligned} \tag{2.84}$$

With this definition, we get

$$\begin{aligned}\left[\hat{a}\left(\omega\right), \hat{a}^{\dagger}\left(\omega'\right)\right] &= \frac{1}{2\pi}\int_{-\infty}^{\infty}\int_{-\infty}^{\infty} dt\, dt' \mathrm{e}^{\mathrm{i}\left(\omega t - \omega' t'\right)} \left[\hat{a}\left(t\right), \hat{a}^{\dagger}\left(t'\right)\right]\\ &= \frac{1}{2\pi}\int_{-\infty}^{\infty}\int_{-\infty}^{\infty} dt\, dt' \mathrm{e}^{\mathrm{i}\left(\omega t - \omega' t'\right)}\delta\left(t - t'\right)\\ &= \frac{1}{2\pi}\int_{-\infty}^{\infty} dt\, \mathrm{e}^{\mathrm{i}\left(\omega - \omega'\right)t}\\ &= \delta\left(\omega - \omega'\right)\end{aligned} \tag{2.85}$$

for the commutator of the modes in frequency space. We used the definition ([Sch06], p. 137)

$$\frac{1}{2\pi}\int_{-\infty}^{\infty} dk\, \mathrm{e}^{\mathrm{i}kx} = \delta\left(x\right) \tag{2.86}$$

for the delta function. Inserting $\hat{a}\left(t\right)$ and $\hat{a}^{\dagger}\left(t\right)$ into equation (2.82) results in

$$\begin{aligned}\frac{d}{dt}\frac{1}{\sqrt{2\pi}}\int_{-\infty}^{\infty} d\omega\, \mathrm{e}^{-\mathrm{i}\omega t}\hat{a}\left(\omega\right) =& \epsilon\frac{1}{\sqrt{2\pi}}\int_{-\infty}^{\infty} d\omega\, \mathrm{e}^{\mathrm{i}\omega t}\hat{a}^{\dagger}\left(\omega\right)\\ &- \frac{\gamma}{2}\frac{1}{\sqrt{2\pi}}\int_{-\infty}^{\infty} d\omega\, \mathrm{e}^{-\mathrm{i}\omega t}\hat{a}\left(\omega\right)\\ &+ \sqrt{\gamma}\frac{1}{\sqrt{2\pi}}\int_{-\infty}^{\infty} d\omega\, \mathrm{e}^{-\mathrm{i}\omega t}\hat{a}_{\mathrm{in}}\left(\omega\right).\end{aligned}$$

Performing the temporal differentiation on the left and comparing the coefficients on the left and right side of the equation with each other leads to the fourier transformed differential equation

$$-\mathrm{i}\omega\hat{a}\left(\omega\right) = \epsilon\hat{a}^{\dagger}\left(-\omega\right) - \frac{\gamma}{2}\hat{a}\left(\omega\right) + \sqrt{\gamma}\hat{a}_{\mathrm{in}}\left(\omega\right)$$

The differential equation for the complex conjugate is

$$\mathrm{i}\omega\hat{a}^{\dagger}(\omega) = \epsilon^{*}\hat{a}(-\omega) - \frac{\gamma}{2}\hat{a}^{\dagger}(\omega) + \sqrt{\gamma}\hat{a}_{\mathrm{in}}^{\dagger}(\omega).$$

With the replacement $\omega \to -\omega$ we get

$$-\mathrm{i}\omega\hat{a}^{\dagger}(-\omega) = \epsilon^{*}\hat{a}(\omega) - \frac{\gamma}{2}\hat{a}^{\dagger}(-\omega) + \sqrt{\gamma}\hat{a}_{\mathrm{in}}^{\dagger}(-\omega)$$

and can write the combined equations in matrix form [Col84]:

$$\mathbf{A}\begin{pmatrix}\hat{a}(\omega)\\ \hat{a}^{\dagger}(-\omega)\end{pmatrix} = \begin{pmatrix}\frac{\gamma}{2}-\mathrm{i}\omega & -\epsilon\\ -\epsilon^{*} & \frac{\gamma}{2}-\mathrm{i}\omega\end{pmatrix}\begin{pmatrix}\hat{a}(\omega)\\ \hat{a}^{\dagger}(-\omega)\end{pmatrix} = \sqrt{\gamma}\begin{pmatrix}\hat{a}_{\mathrm{in}}(\omega)\\ \hat{a}_{\mathrm{in}}^{\dagger}(-\omega)\end{pmatrix}$$

With the inverse of $\mathbf{A}$, we can calculate the intracavity modes and obtain

$$\begin{pmatrix}\hat{a}(\omega)\\ \hat{a}^{\dagger}(-\omega)\end{pmatrix} = \sqrt{\gamma}\begin{pmatrix}\frac{\frac{\gamma}{2}-\mathrm{i}\omega}{\left(\frac{\gamma}{2}-\mathrm{i}\omega\right)^{2}-|\epsilon|^{2}} & \frac{\epsilon}{\left(\frac{\gamma}{2}-\mathrm{i}\omega\right)^{2}-|\epsilon|^{2}}\\ \frac{\epsilon^{*}}{\left(\frac{\gamma}{2}-\mathrm{i}\omega\right)^{2}-|\epsilon|^{2}} & \frac{\frac{\gamma}{2}-\mathrm{i}\omega}{\left(\frac{\gamma}{2}-\mathrm{i}\omega\right)^{2}-|\epsilon|^{2}}\end{pmatrix}\begin{pmatrix}\hat{a}_{\mathrm{in}}(\omega)\\ \hat{a}_{\mathrm{in}}^{\dagger}(-\omega)\end{pmatrix}. \tag{2.87}$$

We can now transform equation (2.79) into frequency space:

$$\sqrt{\gamma}\hat{a}(\omega) = \hat{a}_{\mathrm{in}}(\omega) + \hat{a}_{\mathrm{out}}(\omega) \tag{2.88}$$

and calculate the output operators in dependence of the input field to be

$$\begin{aligned}\hat{a}_{\mathrm{out}}(\omega) =& \sqrt{\gamma}\hat{a}(\omega) - \hat{a}_{\mathrm{in}}(\omega)\\ =& \sqrt{\gamma}\left(\frac{\left(\frac{\gamma}{2}-\mathrm{i}\omega\right)\sqrt{\gamma}\hat{a}_{\mathrm{in}}(\omega)}{\left(\frac{\gamma}{2}-\mathrm{i}\omega\right)^{2}-|\epsilon|^{2}} + \frac{\epsilon\sqrt{\gamma}\hat{a}_{\mathrm{in}}^{\dagger}(-\omega)}{\left(\frac{\gamma}{2}-\mathrm{i}\omega\right)^{2}-|\epsilon|^{2}}\right) - \hat{a}_{\mathrm{in}}(\omega)\\ =& \frac{\left(\frac{\gamma^{2}}{4}+\omega^{2}+|\epsilon|^{2}\right)\hat{a}_{\mathrm{in}}(\omega) + \epsilon\gamma\hat{a}_{\mathrm{in}}^{\dagger}(-\omega)}{\left(\frac{\gamma}{2}-\mathrm{i}\omega\right)^{2}-|\epsilon|^{2}}.\end{aligned} \tag{2.89}$$

The complex conjugate is

$$\hat{a}_{\mathrm{out}}^{\dagger}(\omega) = \frac{\left(\frac{\gamma^{2}}{4}+\omega^{2}+|\epsilon|^{2}\right)\hat{a}_{\mathrm{in}}^{\dagger}(\omega) + \epsilon^{*}\gamma\hat{a}_{\mathrm{in}}(-\omega)}{\left(\frac{\gamma}{2}+i\omega\right)^{2}-|\epsilon|^{2}}. \tag{2.90}$$

The variances of the fields are defined by $\langle\hat{a},\hat{b}\rangle = \langle\hat{a}\hat{b}\rangle - \langle\hat{a}\rangle\langle\hat{b}\rangle$. The output field that is described by equation (2.89) and (2.90) only depends on the input field, which is in a vaccum state in our experiment and thus has zero mean. For that reason, the variance can be calculated by $\langle\hat{a},\hat{b}\rangle = \langle\hat{a}\hat{b}\rangle$ ([Col84], [Bau16], p.86).

$$\begin{aligned}\langle\hat{a}_{\mathrm{out}}^{\dagger}(\omega),\hat{a}_{\mathrm{out}}(\omega')\rangle =& \Bigg\langle \left(\frac{\left(\frac{\gamma^{2}}{4}+\omega^{2}+|\epsilon|^{2}\right)\hat{a}_{\mathrm{in}}^{\dagger}(\omega) + \epsilon^{*}\gamma\hat{a}_{\mathrm{in}}(-\omega)}{\left(\frac{\gamma}{2}+\mathrm{i}\omega\right)^{2}-|\epsilon|^{2}}\right)\\ &\times\left(\frac{\left(\frac{\gamma^{2}}{4}+\omega'^{2}+|\epsilon|^{2}\right)\hat{a}_{\mathrm{in}}(\omega') + \epsilon\gamma\hat{a}_{\mathrm{in}}^{\dagger}(-\omega')}{\left(\frac{\gamma}{2}-\mathrm{i}\omega'\right)^{2}-|\epsilon|^{2}}\right)\Bigg\rangle\end{aligned} \tag{2.91}$$

The terms $\langle 0|\hat{a}_{\text{in}}^{\dagger}(\omega)\,\hat{a}_{\text{in}}(\omega')\,|0\rangle$, $\langle 0|\hat{a}_{\text{in}}^{\dagger}(\omega)\,\hat{a}_{\text{in}}^{\dagger}(-\omega')\,|0\rangle$ and $\langle 0|\hat{a}_{\text{in}}(-\omega)\,\hat{a}_{\text{in}}(\omega')\,|0\rangle$ give a zero contribution since equation (2.10) holds and the input state is in a vacuum. Thus, only the term $\langle 0|\hat{a}_{\text{in}}(-\omega)\,\hat{a}_{\text{in}}^{\dagger}(-\omega')\,|0\rangle$ remains and contributes to the variance via the commutation relation (2.85):

$$
\begin{aligned}
\left\langle \hat{a}_{\text{out}}^{\dagger}(\omega)\,,\hat{a}_{\text{out}}(\omega')\right\rangle =&\left\langle \frac{\epsilon^{*}\gamma\hat{a}_{\text{in}}(-\omega)}{\left(\left(\frac{\gamma}{2}+\mathrm{i}\omega\right)^{2}-|\epsilon|^{2}\right)}\times\frac{\epsilon\gamma\hat{a}_{\text{in}}^{\dagger}(-\omega')}{\left(\left(\frac{\gamma}{2}-\mathrm{i}\omega'\right)^{2}-|\epsilon|^{2}\right)}\right\rangle \\
=&\left\langle \frac{|\epsilon|^{2}\gamma^{2}\left(\delta(\omega-\omega')+\hat{a}_{\text{in}}^{\dagger}(-\omega)\,\hat{a}_{\text{in}}(-\omega')\right)}{\left(\left(\frac{\gamma}{2}+\mathrm{i}\omega\right)^{2}-|\epsilon|^{2}\right)\left(\left(\frac{\gamma}{2}-\mathrm{i}\omega'\right)^{2}-|\epsilon|^{2}\right)}\right\rangle \\
=&\frac{|\epsilon|^{2}\gamma^{2}}{\left(\left(\frac{\gamma}{2}+\mathrm{i}\omega\right)^{2}-|\epsilon|^{2}\right)\left(\left(\frac{\gamma}{2}-\mathrm{i}\omega\right)^{2}-|\epsilon|^{2}\right)}\delta(\omega-\omega') \\
=&\frac{|\epsilon|\,\gamma}{2}\left(\frac{1}{\left(\frac{\gamma}{2}-|\epsilon|\right)^{2}+\omega^{2}}-\frac{1}{\left(\frac{\gamma}{2}+|\epsilon|\right)^{2}+\omega^{2}}\right)\delta(\omega-\omega')\,. \qquad (2.92)
\end{aligned}
$$

In a similar way, we get

$$
\begin{aligned}
\left\langle \hat{a}_{\text{out}}(\omega)\,\hat{a}_{\text{out}}(\omega')\right\rangle =&\left\langle \left(\frac{\left(\frac{\gamma^{2}}{4}+\omega^{2}+|\epsilon|^{2}\right)\hat{a}_{\text{in}}(\omega)+\epsilon\gamma\hat{a}_{\text{in}}^{\dagger}(-\omega)}{\left(\frac{\gamma}{2}-\mathrm{i}\omega\right)^{2}-|\epsilon|^{2}}\right)\right. \\
&\left.\times\left(\frac{\left(\frac{\gamma^{2}}{4}+\omega'^{2}+|\epsilon|^{2}\right)\hat{a}_{\text{in}}(\omega')+\epsilon\gamma\hat{a}_{\text{in}}^{\dagger}(-\omega')}{\left(\frac{\gamma}{2}-\mathrm{i}\omega'\right)^{2}-|\epsilon|^{2}}\right)\right\rangle \\
=&\left\langle \frac{\left(\frac{\gamma^{2}}{4}+\omega^{2}+|\epsilon|^{2}\right)\hat{a}_{\text{in}}(\omega)}{\left(\frac{\gamma}{2}-\mathrm{i}\omega\right)^{2}-|\epsilon|^{2}}\times\frac{\epsilon\gamma\hat{a}_{\text{in}}^{\dagger}(-\omega')}{\left(\frac{\gamma}{2}-\mathrm{i}\omega'\right)^{2}-|\epsilon|^{2}}\right\rangle \\
=&\frac{\left(\frac{\gamma^{2}}{4}+\omega^{2}+|\epsilon|^{2}\right)\epsilon\gamma}{\left(\left(\frac{\gamma}{2}-\mathrm{i}\omega\right)^{2}-|\epsilon|^{2}\right)\left(\left(\frac{\gamma}{2}+\mathrm{i}\omega\right)^{2}-|\epsilon|^{2}\right)}\delta(\omega+\omega')\,. \\
=&\frac{\epsilon\gamma}{2}\left(\frac{1}{\left(\frac{\gamma}{2}-|\epsilon|\right)^{2}+\omega^{2}}+\frac{1}{\left(\frac{\gamma}{2}+|\epsilon|\right)^{2}+\omega^{2}}\right)\delta(\omega+\omega')\,. \qquad (2.93)
\end{aligned}
$$

To calculate the spectrum in the output amplitude and phase quadrature, we introduce the quadrature operators as before:

$$\hat{X}_{1,\text{out}}=\hat{a}_{\text{out}}^{\dagger}+\hat{a}_{\text{out}} \qquad (2.94)$$

$$\hat{X}_{2,\text{out}}=\mathrm{i}\left(\hat{a}_{\text{out}}^{\dagger}-\hat{a}_{\text{out}}\right)\,. \qquad (2.95)$$

We are interested in the variances of these quadrature operators, since they can be directly measured with a spectrum analyzer in the experiment. They are given by

$$
\begin{aligned}
\left\langle \hat{X}_{1,\mathrm{out}}(\omega), \hat{X}_{1,\mathrm{out}}(\omega')\right\rangle =& \left\langle \left(\hat{a}^{\dagger}_{\mathrm{out}}(\omega)+\hat{a}_{\mathrm{out}}(\omega)\right)\left(\hat{a}^{\dagger}_{\mathrm{out}}(\omega')+\hat{a}_{\mathrm{out}}(\omega')\right)\right\rangle \\
=& \Big\langle \hat{a}^{\dagger}_{\mathrm{out}}(\omega)\hat{a}^{\dagger}_{\mathrm{out}}(\omega')+\hat{a}^{\dagger}_{\mathrm{out}}(\omega)\hat{a}_{\mathrm{out}}(\omega')+\delta(\omega-\omega') \\
&+\hat{a}^{\dagger}_{\mathrm{out}}(\omega)\hat{a}_{\mathrm{out}}(\omega')+\hat{a}_{\mathrm{out}}(\omega)\hat{a}_{\mathrm{out}}(\omega')\Big\rangle \\
=& \left\langle \left(\hat{a}_{\mathrm{out}}(\omega)\hat{a}_{\mathrm{out}}(\omega')\right)^{\dagger}\right\rangle+\left\langle \hat{a}_{\mathrm{out}}(\omega)\hat{a}_{\mathrm{out}}(\omega')\right\rangle \\
&+2\left\langle \hat{a}^{\dagger}_{\mathrm{out}}(\omega)\hat{a}_{\mathrm{out}}(\omega')\right\rangle+\delta(\omega-\omega') \\
=& \frac{|\epsilon|\gamma}{2}\left(\frac{1}{\left(\frac{\gamma}{2}-|\epsilon|\right)^2+\omega^2}+\frac{1}{\left(\frac{\gamma}{2}+|\epsilon|\right)^2+\omega^2}\right)\mathrm{e}^{-\mathrm{i}\phi}\delta(\omega+\omega') \\
&+\frac{|\epsilon|\gamma}{2}\left(\frac{1}{\left(\frac{\gamma}{2}-|\epsilon|\right)^2+\omega^2}+\frac{1}{\left(\frac{\gamma}{2}+|\epsilon|\right)^2+\omega^2}\right)\mathrm{e}^{\mathrm{i}\phi}\delta(\omega+\omega') \\
&+|\epsilon|\gamma\left(\frac{1}{\left(\frac{\gamma}{2}-|\epsilon|\right)^2+\omega^2}-\frac{1}{\left(\frac{\gamma}{2}+|\epsilon|\right)^2+\omega^2}\right)\delta(\omega-\omega') \\
&+\delta(\omega-\omega') \\
=& \left(\frac{|\epsilon|\gamma}{\left(\frac{\gamma}{2}-|\epsilon|\right)^2+\omega^2}+\frac{|\epsilon|\gamma}{\left(\frac{\gamma}{2}+|\epsilon|\right)^2+\omega^2}\right)\cos(\phi)\,\delta(\omega+\omega') \\
&+|\epsilon|\gamma\left(\frac{1}{\left(\frac{\gamma}{2}-|\epsilon|\right)^2+\omega^2}-\frac{1}{\left(\frac{\gamma}{2}+|\epsilon|\right)^2+\omega^2}\right)\delta(\omega-\omega') \\
&+\delta(\omega-\omega').
\end{aligned}
$$

Here, we made use of the relation $\delta(x)=\delta(-x)$. Integration over ω' gives the single sided spectrum

$$S_{\mathrm{X_1,X_1}}(\phi,\omega)=1+\frac{|\epsilon|\gamma(\cos(\phi)+1)}{\left(\frac{\gamma}{2}-|\epsilon|\right)^2+\omega^2}+\frac{|\epsilon|\gamma(\cos(\phi)-1)}{\left(\frac{\gamma}{2}+|\epsilon|\right)^2+\omega^2} \tag{2.96}$$

For a pump phase of $\phi=\pi$, the first term vanishes and we see that the variance of $\hat{X}_1$ is smaller than one:

$$S_{\mathrm{X_1,X_1}}(\pi,\omega)=1-\frac{2|\epsilon|\gamma}{\left(\frac{\gamma}{2}+|\epsilon|\right)^2+\omega^2}. \tag{2.97}$$

The quadrature is squeezed compared to the vacuum reference level of one. For $\phi=0$, the variance would increase to values larger than one. In a similar fashion, we can calculate the variance for $\hat{X}_{2,\mathrm{out}}(\omega)$ to be

$$\begin{aligned}
\left\langle \hat{X}_{2,\mathrm{out}}(\omega), \hat{X}_{2,\mathrm{out}}(\omega')\right\rangle =& \Big\langle -\left(\hat{a}_{\mathrm{out}}(\omega)\hat{a}_{\mathrm{out}}(\omega')\right)^{\dagger} + 2\hat{a}^{\dagger}_{\mathrm{out}}(\omega)\hat{a}_{\mathrm{out}}(\omega') \\
& - \hat{a}_{\mathrm{out}}(\omega)\hat{a}_{\mathrm{out}}(\omega') + \delta(\omega-\omega')\Big\rangle \\
=& -|\epsilon|\gamma\cos(\phi)\left(\frac{1}{\left(\frac{\gamma}{2}-|\epsilon|\right)^2+\omega^2}+\frac{1}{\left(\frac{\gamma}{2}+|\epsilon|\right)^2+\omega^2}\right)\delta(\omega+\omega') \\
& + |\epsilon|\gamma\left(\frac{1}{\left(\frac{\gamma}{2}-|\epsilon|\right)^2+\omega^2}-\frac{1}{\left(\frac{\gamma}{2}+|\epsilon|\right)^2+\omega^2}\right)\delta(\omega-\omega') \\
& + \delta(\omega-\omega').
\end{aligned}$$

Integration over ω' yields:

$$S_{\mathrm{X_2,X_2}}(\phi,\omega) = 1 + \frac{|\epsilon|\gamma(1-\cos(\phi))}{\left(\frac{\gamma}{2}-|\epsilon|\right)^2+\omega^2} + \frac{|\epsilon|\gamma(-\cos(\phi)-1)}{\left(\frac{\gamma}{2}+|\epsilon|\right)^2+\omega^2}. \tag{2.98}$$

For a pump phase of $\phi = 0$, we see that $\hat{X}_2$ is squeezed, showing the same spectrum as before:

$$S_{\mathrm{X_2,X_2}}(0,\omega) = 1 - \frac{2|\epsilon|\gamma}{\left(\frac{\gamma}{2}+|\epsilon|\right)^2+\omega^2}. \tag{2.99}$$

For $\phi = \pi$, the variance is increased to values larger than one, which means that the quadrature is anti-squeezed:

$$\begin{aligned}
S_{\mathrm{X_2,X_2}}(\pi,\omega) &= 1 + \frac{2|\epsilon|\gamma}{\left(\frac{\gamma}{2}-|\epsilon|\right)^2+\omega^2} \\
&= 1 + \frac{4\frac{2|\epsilon|}{\gamma}}{\left(1-\frac{2|\epsilon|}{\gamma}\right)^2+4\left(\frac{\omega}{\gamma}\right)^2}
\end{aligned} \tag{2.100}$$

Squeezed states are generated in a degenerate parametric down-conversion cavity if the pump power is smaller than the oscillation threshold. Above this lasing threshold, a bright coherent field would be produced. The threshold is defined by the anti-squeezed spectrum converging to infinity at $\omega = 0$. From equation (2.100), we can deduce that this is the case for $1 - \frac{2|\epsilon|}{\gamma} \to 0$. Thus, we can set $|\epsilon|_{\mathrm{thr}} = \frac{\gamma}{2}$ or $\frac{1}{|\epsilon|_{\mathrm{thr}}} = \frac{2}{\gamma}$. Multiplying this equation with $|\epsilon|$ and expressing the pump amplitudes in terms of powers according to $|\epsilon| = \sqrt{P}$ results in $\sqrt{\frac{P}{P_{\mathrm{thr}}}} = \frac{|\epsilon|}{|\epsilon|_{\mathrm{thr}}} = \frac{2|\epsilon|}{\gamma}$. With this substitution and $\omega = 2\pi f$, we see that the spectra for orthogonally squeezed and anti-squeezed quadratures are

$$S_{\mathrm{sqz,asqz}}(f) = 1 \mp \frac{4\sqrt{\frac{P}{P_{\mathrm{thr}}}}}{\left(1 \pm \sqrt{\frac{P}{P_{\mathrm{thr}}}}\right)^2 + 4\left(\frac{2\pi f}{\gamma}\right)^2}. \tag{2.101}$$

Here, f is the Fourier frequency, which is directly displayed by a spectrum analyzer. Spectra of the squeezed and anti-squeezed quadrature are depicted in figure 2.9 for a cavity with $\frac{\gamma}{2\pi} = 100\,\mathrm{MHz}$. The closer the pump power P gets to the threshold for parametric oscillation, the stronger the squeezing level is. In terms of the photon number distribution depicted in figure 2.4, this means that the stronger nonlinear coupling resulting from high pump powers creates more photon pairs, leading to higher squeezing levels.

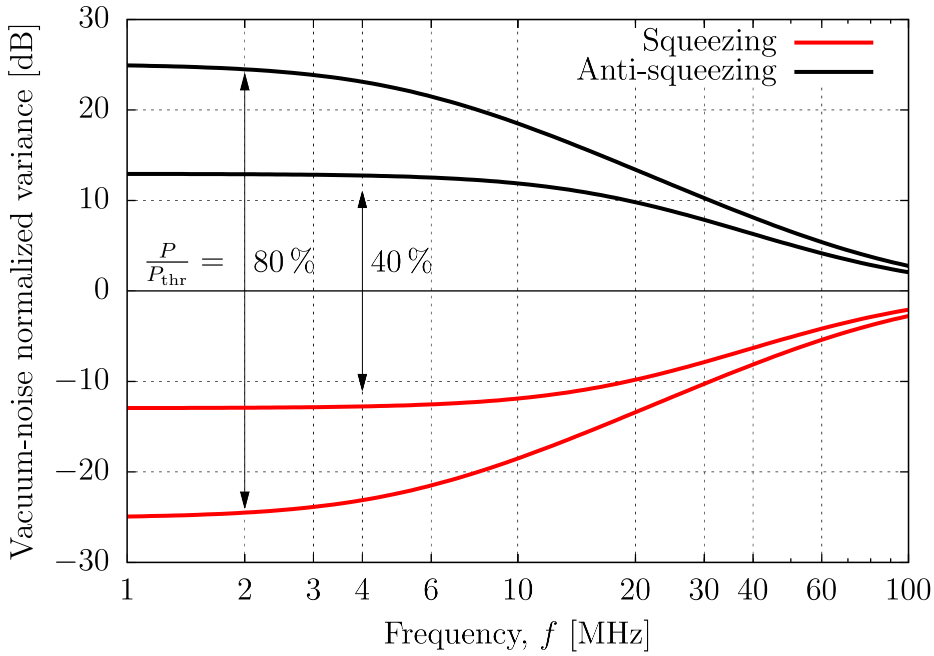

Figure 2.9: Spectra of the squeezed and anti-squeezed quadrature for different pump powers and a cavity with $\frac{\gamma}{2\pi} = 100\,\mathrm{MHz}$. The closer the pump power P is to the threshold for optical parametric oscillation P_{thr}, the more squeezing can be observed.

2.2.3 Effect of optical loss on squeezing

The previously presented theory of squeezed states of light assumes perfect optics and does not take into account any optical loss. In the experiment, optical loss, for example from absorption or scattering, leads to a loss of photons and reduces the amount of detectable squeezing. As described in the preceding sections, a squeezed state only contains even photon numbers since the nonlinear process of parametric down-conversion always creates photon pairs. This statistic breaks down if photons are lost. The higher the losses are, the more the actual state deviates from an ideal squeezed state. Figure 2.10 shows how optical losses can be modeled with a beam splitter.

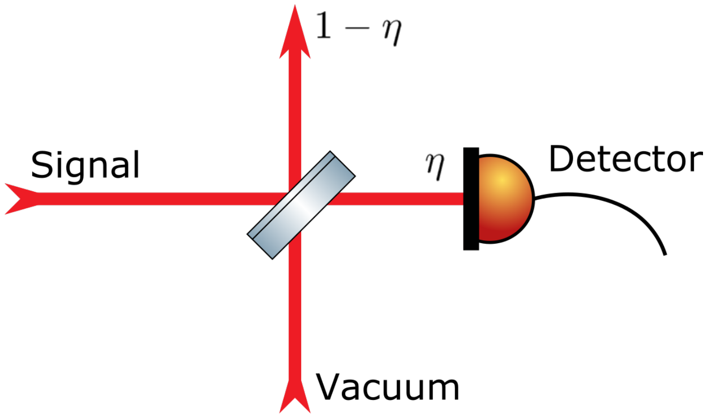

Figure 2.10: Model of optical loss with a beamsplitter. The losses are characterized by the efficiency η. When passing the beamsplitter, a fraction of $1-\eta$ photons are lost from the signal. This part of the signal is replaced by vacuum. In a squeezing experiment, this incoupling vacuum noise reduces the observable squeezing.

It transmits the fraction η of the signal's intensity. Thus, a fraction of $1-\eta$ of the incoming photons are lost ([Leo97], pp. 94ff.). These losses can also be understood as vacuum noise coupling into the squeezed state, reducing the squeezing level. Using the beam splitter relations ([Scu97], p. 126), we see that

$$\begin{aligned} S_{\eta,\mathrm{sqz}}(f) &= \eta \left(1 - \frac{4\sqrt{\frac{P}{P_{\mathrm{thr}}}}}{\left(1+\sqrt{\frac{P}{P_{\mathrm{thr}}}}\right)^2 + 4\left(\frac{2\pi f}{\gamma}\right)^2} \right) + (1-\eta) \\ &= 1 - \eta \frac{4\sqrt{\frac{P}{P_{\mathrm{thr}}}}}{\left(1+\sqrt{\frac{P}{P_{\mathrm{thr}}}}\right)^2 + 4\left(\frac{2\pi f}{\gamma}\right)^2} \end{aligned}$$

For $P = 0$, the formula reproduces the variance of the vacuum, which is normalized to one. For anti-squeezing, we get a similar formula. In total, we get

$$S_{\eta,\mathrm{sqz,asqz}}(f) = 1 \mp \eta \frac{4\sqrt{\frac{P}{P_{\mathrm{thr}}}}}{\left(1\pm\sqrt{\frac{P}{P_{\mathrm{thr}}}}\right)^2 + 4\left(\frac{2\pi f}{\gamma}\right)^2}. \tag{2.102}$$

for a squeezing measurement with losses [Vah16]. Figure 2.11 illustrates the effect of losses on the squeezing spectrum. For the plot, the values $\frac{\gamma}{2\pi} = 100\,\mathrm{MHz}$, $\frac{P}{P_{\mathrm{thr}}} = 80\,\%$ and $\eta = 0.95$ were inserted into equation (2.102). The squeezing level is reduced significantly, while the anti-squeezed variance is hardly affected. Thus, it is important to reduce the optical losses of a squeezing experiment to achieve high levels of quantum noise reduction.

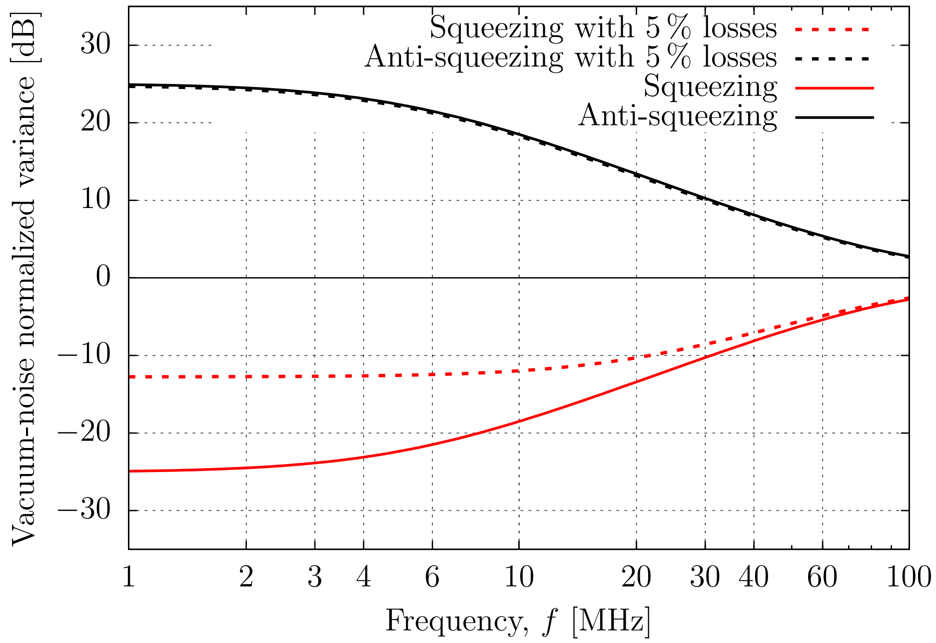

Figure 2.11: Effect of losses on the squeezing spectrum. The plot shows the spectra for the squeezed and anti-squeezed quadrature according to equation (2.102) for $\frac{\gamma}{2\pi} = 100\,\text{MHz}$ and $\frac{P}{P_{\text{thr}}} = 80\,\%$ with $\eta = 0.95$. The loss mostly affects the squeezed quadrature and reduces the measurable squeezing significantly. The effect on the anti-squeezed quadrature is negligible in this example.

2.2.4 Phase matching

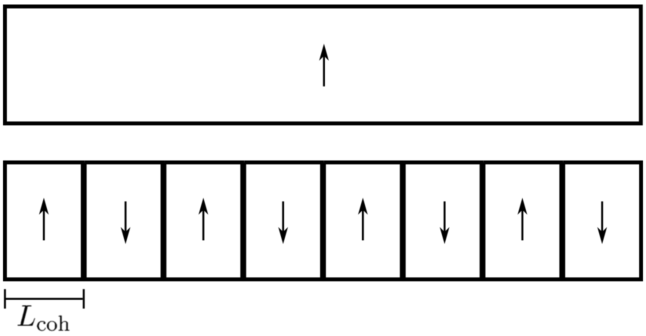

Figure 2.12: Nonlinear crystal (top picture) and periodically poled nonlinear crystal (bottom picture). The sign of the effective nonlinearity d_{eff} changes periodically in a quasi phase matched crystal, leading to a builtup of the signal amplitude across its complete length. In contrast, the sign of d_{eff} is constant in a crystal that is not periodically poled and its birefringence has to be used for phase matching ([Boy08], p. 85).

For efficient second-harmonic generation and parametric down-conversion, the optimization of phase matching between the pump and signal field is important. The pump field induces the generation of the signal wave at every point in the nonlinear material. The signal travels with a speed that is determined by the refractive index n_s. Due to normal dispersion, the pump field travels with a different velocity which is determined by n_p. Good phase matching ensures that both fields travel with the same speed within the nonlinear material. Thus, constructive interference of the newly generated signal wave with the one that has been generated previously in the crystal is ensured at every point in the nonlinear medium. This leads to an increasing amplitude of the signal field and thus maximum output power ([Dem06], pp. 254–256, [Fej92]). As introduced in equations (2.53) and (2.54), the phase mismatch for second-harmonic generation in the plane wave approximation is given by $\Delta k = 2k_1 - k_2$. This also holds for the degenerate squeezed-light source used in this thesis ([Vah08a], p. 29). The phase matching condition can be rewritten in the following form:

$$\begin{aligned} \Delta k &= 2k_1 - k_2 = 0 \\ \Rightarrow \frac{n_2 \nu_2}{c_2} &= 2\frac{n_1 \nu_1}{c_1}. \end{aligned}$$

Since $\nu_2 = 2\nu_1$, $n_1 = n_2$ has to be satisfied for perfect phase matching. If both refractive indices are the same, both waves travel with the same speed within the crystal and constructive interference takes place over its full length. This can be achieved by exploiting the birefringence of a nonlinear material with different refractive indices for the ordinary and extraordinary polarization ([Boy08], pp. 79ff., [Dem06], pp. 254–256). However, birefringence based methods are rather complicated to implement experimentally, which is the reason why the technique of quasi phase matching was used within this thesis. A nonlinear crystal that is optimized for quasi phase matching is segmented into several domains across its length and the sign of the effective second order nonlinearity d_{eff} is changed periodically in every domain [Fej92]. This periodical poling is illustrated in figure 2.12. The upper scheme depicts a domain-free crystal which can only be phase matched exploiting its birefringence. The bottom scheme shows the domain structure of a crystal that is prepared for quasi-phase matching. The sign of d_{eff} is switched after the coherent builtup length L_{coh}, leading to an increasing signal amplitude across the complete length of the crystal, as shown qualitatively in figure 2.13. In the experiment, the domain length L_{coh} is optimized by heating the crystal and using its thermal expansion for temperature based fine tuning. This fine tuning also enables us to optimize the non-zero phase matching values that have to be taken into account when considering Gaussian beams, as mentioned before [Las07].

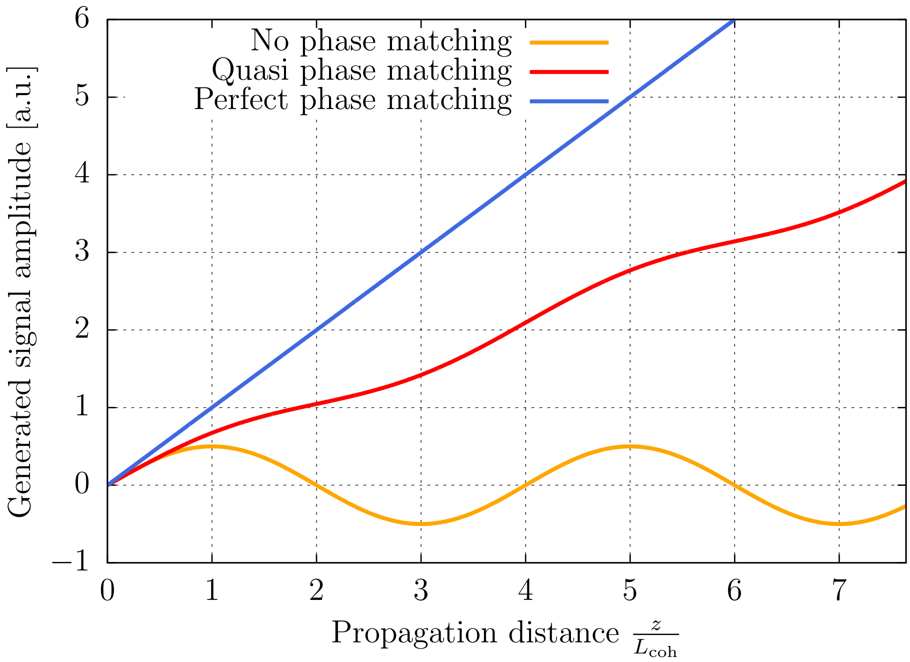

Figure 2.13: Qualitative illustration of the amplitude built-up of the signal field that is generated in a nonlinear, quasi-phase matched second order process. Without phasematching, the different velocities of the signal and pump field in the crystal would lead to an oscillating signal amplitude. Periodically changing the sign of the effective nonlinearity d_{eff} results in a constant built-up of the signal amplitude across the length of the crystal ([Boy08], p. 86).

3 Experimental setup

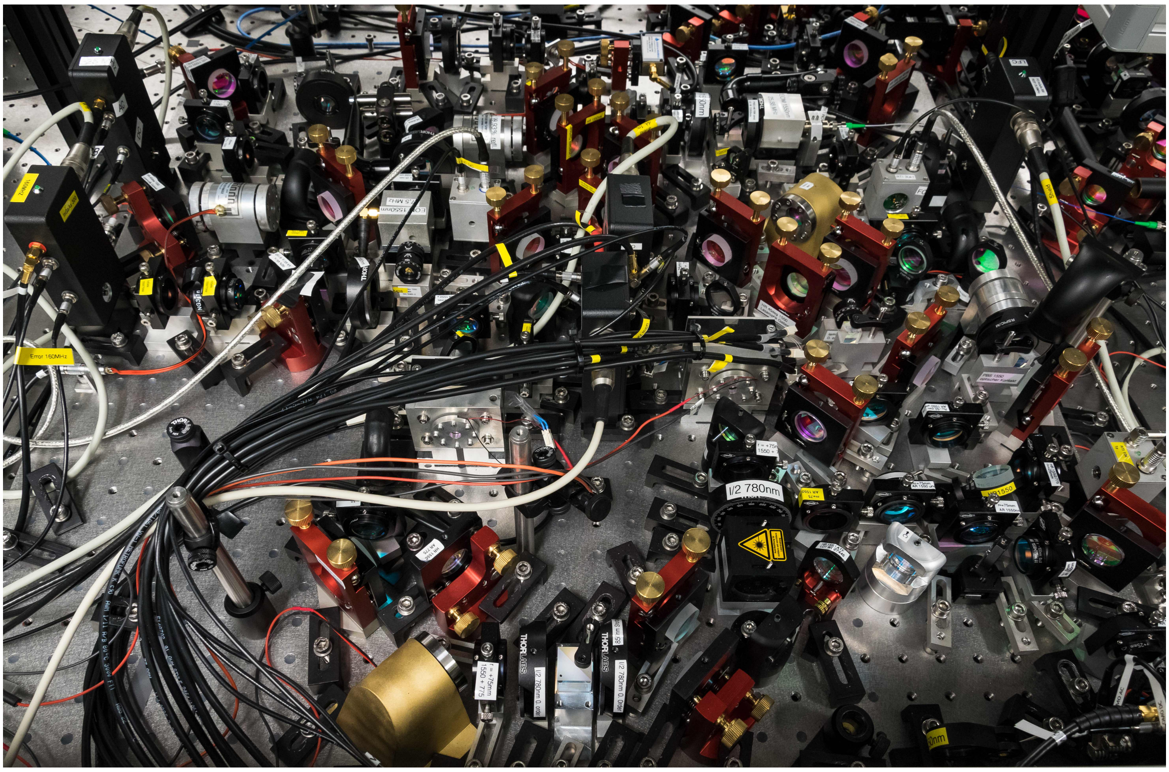

Figure 3.1: This figure shows a photograph of the breadboard with the experiment in the laboratory. The laser is coupled into the experiment in the top right corner. The angle of view is the same as in the schematics in figure 3.2.

The aim of the experiment presented in this thesis was to set up a source for strongly squeezed vacuum states of light at 1550 nm with a small footprint to allow for easy transportation and integration in other experiments. The setup to achieve this goal is based on experimental techniques that are presented in [Vah08a] and [Kha11] and led to the development of the squeezed-light source at 1064 nm that is used in the gravitational wave detector GEO600 [Aba11]. The setup that was developed within this thesis is depicted in figure 3.2 schematically. A photograph is shown in figure 3.1. It fits on a breadboard of 80 cm x 80 cm. To achieve this small footprint, various changes were implemented compared to the GEO600 squeezed-light source. In this experiment, only one external laser was used and coupled to the setup on the breadboard via a fiber coupler. All fields needed for the generation and characterization of squeezed vacuum states were generated from this source. Apart from that, short linear filter cavities were implemented. These cavities are more compact than the ring cavities that are used in the GEO600 source and are, for example, described in [Wil98]. A revised design of the second-harmonic generation and parametric down-conversion cavities was also implemented. It includes double resonance for both 1550 nm and 775 nm as well as a temperature gradient across the nonlinear crystal. The double resonance feature was already tested in other experiments [Vol13, Bau15], but it was found difficult to achieve simultaneous phase matching and double resonance for both fields. The temperature gradient that is generated by heating different parts of the nonlinear medium to unequal temperatures allows for a fine tuning of phase matching and simultaneous double resonance. A new approach for the single sideband generation scheme, comprising another filter cavity and passing an AOM twice, was implemented in this experiment as well. As shown in 3.2, the setup can be divided up into different subsections. The green area shows the laser preparation. A linear filter cavity was placed at the output of the NKT Photonics Koheras Boostik fibre laser to improve the spatial mode shape. The cavity waist was chosen such that the beam was in a collimated TEM00 mode for the downstream experiment. The laser preparation stage is followed by a second-harmonic generator (blue area), which converts the 1550 nm light from the laser to 775 nm. This wavelength is used to pump the parametric down-conversion cavity in the following red section. It generates the squeezed vacuum states that are analyzed with the homodyne detection scheme in the yellow area. To characterize the squeezed-light source at acoustic frequencies, the squeeze angle as well as the homodyne readout angle have to be stabilized with respect to each other. For that purpose, the coherent control scheme described in ([Vah08a], pp. 71ff., [Che07b]) was implemented. The single sideband that is needed for coherent control was generated and also spatially filtered in the orange section. The locks that stabilize the squeezing and readout angles were implemented as indicated in the grey areas. In the following, we describe the elements and techniques that were used in each of the experimental sections in more detail.

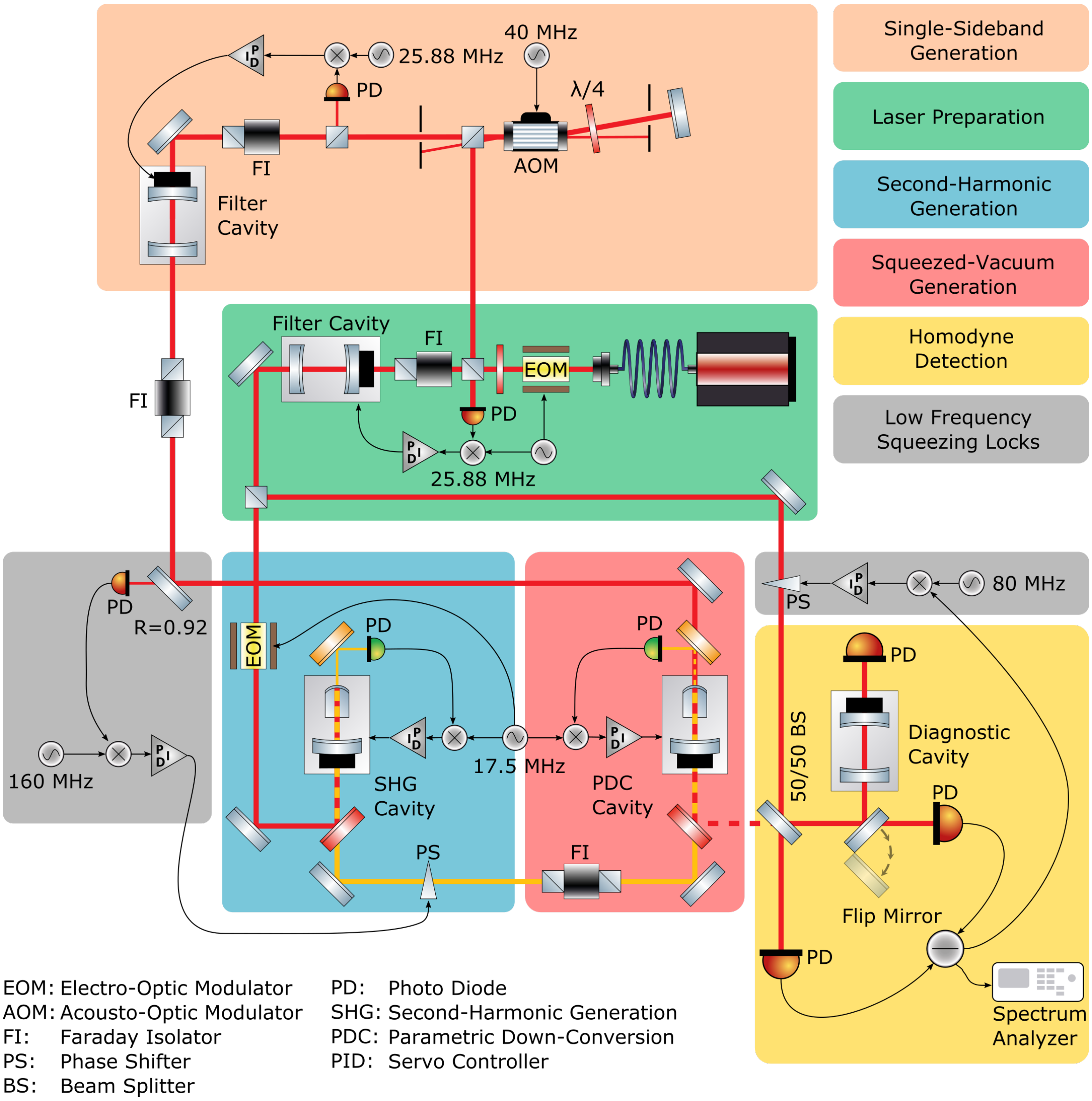

EOM: Electro-Optic Modulator
AOM: Acousto-Optic Modulator
FI: Faraday Isolator
PS: Phase Shifter
BS: Beam Splitter
PD: Photo Diode
SHG: Second-Harmonic Generation
PDC: Parametric Down-Conversion
PID: Servo Controller

Figure 3.2: Scheme of the experimental setup. The experiment can be divided up into different sections, as indicated by the different colors. First, the laser is prepared for the downstream experiment in the laser preparation stage (green). The second-harmonic pump field at 775 nm is generated afterwards (blue) and guided to the parametric down-conversion cavity that generates squeezed vacuum states (red). The squeezed states are characterized with a homodyne detector (yellow). The squeezed quadrature and the readout quadrature have to be stabilized with respect to each other for low frequency squeezing. For that purpose, the single sideband coherent control scheme was implemented in the experiment (grey). The sideband is generated by passing an acousto-optic modulator twice (orange).

3.1 Linear filter cavity

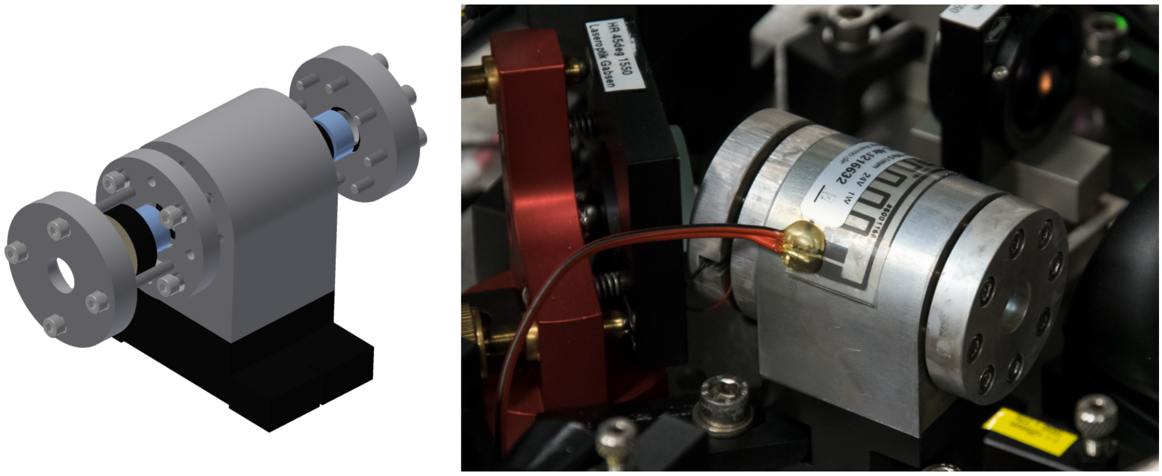

Figure 3.3: Drawing and picture of the linear filter cavity that was used in the experiment. A heating foil was glued to the curved surface on top of the spacer to compensate for temperature drifts.

The filter cavity, as depicted in figure 3.3, was used in the laser preparation stage and the single sideband generation section of the experiment. In the laser preparation stage, the cavity improves the spatial mode shape of the laser beam that is coming from the fiber. It also supresses technical noise at sideband frequencies exceeding the cavity's linewidth. This results in a shot noise limited beam for the measurements in the downstream experiment at those frequencies. In the single sideband generation section, a sideband of 80 MHz for the coherent control locking scheme is generated with an acousto-optic modulator. This beam is used to lock the homodyne readout angle to the squeezing angle. The spatial beam profile of this beam also has to be improved to obtain a TEM00 mode for the further application of the single sideband. Apart from that, the filter cavity suppresses photons at the DC laser frequency from the frequency-shifted beam, which is important for the measurement of squeezed states at acoustic frequencies. Details regarding this coherent control scheme will be explained in section 3.4. The filter cavity is a linear Fabry-Perot cavity with two plano-concave mirrors that have a radius of curvature of 10 m and a reflectivity or $R = 99.93\,\%$ on the curved side and an anti-reflective coating on the plane side. The separation between the two mirrors is 32.2 mm. These parameters result in a simulated full-width-half-maximum linewidth of 1.0345 MHz with a Finesse of 4486 and a waist size of 445 μm. The high finesse leads to the small linewidth that ensures the suppression of technical laser noise at sideband frequencies exceeding 1 MHz. The high radius of curvature of 10 m leads to the large waist, which ensures that the beam leaving the cavity is collimated. This makes it easier to handle and mode-match it to the cavities in the downstream experiment. To compensate for temperature drifts, a heating foil was attached to the cavity.

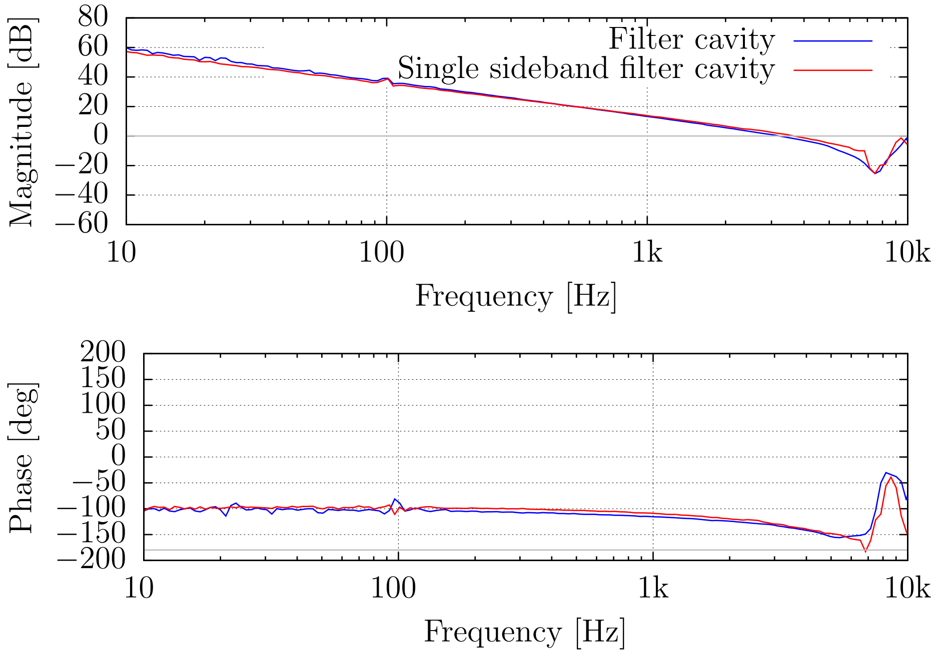

Figure 3.4: Bode plots of the open loop gain measurements of the filter cavities for the laser and the single sideband. Both cavities show a similar response with a maximal unity-gain frequency around 3 kHz.

Before the cavity length can be stabilized, the spacer has to be heated up until its length has increased by one free spectral range. This is the operating point at which the dissipation of heat to the environment allows for sufficient cooling of the cavity and thus an active temperature control is possible. The foil heats the mechanical spacer when the ambient temperature falls. The heating power is reduced when the ambient temperature rises. As a result, the temperature of the spacer and the distance between the mirrors remains constant. Temperature drifts occur at small frequencies, usually in the range of a few millihertz. In contrast to that, acoustics couple into the cavity at higher frequencies, around a few kilohertz. A piezo-electric actuator was integrated in the cavity to compensate for these fast disturbances. When a voltage is applied to the piezo, it expands and thus changes the cavity length. The higher the voltage, the larger is the expansion. Usually, high voltage amplifiers that reach up to 400 V are used. However, as slow length changes were compensated for by the heating foil, the output voltage of operational amplifiers of up to 13 V provided enough dynamical range to lock the filter cavities of this experiment for hours. The error signals for both the low frequency temperature control loop and the high frequency loop including the piezo-electric element were obtained with the Pound-Drever-Hall locking technique [Dre83, Bla01]. A phase modulation frequency of 25.88 MHz was chosen for that purpose and a maximal control loop bandwidth around 3 kHz was achieved, as the open loop gain measurements depicted in figure 3.4 show. In the homodyne detection section, a shorter version of this cavity was used as the reference for the alignment of the local oscillator and squeezed field on the balanced beamsplitter. This cavity was neither temperature stabilized nor locked since it was only necessary to scan its length during the alignment.

3.2 Second-harmonic generation and parametric down-conversion cavities

As described in section 2.2, the nonlinear processes of second-harmonic generation and parametric down-conversion are used for the generation of squeezed vacuum states at 1550 nm. The efficiency of these processes can be enhanced by placing the nonlinear material in a cavity. A hemilithic cavity that was resonant for both the fundamental and second-harmonic wavelengths of 1550 nm and 775 nm was successfully used in other experiments for second-harmonic and squeezing generation [Vol13]. The nonlinear PPKTP crystal used in these cavities has a curved backside with a highly reflective coating for both the second-harmonic and fundamental wavelengths. The front side of the crystal is plane and anti-reflectively coated. In combination with a meniscus with a reflectivity of 97.5 % at 775 nm and 85 % at 1550 nm that is placed in front of the plane side, the cavity is formed. However, the remaining experimental challenge is to achieve simultaneous phase matching and double resonance. This is problematic, since the Gouy phase of focused Gaussian laser beams [Las07] and dielectric mirror coatings introduce differential phase shifts. Apart from that, phase shifts are introduced since the crystal length is not an integer multiple of the coherent builtup length L_{coh}. The reason for this is that the poling period cannot be closely monitored during polishing and cutting of the crystals. To compensate for these differential phase shifts, an adjustable dispersive component like a rotatable, anti-reflectively coated window can be integrated into the cavity [Ste11, Pea99, McK06]. Another alternative is to use a wedged crystal that can be translated perpendicular to the cavity axis, which changes the differential optical path length for both fields in the medium [Ime98, Ste11]. Both approaches have disadvantages. An additional anti-reflectively coated window increases the intra-cavity losses and thus reduces the squeezing that can be observed. Moving a wedged crystal is not possible if one side of the crystal is used as the cavity end-mirror, as in our setup. To solve these issues, a new approach was tested within this thesis. It comprises the partitioning of the nonlinear, quasi phase matched crystal into two different regions that can be heated independently to different temperatures. Thus, the main part of the crystal can be heated to the phase matching temperature while the remainder can be used to fine tune the cavity length via the thermal expansion of the material and thus compensate for the differential phase shifts mentioned above. For that purpose, the heating unit that contains the crystal was redesigned. This section describes the design of the cavity and the heating unit in detail. Apart from that, the effect of the temperature gradient on second-harmonic generation is presented. Both cavities for second-harmonic generation and parametric down-conversion use the same mechanical design.

3.2.1 Nonlinear-cavity design

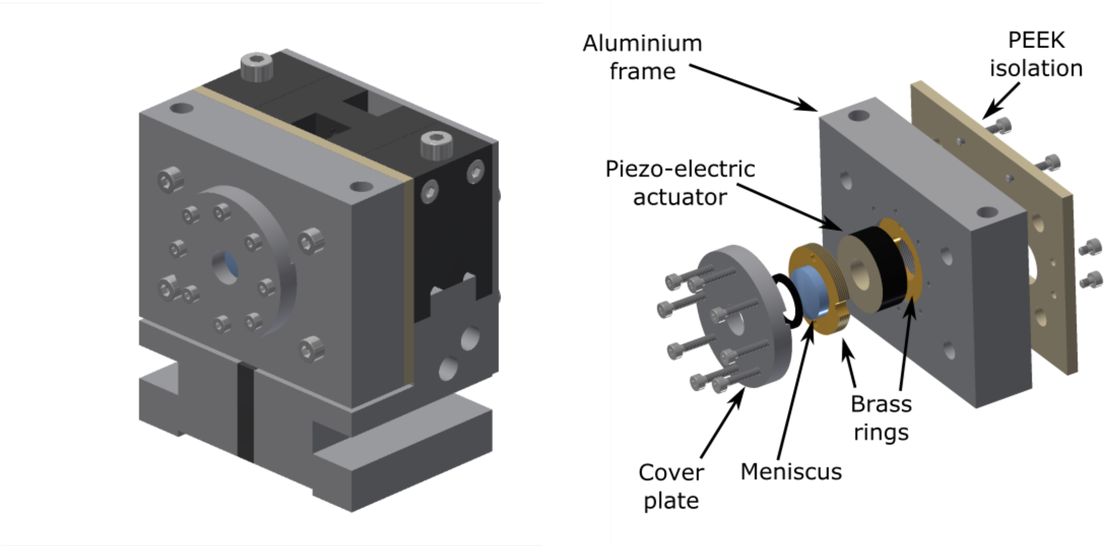

Figure 3.5: Drawing of the nonlinear cavity and the construction that holds the incoupling mirror. The explosion on the right side shows its individual parts. The position of the inner brass rings defines the air gap between the meniscus and the crystal inside the cavity. With the piezo-electric element, the cavity length can be adjusted. The PEEK isolation decouples the frame thermally from the rest of the cavity.

A drawing of the nonlinear cavity is shown in figure 3.5. The left side shows the complete construction, the right side an explosion of the front which contains the meniscus and a piezo-electric element. This element pushes on the meniscus and can thus be used to change and scan the cavity length. To assemble the front, the piezo-electric element is placed on a brass ring first. The circumference of this brass ring is threaded to fit in the threaded hole in the aluminium frame. Its position in the frame defines the cavity length. Before the meniscus is placed on top of the piezo-electric element, a second brass ring is placed in the hole to assist with the alignment of the meniscus. It ensures that the center of the meniscus is aligned with the center of the other parts and the hole in the aluminum plate. The mensicus and piezo-electric element are finally fixed and kept in their position by the tension created by putting the cover plate on top of the meniscus and screwing it down to the aluminium frame. In the experiment, the whole frame can be moved in front of the crystal. Its optimal position is defined by the axis of the cavity that is formed by the meniscus and the curved backside of the nonlinear crystal. This axis must be in parallel to the optical table. To find this position, a laser beam is coupled into the cavity through the meniscus and the power that leaks out of the cavity through its backside is detected with a photodiode. Slightly moving the aluminium frame while scanning the cavity length with the help of the piezo-electric element makes it possible to find a position in which cavity modes are visible on the photodiode. Once this position is found, the frame is attached to the rest of the cavity construction with the four screws in its corners. However, a stable cavity can only be formed if the air gap between the inner surface of the meniscus and the anti reflectively coated plane side of the crystal is chosen appropriately. The air gap also affects the size and the position of the waist of the laser beam inside the cavity. The dependence of both parameters on the air gap is shown in figure 3.6. The radius of curvature of the highly reflective coated backside of the crystal is 12 mm and the power reflectivity is $> 99.98\,\%$ for 1550 nm and $\approx 99.955\,\%$ at 775 nm, according to the manufacturer. The incoupling mirror has a radius of curvature of 25 mm and a power reflectivity of 85.0 % for 1550 nm and 97.5 % for 775 nm. Those values result in a simulated free spectral range of 3.66 GHz. The full-width-half-maximum linewidth at 1550 nm is 95.56 MHz and at 775 nm it is 15.36 MHz. The cavity is stable for an air gap within the range of 20 mm to 26 mm. We

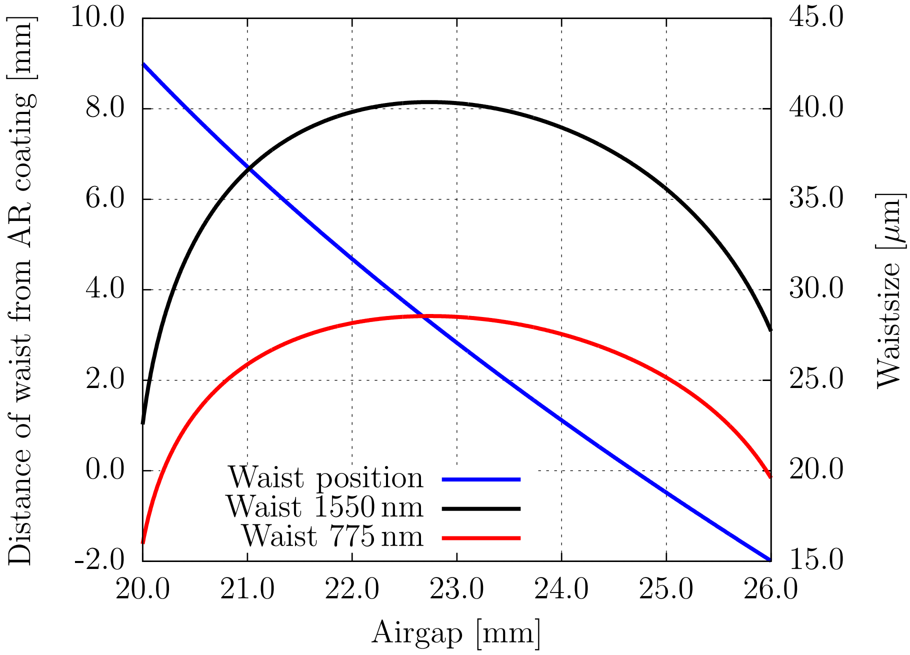

Figure 3.6: Dependence of the waist position and size on the air gap between the incoupling mirror and the plane side of the nonlinear crystal. The cavity is stable for air gaps within the range of 20 mm to 26 mm. The waist position is given as the distance from the plane, anti-reflectively coated surface. Values between 0 and 9.3 mm indicate that the waist is within the crystal. For negative values, the waist is outside the crystal and in front of the plane side.

set the air gap to approximately 24.8 mm for the second-harmonic generation cavity and 24 mm for the parametric down-conversion cavity. In both cases, the waist lies within the first two thirds of the crystal, close to the anti-reflectively coated plane surface. The small waist in the cavity creates a strong electric field that increases the nonlinear coupling, as explained in section 2.2.1. Thus, this region of the crystal should be heated to the phase matching temperature. The last few millimeters of the crystal can then be heated to a slightly different temperature. Since the beam has already diverged, the field strength is smaller in this region, which decreases the nonlinear coupling. The end section of the crystal can thus be used to fine tune the cavity length. Changing the temperature of this section results in small changes of

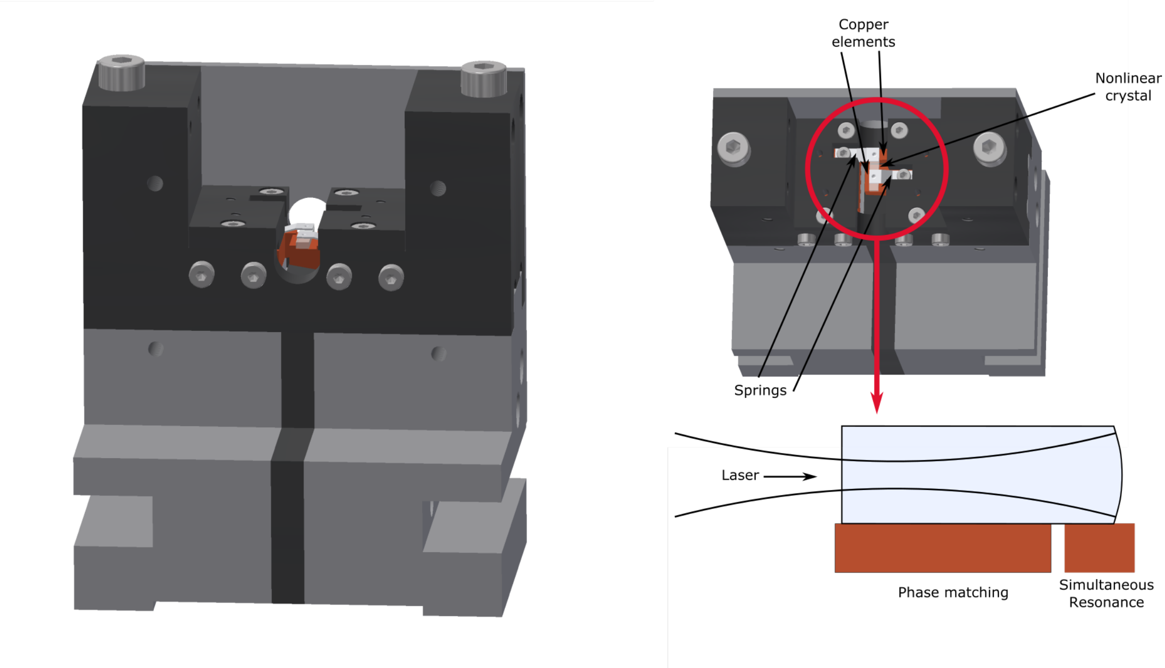

Figure 3.7: Construction of the heating unit within the nonlinear cavities. The left picture shows the cavity without the frame that contains the incoupling mirror. The nonlinear crystal is visible in the center and held onto the copper elements with two springs. The copper guides the heat generated by two peltier elements underneath them into the crystal. As shown in the bottom right picture, the waist of the beam in the cavity is in the first two thirds of the crystal. This area is heated up to the phase matching temperature. The last few millimeters can be heated to a different temperature to adjust the cavity length and improve the simultaneous resonance of both the fundamental and second-harmonic field.

the cavity length as it is increased by further heating and decreased by cooling. This feature can be used to optimize the simultaneous resonance of the second-harmonic and fundamental field, which in turn leads to higher conversion efficiencies due to a better overlap of the cavity modes for the fundamental and second-harmonic wavelengths in the first two thirds of the crystal. The construction that creates the two temperatures within the crystal is depicted in figure 3.7. A photograph is shown in figure 3.8. It shows the nonlinear cavity without the frame that holds the meniscus. The crystal is positioned in the center of the cavity on two copper plates. Two springs keep it in its position with a force of $1.1 \pm 0.4\,\mathrm{N}$. The copper plates conduct the heat, that is generated by two peltier elements underneath the respective plate, into the crystal. To improve the heat transfer from the copper into the crystal, thin gold foil was placed in between them. Gold foil was chosen because it is a soft material with a high thermal conductivity. Thus, it can even out roughnesses from the manufacturing process of the copper elements without lowering the thermal conductivity. In the

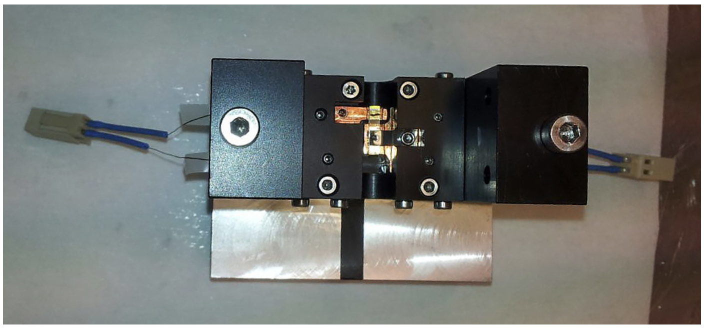

Figure 3.8: Photograph of the nonlinear cavity that was used in this experiment for second-harmonic generation and parametric down-conversion. In the center, the nonlinear crystal that is placed on two copper elements is visible. It is fixed in its position with one of the two springs that were used in total.

experiment, the beam from the linear filter cavity in the laser preparation section was guided into the second-harmonic generation cavity, as figure 3.2 shows. The second-harmonic generation cavity converts the beam from 1550 nm to 775 nm. A characterization of the second-harmonic generation process will be presented in the next section. The converted beam is sent into the parametric down-conversion cavity and serves as the pump field to generate the squeezed field. The length of the second-harmonic generation cavity and parametric down-conversion cavity was stabilized with the piezo-electric element in the aluminium frame. The error signal was generated by the Pound-Drever-Hall method in both cases. For that purpose, an electro-optical modulator was inserted into the experiment and imprinted sidebands at 17.5 MHz on the 1550 nm field that pumps the second-harmonic generation cavity. The bright 1550 nm field as well as the sidebands are converted. The converted sidebands were detected and demodulated in transmission of the nonlinear cavities. The advantage of locking the second-harmonic generation cavity with the 775 nm sidebands is that the lock is more stable. At 1550 nm, the conversion reduces the power in the sidebands and the lock becomes unstable. The parametric down-conversion cavity was locked in the same way with the converted sidebands. The open loop gain measurements of both cavities are shown in figure 3.9. A control loop bandwidth of around 9 kHz was achieved for the nonlinear cavities.

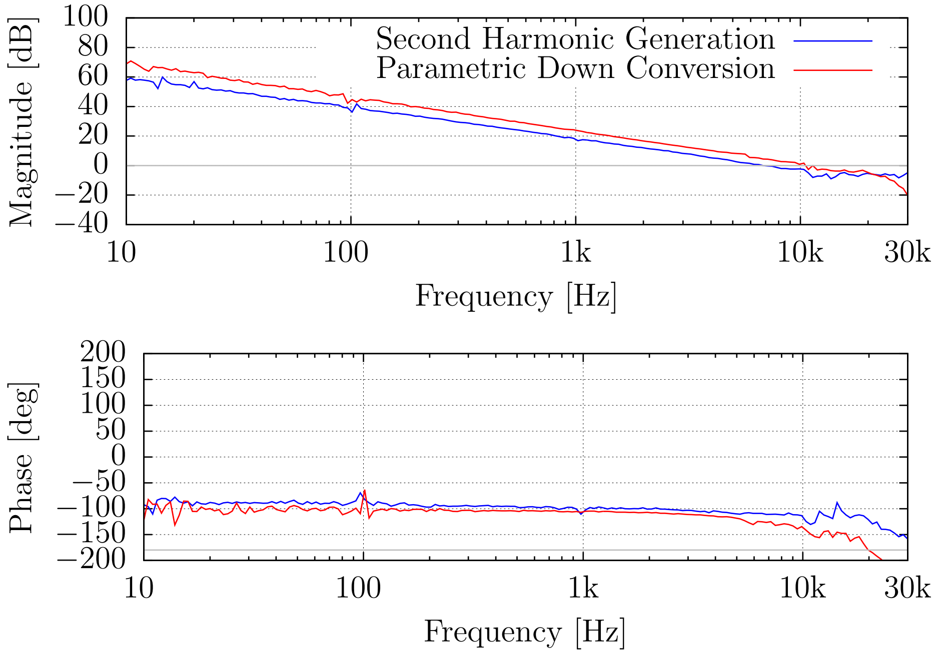

Figure 3.9: Bode plot of the open loop gain of the nonlinear cavities. Both the second-harmonic generation cavity and the parametric down-conversion cavity achieved a control loop bandwidth around 9 kHz. This value is higher than the 2 kHz for the linear filter cavities. In the bode plots for the filter cavities, a peak around 10 kHz is visible, which limits the control loop bandwidth. However 2 kHz were sufficient for the filter cavities since the lock proved to be stable for hours in our experiment.

3.2.2 Second-harmonic generation

The second-harmonic generator used in this experiment was described in detail in the previous section. It converts the laser power at 1550 nm to 775 nm. This field is needed to pump the parametric down-conversion that generates the squeezed vacuum. A high conversion efficiency is desirable for the experiment since it allows for a reduction of the input laser power. To calculate the conversion efficiency, we measured the input power at 1550 nm and the generated output at 775 nm with a powermeter. The conversion efficiency is given by

$$\eta_{\mathrm{conv}} = \frac{P_{775}}{P_{1550}}. \tag{3.1}$$

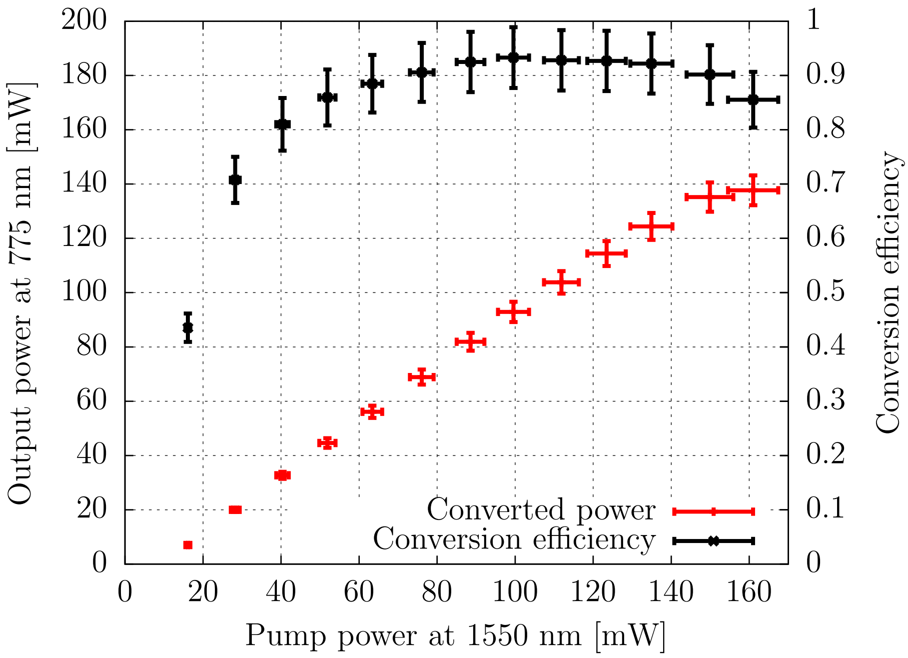

Figure 3.10: Conversion efficiency of second-harmonic generation. We achieved a conversion efficiency of more than 90 %. The values presented were not corrected for any inefficiencies, which means that the input pump power at 1550 nm was not corrected for the mode matching to the fundamental mode of the second-harmonic generation cavity. Apart from that, the power in the 775 nm field was directly measured behind the dichroic beam splitter shown in figure 3.2. The powermeter had an error of 4 % for both wavelengths.

The result of our measurement is shown in figure 3.10. We achieved a conversion efficiency of more than 90 %. The input pump power was not corrected for the mode matching of the pump field to the fundamental mode of the second-harmonic generation cavity. Thus, the conversion efficiency takes the total external power and all inefficiencies into account. For smaller input powers, the conversion efficiency decreases. The reason is the smaller intra cavity power which reduces the nonlinear coupling. For higher pump powers, the efficiency decreases as well. In this regime, the high input power at 1550 nm leads to a strong nonlinear coupling and thus a strong field at 775 nm. The intra cavity power of this field at 775 nm is high enough to initiate the inverse process, that is to say a parametric down converversion from 775 nm back to 1550 nm in the same cavity. To suppress this effect, temperature fine tuning was used to reduce the gain for the conversion to 1550 nm.

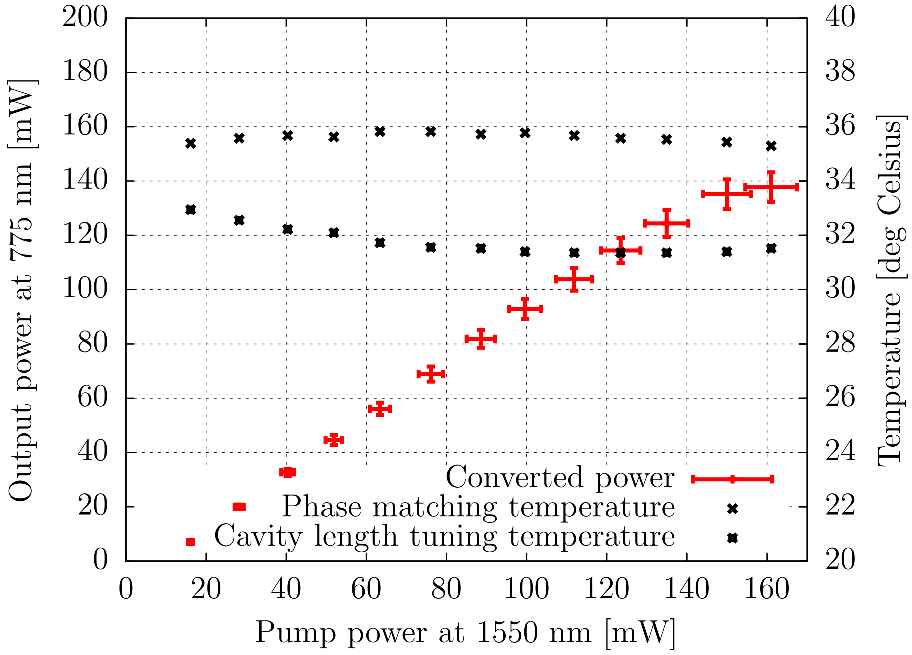

Figure 3.11: Temperature settings that were used to optimize the conversion efficiency of the SHG. For each input power at 1550 nm, both temperature actuators were tuned. The phase matching temperature does not vary significantly with the input power, but to suppress the conversion from 775 nm back to 1550 nm, the cavity length was changed for higher pump powers to reduce the gain for that back-conversion process. The data were not corrected for inefficiencies. The temperatures were deduced from measurements with NTC sensors that were placed in the copper elements of the heating unit.

Figure 3.11 shows the temperature settings that were necessary to achieve optimal phase matching and the best resonance condition for both fields at 1550 nm and 775 nm. The procedure to optimize the temperatures was as follows: First, we scanned the cavity length and observed the transmitted 775 nm field on a photodiode. We tuned both temperatures to maximize the power in the fundamental mode of the second-harmonic field. Once the best combination was found, the cavity length was stabilized. While being stabilized, we optimized the temperatures again for maximum output at 775 nm. After that procedure, we took the data presented in figure 3.11. We observed that the temperature that adjusts the cavity length varies with the input pump power, while the phase matching temperature varies only very little by a few tenth of a degree Celsius. As described above, conversion from 775 nm back to a 1550 nm mode of the second-harmonic generation cavity can set in for large 775 nm intra-cavity powers. If the gain for that process is high enough, an optical parametric oscillation can be initiated, as illustrated in figure 3.12.

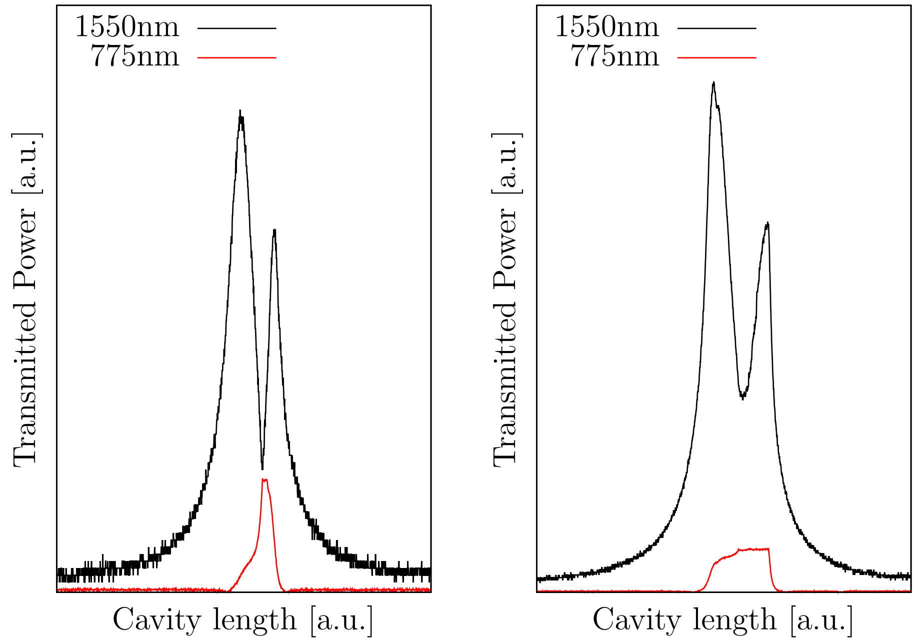

Figure 3.12: Conversion from 775 nm back to 1550 nm in the second-harmonic generation cavity due to an optical parametric oscillation initiated by high intra-cavity powers at 775 nm. On the left hand side, the 775 nm peak is slightly flattened, indicating that the 775 nm intra-cavity power is high enough to initiate the inverse process, a conversion from 775 nm back to 1550 nm. On the right hand side, the 775 nm peak is cutoff. Due to the high intra-cavity power, an optical parametric oscillation takes place and converts the light back to 1550 nm.

The picture on the left shows the 775 nm cavity peak in red and the 1550 nm peak in black. The top of the peak at 775 nm is slightly flattened, indicating that the intra-cavity power at 775 nm at these points is high enough to initiate an optical parametric oscillation that is converting power from 775 nm back to 1550 nm. On the right hand side, the 775 nm intra cavity power is above the oscillation threshold. The 775 nm peak is cutoff and a plateau is observable, since the power that exceeds the oscillation threshold is converted to 1550 nm. By slightly changing the cavity length and thus the overlap of the 775 nm and 1550 nm cavity mode, that effect can be suppressed because the gain for the oscillation is reduced. Thus, no conversion back to 1550 nm takes places. However, this procedure reduces the conversion efficiency to less than 90 %

due to the non-perfect mode overlap of both cavity modes. While the experiments that are described in this thesis were performed, another multi-temperature scheme for second-harmonic generation was published in [Zie17]. In contrast to our setup, their scheme uses three temperature regions instead of two and a partially periodically poled material with curved and coated end surfaces that form a monolithic resonator. In addition to the temperatures, a piezo-electric element, that applies pressure to the crystal, is used to adjust and stabilize the cavity length. With this scheme, it was also possible to achieve simultaneous phase matching and double resonance for second-harmonic generation.

3.3 Theory of balanced homodyne detection

Balanced homodyne detection is used to characterize squeezed vacuum states. Squeezed states of light are characterized by comparing the noise power in the squeezed and anti-squeezed quadrature with vacuum noise. A reference beam, the local oscillator, is needed to discriminate between those two quadratures ([Bac04], pp. 206ff.). This reference beam is overlapped with the squeezed field on a beam splitter, where they interfere with each other. Each of the resulting fields in the two output ports is detected with a photo diode. Figure 3.13 shows this detection scheme.

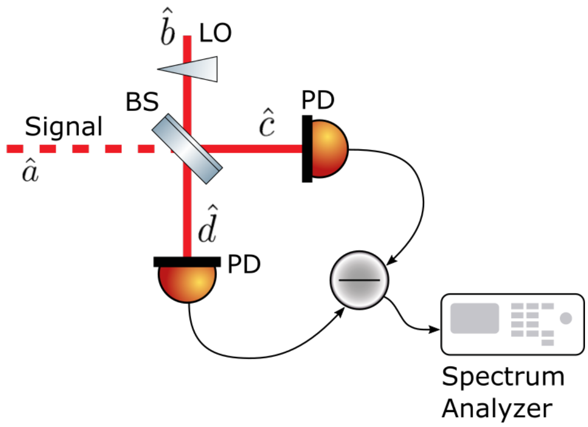

Figure 3.13: Homodyne detection scheme. The signal field is overlapped with a local oscillator (LO) at a beam splitter (BS). The fields at the outputs are each detected with a photo diode and the resulting photo currents are subtracted. The signal that is obtained from the subtraction is recorded with a spectrum analyzer.

The photocurrent of each diode is proportional to the detected intensity and given by $I_c = \langle \hat{c}^\dagger \hat{c} \rangle$ and $I_d = \langle \hat{d}^\dagger \hat{d} \rangle$ ([Ger05], pp. 167ff.). The modes after passing the beam splitter are given by ([Scu97], pp. 125ff.)

$$\hat{c} = \sqrt{T}\hat{a} + \mathrm{i}\sqrt{1-T}\hat{b} \tag{3.2}$$

$$\hat{d} = \mathrm{i}\sqrt{1-T}\hat{a} + \sqrt{T}\hat{b}, \tag{3.3}$$

with the transmissivity T of the beam splitter that is shown in the detection scheme. With this definition, we get

$$\begin{aligned}
\hat{c}^\dagger \hat{c} &= \left(\sqrt{T}\hat{a}^\dagger - \mathrm{i}\sqrt{1-T}\hat{b}^\dagger\right)\left(\sqrt{T}\hat{a} + \mathrm{i}\sqrt{1-T}\hat{b}\right) \\
&= T\hat{a}^\dagger \hat{a} + (1-T)\,\hat{b}^\dagger \hat{b} + \mathrm{i}\sqrt{T\,(1-T)}\left(\hat{a}^\dagger \hat{b} - \hat{b}^\dagger \hat{a}\right) \qquad (3.4)
\end{aligned}$$

$$\begin{aligned}
\hat{d}^\dagger \hat{d} &= \left(-\mathrm{i}\sqrt{1-T}\hat{a}^\dagger + \sqrt{T}\hat{b}^\dagger\right)\left(\mathrm{i}\sqrt{1-T}\hat{a} + \sqrt{T}\hat{b}\right) \\
&= (1-T)\,\hat{a}^\dagger \hat{a} + T\hat{b}^\dagger \hat{b} - \mathrm{i}\sqrt{T\,(1-T)}\left(\hat{a}^\dagger \hat{b} - \hat{b}^\dagger \hat{a}\right) \qquad (3.5)
\end{aligned}$$

For $T = 0.5$, which is the case in balanced homodyne detection, we get:

$$\hat{c}^\dagger \hat{c} = \frac{1}{2}\hat{a}^\dagger \hat{a} + \frac{1}{2}\hat{b}^\dagger \hat{b} + \mathrm{i}\frac{1}{2}\left(\hat{a}^\dagger \hat{b} - \hat{b}^\dagger \hat{a}\right) \qquad (3.6)$$

$$\hat{d}^\dagger \hat{d} = \frac{1}{2}\hat{a}^\dagger \hat{a} + \frac{1}{2}\hat{b}^\dagger \hat{b} - \mathrm{i}\frac{1}{2}\left(\hat{a}^\dagger \hat{b} - \hat{b}^\dagger \hat{a}\right). \qquad (3.7)$$

If we take the difference of the detected intensities and calculate the mean, the advantage of balanced homodyne detection becomes apparent:

$$\begin{aligned}
I_c - I_d =& \left\langle \hat{c}^\dagger \hat{c} - \hat{d}^\dagger \hat{d} \right\rangle \\
=& \Big\langle \frac{1}{2}\hat{a}^\dagger \hat{a} + \frac{1}{2}\hat{b}^\dagger \hat{b} + \mathrm{i}\frac{1}{2}\left(\hat{a}^\dagger \hat{b} - \hat{b}^\dagger \hat{a}\right) \\
& - \frac{1}{2}\hat{a}^\dagger \hat{a} - \frac{1}{2}\hat{b}^\dagger \hat{b} + \mathrm{i}\frac{1}{2}\left(\hat{a}^\dagger \hat{b} - \hat{b}^\dagger \hat{a}\right) \Big\rangle \\
=& \mathrm{i}\left\langle \hat{a}^\dagger \hat{b} - \hat{b}^\dagger \hat{a} \right\rangle. \qquad (3.8)
\end{aligned}$$

Since the terms proportional to $\hat{a}^\dagger \hat{a}$ and $\hat{b}^\dagger \hat{b}$ have the same sign, they vanish in the photocurrent that results from the subtraction. Only the interference terms $\hat{a}^\dagger \hat{b}$ and $\hat{b}^\dagger \hat{a}$ remain ([Scu97], p. 128). Thus, for $T = 0.5$, technical noise in the input modes $\hat{a}$ and $\hat{b}$ cancels out ([Leo97], pp. 83ff.). In a squeezing experiment, the local oscillator can be described as a coherent state. Thus, we can write $\hat{b} = \beta \mathrm{e}^{-\mathrm{i}\nu t}$ with $\beta = |\beta|\mathrm{e}^{\mathrm{i}\psi}$ and get

$$\begin{aligned}
I_c - I_d &= \mathrm{i}\left\langle \hat{a}^\dagger \hat{b} - \hat{b}^\dagger \hat{a} \right\rangle \\
&= \mathrm{e}^{\mathrm{i}\frac{\pi}{2}} \langle \hat{a}^\dagger |\beta| \mathrm{e}^{\mathrm{i}\psi} \mathrm{e}^{-\mathrm{i}\nu t} - \hat{a}|\beta|\mathrm{e}^{-\mathrm{i}\psi}\mathrm{e}^{\mathrm{i}\nu t} \rangle \\
&= \langle \hat{a}^\dagger |\beta| \mathrm{e}^{\mathrm{i}\left(\psi + \frac{\pi}{2}\right)} \mathrm{e}^{-\mathrm{i}\nu t} + \hat{a}|\beta|\mathrm{e}^{-\mathrm{i}\left(\psi + \frac{\pi}{2}\right)}\mathrm{e}^{\mathrm{i}\nu t} \rangle \\
&= |\beta| \left\langle \hat{a}^\dagger \mathrm{e}^{-\mathrm{i}\nu t} \mathrm{e}^{\mathrm{i}\Theta} + \hat{a}\mathrm{e}^{-\mathrm{i}\Theta}\mathrm{e}^{\mathrm{i}\nu t} \right\rangle \qquad (3.9)
\end{aligned}$$

with $\Theta = \psi + \frac{\pi}{2}$. Both the local oscillator and the squeezed field have the same frequency ν since they originate from the same laser and we can write $\hat{a} = \hat{a}_0 \mathrm{e}^{-\mathrm{i}\nu t}$. With this relation, we get

$$I_c - I_d = |\beta| \left\langle \hat{a}_0^\dagger \mathrm{e}^{\mathrm{i}\Theta} + \hat{a}_0 \mathrm{e}^{-\mathrm{i}\Theta} \right\rangle \qquad (3.10)$$

A generalized quadrature operator can be defined by $\hat{X}(\Theta) = \hat{a}_0^\dagger \mathrm{e}^{\mathrm{i}\Theta} + \hat{a}_0 \mathrm{e}^{-\mathrm{i}\Theta}$, which corresponds to the cavity output operators as defined in equation (2.94) and (2.95) for $\Theta = 0$ and $\Theta = \frac{\pi}{2}$. Thus, the difference current of a balanced homodyne detector can directly be used to measure the variances of any arbitrary quadrature $\hat{X}(\Theta)$. The measurement signal is amplified and scales with the amplitude of the local oscillator $|\beta|$. In the experiment, the current is converted to a voltage with a transimpedance amplifier. This voltage is analyzed with a spectrum analyzer. The resulting noise power is proportional to the variance of the squeezed state ([Sch17], p. 7).
For the detection scheme, a good spatial overlap of the local oscillator and signal on the balanced beam splitter is important for the interference of both modes. To simplify the alignment, a diagnostic cavity as shown in figure 3.2 is used. Both the local oscillator and signal fields are modematched to this cavity. Since the beam splitter is a common point in both beam paths, a good modematching to the cavity results in a good spatial overlap. The detection efficiency of a balanced homodyne detector depends on this spatial overlap and the quantum efficiency η_{PD} of its diodes. The spatial overlap is characterized by the fringe visibility. If the powers in the input ports are equal, it is given by ([Ste13b], p. 39):

$$V = \frac{I_{\max} - I_{\min}}{I_{\max} + I_{\min}}. \tag{3.11}$$

$I_{\max}$ and $I_{\min}$ are the maximum and minimum intensities that are measured on one of the two photo diodes with scanned local oscillator phase. Including the quantum efficiency of the diodes, the overall detection efficiency of a balanced homodyne detector is given by ([Bac04], p. 210, [Wad16], p. 149)

$$\eta_{\mathrm{det}} = \eta_{\mathrm{PD}} V^2. \tag{3.12}$$

3.4 Coherent control locking for low frequency squeezing

For the detection and application of squeezed vacuum states at audio frequencies, for example in gravitational wave detection [The11], it is necessary to stabilize the squeeze angle as well as the homodyne readout angle. For that purpose, the coherent control scheme was developed and successfully tested in the gravitational wave detector GEO600 [Gro13, Kha12]. The detailed description of this locking technique is presented in ([Che07b], [Che07a], pp. 161 ff.,[Vah08a], pp. 71 ff.) and will be reproduced briefly here. The locking scheme and its integration into the setup is illustrated with phasor diagrams in figure 3.15. To stabilize and actively control the squeezing angle as well as the homodyne readout angle with respect to each other, an interaction that establishes a phase relationship between those quantities is required. This relationship is established with a single sideband that interacts with the nonlinear crystal in the parametric down-conversion cavity. The single sideband is generated in the orange section of figure 3.2. A fraction of the power from the fibre laser is sent towards an acousto-optic modulator that is driven with a 40 MHz modulation and thus creates a sideband at 40 MHz. This first-order sideband leaves the acousto-optic modulator under a different angle than the zero order fundamental beam. Both beams are separated from each other with a pinhole. The frequency-shifted sideband is redirected towards the acousto-optic modulator and passes it once more. This results in a total frequency shift of 80 MHz. The 40 MHz sideband that remains after the second passage through the acousto-optic modulator is separated from the 80 MHz sideband with another pinhole. Since a quarter waveplate is also passed twice, the polarisation of the 80 MHz sideband is turned from the original s-polarisation of the fundamental beam to p-pol. This allows for the separation of the 80 MHz sideband from the fundamental beam that comes from the laser. Subsequently, the single sideband is filtered with a cavity as described in section 3.1. Thus, remaining photons at the fundamental laser frequency are suppressed since their frequency is larger than the cavity linewidth of 1 MHz. In the downstream experiment, the filtered single sideband is injected into the parametric down-conversion cavity through the highly reflective backside. It initiates a parametric down-conversion process, as illustrated in figure 3.14 and a second sideband at −80 MHz is generated due to the nonlinear interaction in the cavity.

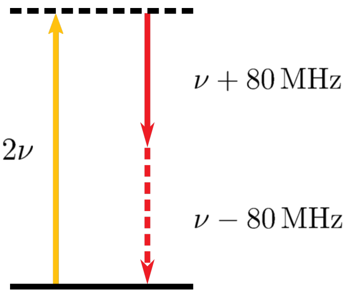

Figure 3.14: Energy level diagram of the interaction of the single sideband at 80 MHz with the nonlinear medium in the parametric down-conversion cavity. The sideband seeds a down-conversion process. Due to energy conservation, a second sideband at −80 MHz has to be created from that processes. The sidebands at +80 MHz and −80 MHz are used to generate the error signal for the coherent control scheme.

The field leaving the cavity after the interaction is proportional to

$$E_{\mathrm{out}}(t) \propto \frac{1+g}{\sqrt{2g}}\alpha_\Omega \cos(\nu t + \Omega t) - \frac{1-g}{\sqrt{2g}}\alpha_\Omega \cos(\nu t - \Omega t - 2\phi) \tag{3.13}$$

with $g = e^{2r}$ and r being the squeeze factor as described earlier. ϕ is the squeezing angle, which is related to the 775 nm pump phase and α_Ω the amplitude of the single sideband that is generated by the acousto-optic modulator. This field is detected behind a $R = 92\,\%$ mirror with a photo diode, resulting in a photocurrent that is proportional to the intensity given by

$$I_{\mathrm{out}}(t) = |E_{\mathrm{out}}|^2 \propto \frac{\alpha_\Omega^2}{2g}\left[(1+g)\cos(\nu t + \Omega t) - (1-g)\cos(\nu t - \Omega t - 2\phi)\right]^2 \tag{3.14}$$

This intensity is modulated with the beating of the two sidebands. Both sidebands are separated by 80 MHz from the carrier. Thus, a demodulation frequency of $2\Omega = 160$ MHz has to be chosen. With the proper demodulation phase and low pass filtering, an error signal that is proportional to the pump phase can be obtained and the pump phase can be stabililzed:

$$\epsilon_{\mathrm{pumpphase}} \propto \frac{\alpha_\Omega^2 \left(g^2-1\right) \sin\left(2\phi\right)}{4g}. \tag{3.15}$$

The error signal for the homodyne detector readout angle is derived from the beating of the local oscillator with the sidebands that leave the parametric down-conversion cavity along the path of the squeezed vacuum. The homodyne detector consists of two photo diodes. The field on the diodes is given by

$$\begin{aligned} E_{\mathrm{PD1}} \propto & \frac{1}{\sqrt{2}}\left[\alpha_{\mathrm{LO}} \mathrm{e}^{-\mathrm{i}(\nu t+\Theta)} + \left(\frac{1+g}{\sqrt{2g}}\alpha_\Omega \cos\left(\nu t+\Omega t\right)\right.\right. \\ & \left.\left. - \frac{1-g}{\sqrt{2g}}\alpha_\Omega \cos\left(\nu t-\Omega t-2\phi\right)\right)\right] + c.c. \end{aligned} \tag{3.16}$$

and

$$\begin{aligned} E_{\mathrm{PD2}} \propto & \frac{1}{\sqrt{2}}\left[\alpha_{\mathrm{LO}} \mathrm{e}^{-\mathrm{i}(\nu t+\Theta)} - \left(\frac{1+g}{\sqrt{2g}}\alpha_\Omega \cos\left(\nu t+\Omega t\right)\right.\right. \\ & \left.\left. - \frac{1-g}{\sqrt{2g}}\alpha_\Omega \cos\left(\nu t-\Omega t-2\phi\right)\right)\right] + c.c.. \end{aligned} \tag{3.17}$$

Here Θ defines the readout angle and determines which quadrature of the signal field is analyzed. The photocurrents that are generated from these fields are subtracted from each other in the homodyne detector. The resulting current is proportional to

$$I_{\mathrm{diff}} = \frac{2\sqrt{2}\alpha_{\mathrm{LO}}\alpha_\Omega \left(-1+g\right)}{\sqrt{g}} \cos\left(\Omega t+2\phi+\Theta\right). \tag{3.18}$$

Demodulation of this current with Ω results in the error signal for the local oscillator readout phase:

$$\epsilon_{\mathrm{homodyne}} = \frac{\sqrt{2}\alpha_{\mathrm{LO}}\alpha_\Omega \left(-1+g\right)}{\sqrt{g}} \sin\left(2\phi+\Theta\right). \tag{3.19}$$

This error signal does not only contain the homodyne readout angle Θ, but also the pump phase ϕ. However, the pump phase can be stabilized with the error signal that has been derived before. With ϕ being constant, a stable phase relationship between the squeezing and readout angle can be established, allowing for the detection of squeezing at acoustic frequencies.

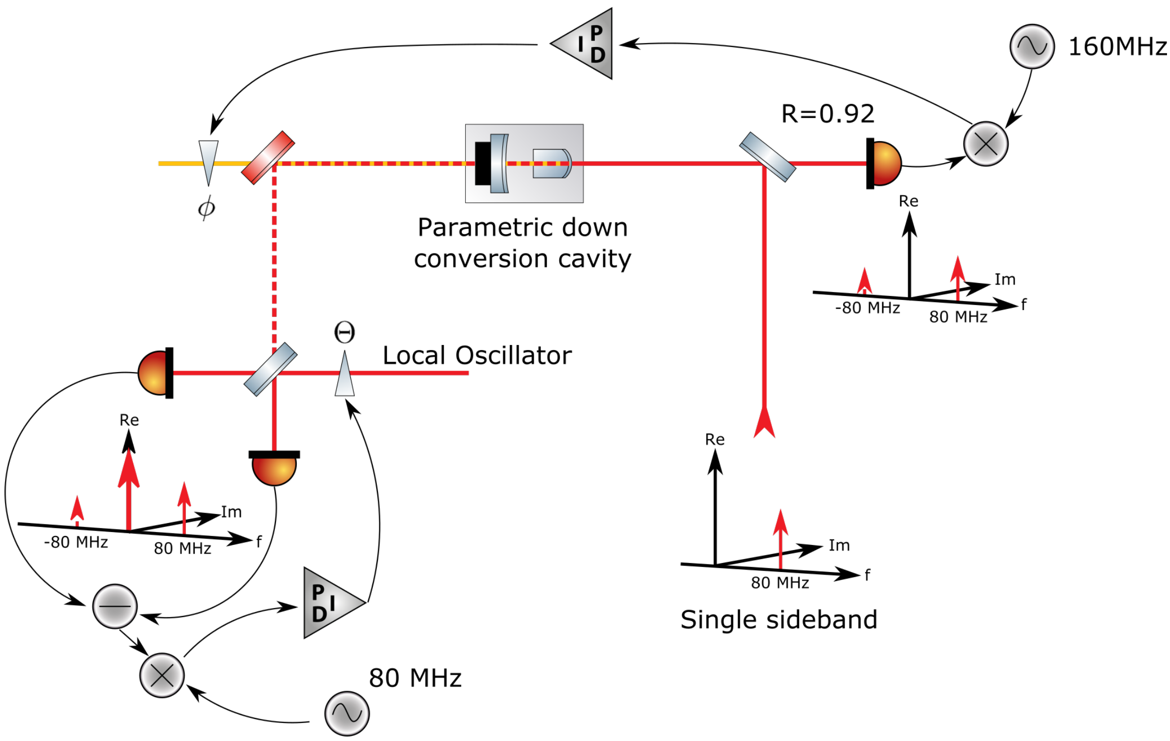

Figure 3.15: Illustration of the generation and propagation of the sidebands needed for the coherent control locking scheme. The single sideband is generated with an acousto-optic modulator and injected into the parametric down-conversion cavity through its highly reflective backside. Within the cavity, a second sideband is generated that leaves the cavity through the backside as well as the incoupling mirror. The signal leaving the backside of the cavity is detected with a single photo diode behind a mirror with a reflectivity of 92 % while the fields that leave the cavity through the incoupling mirror beat with the local oscillator and are detected with the homodyne detector.

As described before, the single sideband is injected through the highly reflectively coated backside of the nonlinear crystal into the parametric down-conversion cavity. Here, a second sideband is created and leaves the cavity through the backside. Both sidebands are detected with a photo diode behind a mirror with a reflectivity of 92 %. Demodulation of the photo current extracts the error signal described by equation (3.15). The two sidebands also escape from the cavity through the incoupling mirror. They follow the path of the squeezed field, beat with the local oscillator and the resulting signal is detected with the photo diodes of the homodyne detector. Demodulation of the difference of the photo currents from each diode yields the error signal given by equation (3.19). The error signals that were generated in the experiment are depicted in figure 3.16. The top picture shows the error signal for the local oscillator phase and the bottom one the error signal that was generated for the pump phase lock. This signal is measured behind a mirror with a reflectivity of 92 %. For that reason and because the sideband at $-80\,\mathrm{MHz}$ escapes the parametric down-conversion cavity through the highly reflective coated backside, the signal to noise ratio is reduced compared to the signal from the homodyne detector in the top picture.

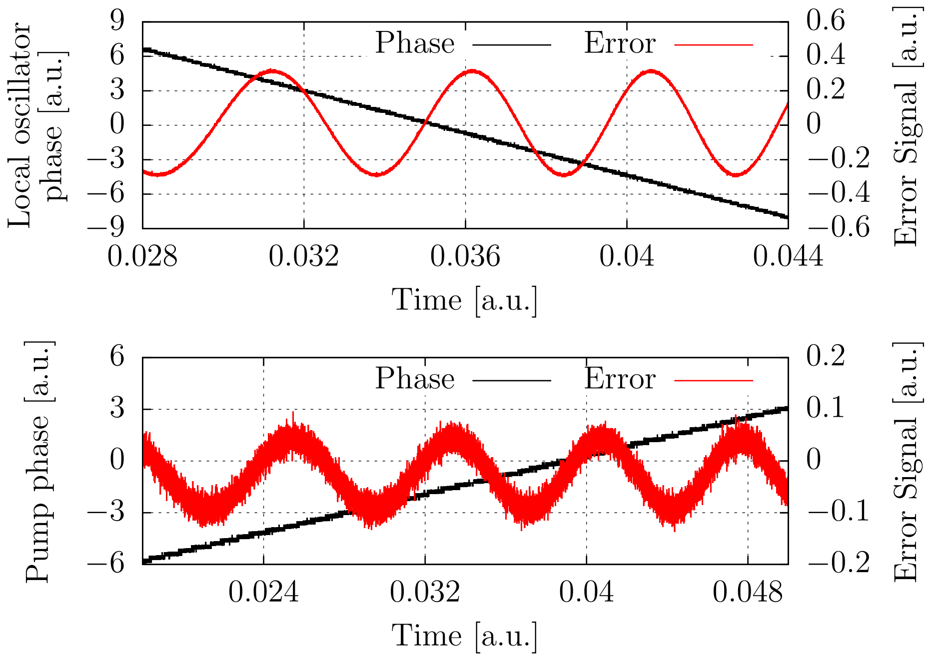

Figure 3.16: Error signals for low frequency locking. The upper plot shows the signal that is generated by demodulation of the homodyne signal with $80\,\mathrm{MHz}$. This signal is used to stabilize the local oscillator phase. The one in the bottom picture results from a demodulation with $160\,\mathrm{MHz}$ and is detected behind the parametric down-conversion cavity, that is to say in reflection of the highly reflective coated backside. It is used to stabilize the pump phase.

Figure 3.17 shows the bode plot of the open loop gain functions for the coherent control scheme as implemented in this experiment. The unity gain frequency is around $70\,\mathrm{Hz}$. Since the phase margin of the lock is very small around those frequencies, the gain was reduced and thus the locking bandwidth to a point where the measurements could be performed when data were taken.

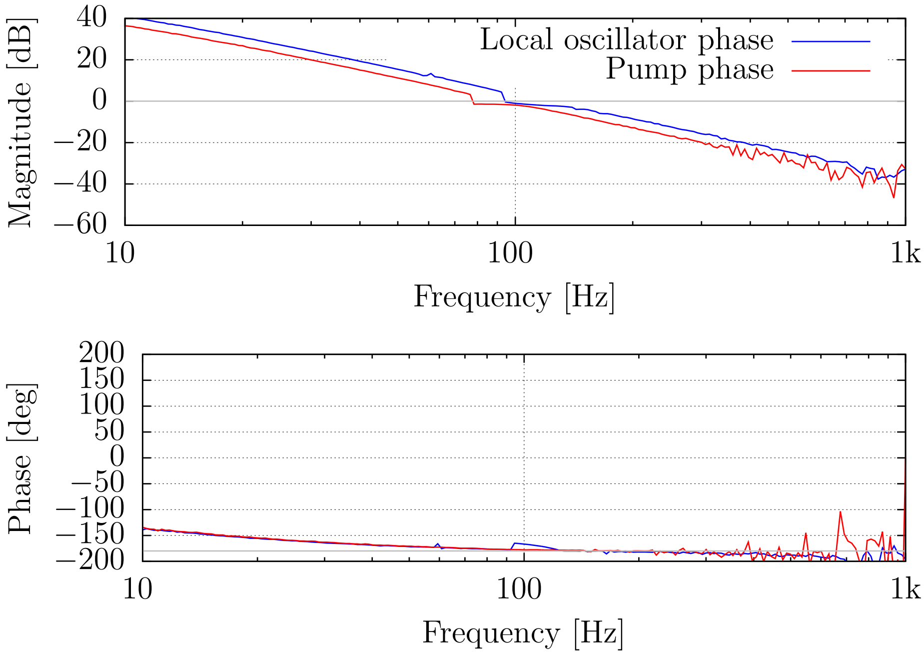

Figure 3.17: Bode plot of the open Loop gain of the coherent control locks. For the unity gain frequency around 70 Hz, the phase margin is small. Thus, the gain was reduced for the measurements to obtain a more stable lock.

4 Squeezing in the MHz regime

Squeezed vacuum states of light with high squeeze factors at MHz or even GHz sideband frequencies are an important resource for applications like quantum key distribution [Ast12] [Ast13] [Ebe13]. In this chapter, we present the detection of 13 dB squeezing at a sideband frequency of 5 MHz and below. The results have been published in [Sch18].

4.1 Detection of 13dB squeezed vacuum states

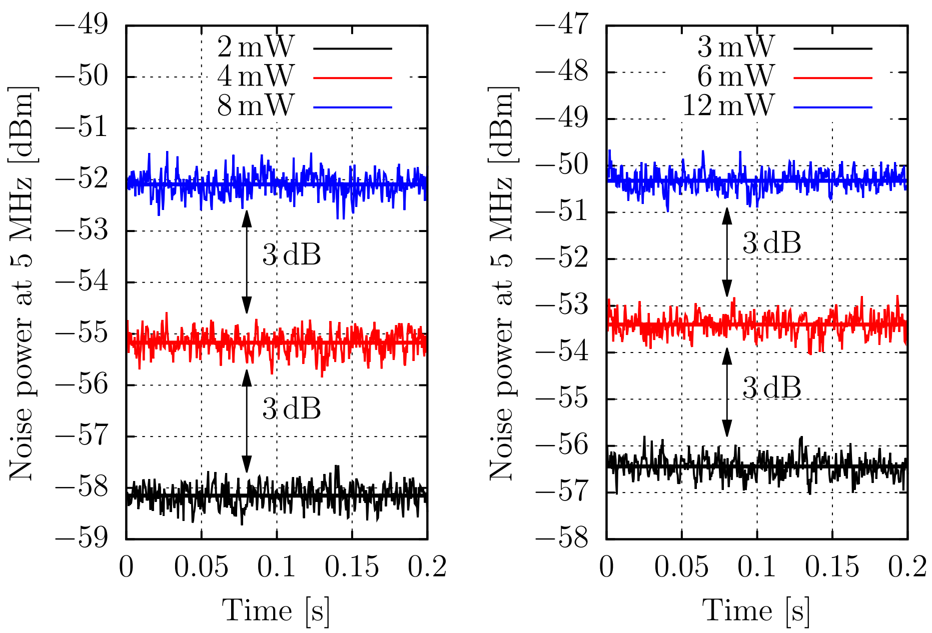

Figure 4.1: Verification of the linearity of the homodyne detector at a sideband frequency of 5 MHz. Vacuum noise was measured with local oscillator powers from 2 mW to 12 mW. Doubling the power results in a 3 dB increase of the noise power, indicating the linearity of the detection system.

For the detection of squeezed vacuum states with strong squeeze factors, a balanced homodyne detector with a large dark noise clearance and a linear response is needed. According to equation (3.10), doubling the local oscillator power P_{LO} increases the amplification of the signal by a factor of two. This results in an increase of $10 \log (2P_{\mathrm{LO}}) =$

$10\log(P_{\mathrm{LO}}) + 3\,\mathrm{dB}$ in noise power if the vacuum noise level is measured. Our detector exhibits this linear scaling for local oscillator powers of up to 12 mW, which is shown in figure 4.1. The resolution bandwidth of the spectrum analyzer for all traces was 300 kHz and the video bandwidth 300 Hz. These settings were used for every measurement presented in this chapter. Figure 4.2 shows the best zero span measurement of a squeezd vacuum state in our experiment.

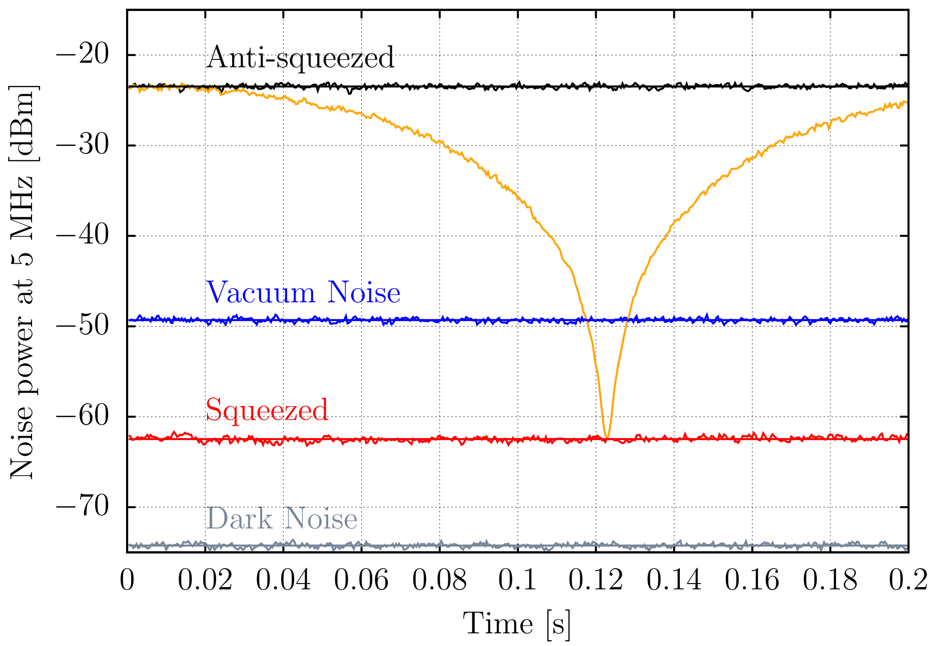

Figure 4.2: Zero span measurement at a Fourier frequency of 5 MHz. The squeeze factor is $13.1 \pm 0.05\,\mathrm{dB}$ and the anti-squeeze factor $25.8 \pm 0.05\,\mathrm{dB}$. The dark noise was 24.9 dB below vacuum noise. The resolution bandwidth was set to 300 kHz and the video bandwidth to 300 Hz.

The quantum noise of the squeezed quadrature is $13.1 \pm 0.05\,\mathrm{dB}$ below the vacuum noise. The noise in the anti-squeezed quadrature is $25.8 \pm 0.05\,\mathrm{dB}$ larger than the shot noise. The difference between the detector's dark noise and the vacuum level was 24.9 dB with a local oscillator power of 12 mW. The dark noise was not subtracted from the data, thus $13.1 \pm 0.05\,\mathrm{dB}$ were directly observed. The orange trace shows a continuous sweep of the local oscillator detection phase from the anti-squeezed to the squeezed quadrature. The vaccuum level was checked before and after each measurement cycle to ensure a constant reference level. The error bars are a result of the remaining uncertainty. To record the traces of the squeezed and anti-squeezed quadrature, the local oscillator phase was manually tuned with the help of a piezo-electric element. The temperature settings were 47.6 °C for the phase matching temperature and 47.0 °C for the temperature that optimizes the cavity length for simultaneous phase matching and double resonance. These values turned out to be ideal to generate the strong squeeze factor. Varying the temperatures around those values led to decreased squeeze factors.

4.2 Spectra and pump power dependence

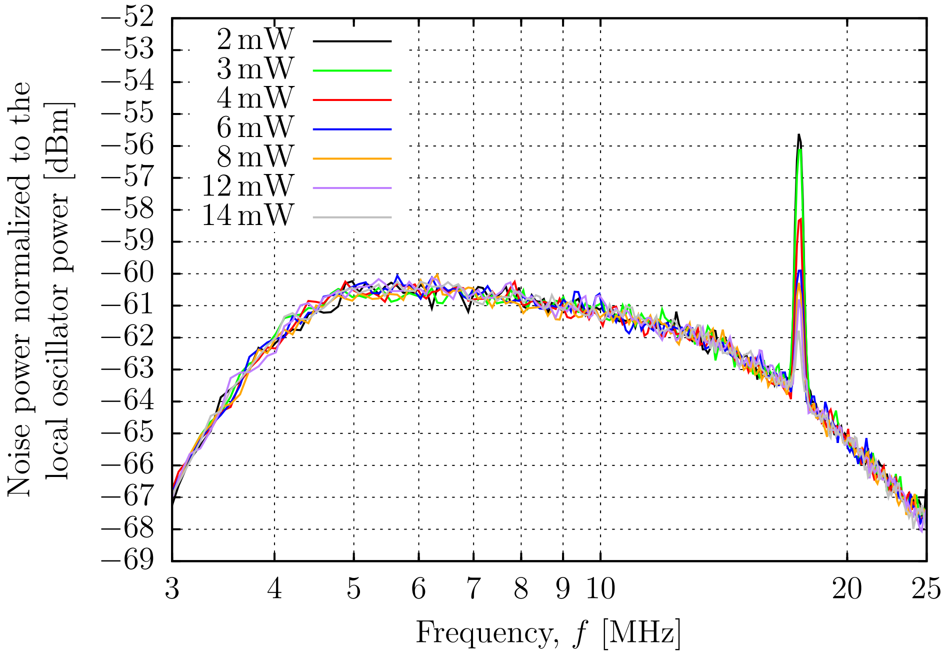

Figure 4.3: Linearity of the homodyne detector between 3 MHz and 25 MHz. Each spectrum of the vacuum noise was normalized to 1 mW local oscillator power. Since the traces overlay, the detector can be considered to be linear between 3 MHz and 25 MHz. At 17.5 MHz, a phase modulation peak that is used for the Pound-Drever-Hall stabilization of the length of the parametric down-conversion cavity, is visible.

At a sideband frequency of 5 MHz, our homodyne detector exhibits the largest amplification of the signal field and the largest darknoise clearance for a given local oscillator power. However, we also characterized the squeezed vaccum source in the frequency range from 3 MHz to 25 MHz. To verify the linearity of the detector in this regime, we measured spectra of vaccum noise for different local oscillator powers from 2 mW to 14 mW. Higher powers were not tested to avoid damage of the photo diodes. All spectra were normalized to 1 mW local oscillator power. For that purpose, the measured noise power was converted to linear units:

$$P_{\text{noise}}\,[\text{mW}] = 10^{\frac{P_{\text{noise}}[\text{dBm}]}{10}}\,[\text{mW}]\,,$$

normalized to the local oscillator power:

$$\frac{P_{\text{noise}}}{P_{\text{LO}}} = \frac{10^{\frac{P_{\text{noise}}[\text{dBm}]}{10}}}{P_{\text{LO}}},$$

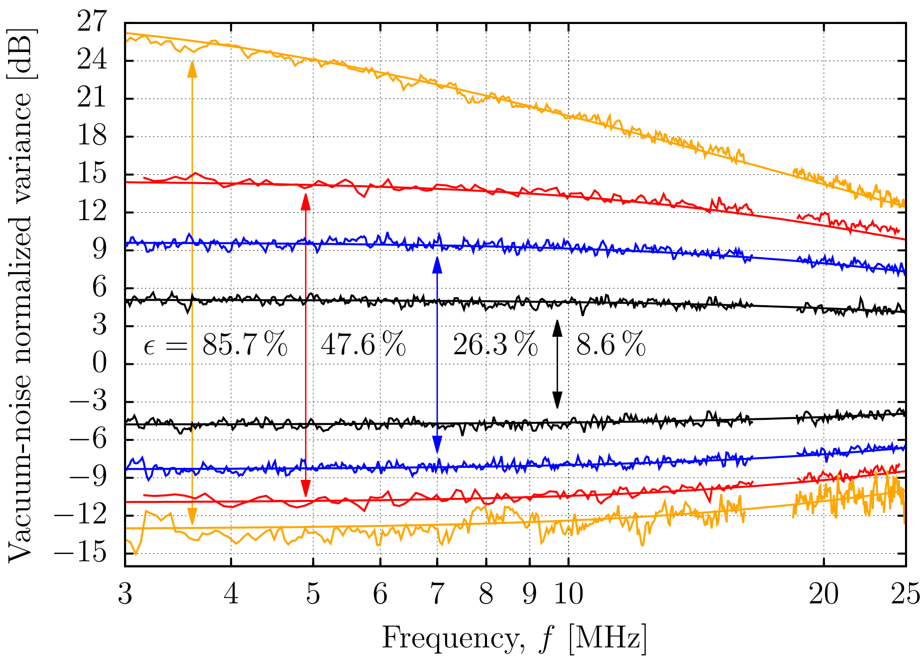

Figure 4.4: Spectra showing the dependence of the squeeze and anti-squeeze factors on the pump parameter. To allow for a comparison with the theory, each spectrum was corrected from dark noise. The pump parameters were 85.7 %, 47.6 %, 26.3 % and 8.6 %. From the fits, we infered the linewidth of the parametric down-conversion cavity to be 109.8 MHz and the overall detection efficiency to be 0.952. The resolution bandwidth was 300 kHz with a video bandwidth of 300 Hz. For the $\epsilon = 85.7\,\%$ spectrum, we reduced the local oscillator power to 1 mW to ensure that the large anti-squeezed noise powers remain within the linear regime of the homodyne detector.

and converted back to dBm scaling:

$$\begin{aligned}\frac{P_{\text{noise}}}{P_{\text{LO}}}\,[\text{dBm}] &= 10\log\frac{10^{\frac{P_{\text{noise}}}{10}}/P_{\text{LO}}}{1\,[\text{mW}]}\\ &= P_{\text{noise}}\,[\text{dBm}] - 10\log\frac{P_{\text{LO}}\,[\text{mW}]}{1\,\text{mW}}.\end{aligned}$$

Figure 4.3 shows that the traces for the different local oscillator powers overlay with each other, indicating that the normalized noise powers are identical and that the homodyne detector is linear in the given regime. Around 17.5 MHz a modulation peak, resulting from the cavity length stabilization of the parametric down-conversion cavity is visible. The squeezed vaccum state cannot be characterized within that region. Figure 4.4 shows spectra of the squeeze and anti-squeeze factors in the frequency range from 3 MHz to 25 MHz. We fitted formula (2.102) to the data, as the solid lines indicate. The data were corrected from dark noise. Each spectrum was recorded with a different pump power, resulting in different pump parameters ϵ. We measured values of 85.7 %, 47.6 %, 26.3 % and 8.6 %. To extent the linear response of the homodyne detector to the large anti-squeezed noise powers of the data with $\epsilon = 85.7\,\%$, we reduced the local oscillator power to 1 mW for this measurement. This was done at the expense of a lower dark-noise clearance. From fitting, we inferred a full-width at half-maximum linewidth of the parametric down-conversion cavity of $\frac{\gamma}{2\pi} = 109.8\,\mathrm{MHz}$ and an overall detection efficiency of $\eta = 0.952$. Datapoints around 17.5 MHz were deleted from the plot and not included for the fits since they were shifted by the phase modulation peak for the lock that is shown in figure 4.3. The measured linewidth is in good agreement with the simulated value of 95.56 MHz. Most likely, the deviation results from the fact that the optical path length of the cavity cannot be determined and adjusted exactly enough. The air gap between the incoupling mirror and the crystal might be shorter than calculated, resulting in an increased linewidth. Each trace was recorded with a temperature of 47.6 °C for phase matching and 47 °C for the optimization of the simultaneous resonance and phase matching conditions. The independence of the temperature settings from the pump parameter indicates that heating due to absorption of light in the nonlinear crystal is not influencing our measurements. This is in accordance with the results obtained by Steinlechner et al. in [Ste13a] and our second-harmonic generation measurements presented in the previous section. Steinlechner et al. measured an absorption of 84 ± 40 ppm/cm at 1550 nm and 127 ± 24 ppm/cm at 775 nm, which is negligible for small laser powers. Our best squeezing values were obtained with only 12 ± 1 mW external pump power at 775 nm. As figure 3.11 indicates, the adjustment of the cavity length temperature due to absorption induced heating of the crystal is only necessary for significantly higher powers.

4.3 Loss analysis

As figure 2.9 shows, the squeezing and anti-squeezing levels from an ideal lossless parametric down-conversion cavity are identical for all sideband frequencies. However, optical losses in the setup reduce the observable squeeze factor. This is described by equation (2.102) and illustrated in figure 2.10. Our setup was limited by 4.8 % optical loss, as we deduced from the fits to the spectra that resulted in a value of $\eta = 0.952$ for the propagation efficiency. The limited homodyne visibility contributes most to the optical losses. We achieved a fringe visibility of $\approx 99\,\%$, resulting in 2 % detection loss according to equation 3.12. In other experiments, values of up to 99.6 % have been achieved [Vah16]. We assume that a slight deviation of the spatial mode shape of the local oscillator from a perfect TEM00 mode is limiting our fringe visibility. As figure 3.2 shows, the local oscillator is split off from the beam leaving the filter cavity in the laser preparation section with a polarizing beam splitter. The halfwave-plate in front of the beam splitter allows for the adjustment of the local oscillator power. However, imperfections might result in a deformation of the modeshape, limiting the interference contrast of the local oscillator with the signal at the beam splitter of the homodyne detector. Another filter cavity in the local oscillator path, as also shown in [Vah16], might lead to an improved fringe visibility. However, the limited space of 80 x 80 cm^2 did not allow for another component in this section. Another source for optical losses is the quantum efficiency of the photo diodes. We used custom made diodes manufactured by Laser Components. Their quantum efficiency is specified to be $\eta_{\mathrm{pd}} \approx 0.99$. Thus, the diodes contribute 1 % to the total losses. Apart from that, the transmission through seven anti-reflectively coated surfaces of three lenses and the parametric down-conversion cavity coupler lead to $\eta_{\mathrm{pr}} \approx 0.99$ and thus 1 % losses. The remaining 0.8 % losses can be explained by the escape efficiency of the parametric down-conversion cavity, which describes how efficient the squeezed field is extracted from the cavity [Wad16]. It is given by [Meh12]

$$\eta_{\mathrm{esc}} = \frac{T}{T+L}. \tag{4.1}$$

where T is the transmissivity of the input coupler and L represents the intracavity losses. For our cavity, the transmissivity of the input coupler was 15 %. From the measurement protocol of the coating company Laseroptik GmbH, we estimate a value around 0.1 % for the intracavity losses, which includes losses at the anti-reflectively coated plane surface of the crystal and the remaining transmissivity through the highly-reflectively coated curved end face as well as absorption and scattering within the crystal. Thus, we obtain

$$\eta_{\mathrm{esc}} = \frac{15\,\%}{15\,\% + 0.1\,\%} = 0.993. \tag{4.2}$$

The escape efficiency can be improved by reducing the losses or increasing the transmissivity of the input coupling mirror. Reducing the losses is difficult, since the main sources depend on the manufacturing processes of the suppliers or material properties and cannot be controlled. Increasing the transmissivity is possible, however, it would lead to a higher threshold for optical parametric oscillation, which results in a higher pump power that is necessary to achieve the same squeezing strength. Higher pump powers, in turn, might lead to changing conditions for optimal phase matching and simultaneous double resonance due to heating of the crystal. However, the squeezed-light source is easier to operate in a regime where heating of the crystal does not have an influence on the optimal temperature settings and thus the pump power should be kept as small as possible. Another source for the degradation of the squeeze strength is phase noise [Oel16, Dwy13]. It results from fluctuations of the relative phase of the local oscillator and the squeezed field. Thus, the measurement angle is not constantly aligned with the squeeze angle and noise from the anti-squeezed quadrature is projected into the squeezed quadrature, reducing the observable squeezing strength. Assuming that the phase jitter is normally distributed and has a small standard deviation, the effect of phase noise on the squeezing and anti-squeezing spectra given by equation (2.102) can be described by [Aok06, Vah16]:

$$S_{\mathrm{sqz}}\left(\tilde{\Theta}\right) = S_{\mathrm{sqz}}\left(f\right)\cos^2\left(\tilde{\Theta}\right) + S_{\mathrm{asqz}}\left(f\right)\sin^2\left(\tilde{\Theta}\right) \tag{4.3}$$

$$S_{\mathrm{asqz}}\left(\tilde{\Theta}\right) = S_{\mathrm{asqz}}\left(f\right)\cos^2\left(\tilde{\Theta}\right) + S_{\mathrm{sqz}}\left(f\right)\sin^2\left(\tilde{\Theta}\right). \tag{4.4}$$

The phase noise $\tilde{\Theta}$ was not included in the fits presented in figure 4.4 since it was found to be negligible. Figure 4.5 illustrates how significant phase noise would influence our best spectrum with $\epsilon = 85.7\,\%$. The effect of phase noise becomes more crucial if high squeeze factors are measured and reduces the maximum observable squeezing. Our simulations show that a deviation from the fit can be observed for values of $\tilde{\Theta} > 2 \times 10^{-3}\,\text{rad}$. Thus, we estimate 2 mrad to be the upper limit for phase noise in our experiment. This amount does not lead to a degradation of the squeeze strength in the frequency range between 3 MHz and 25 MHz.

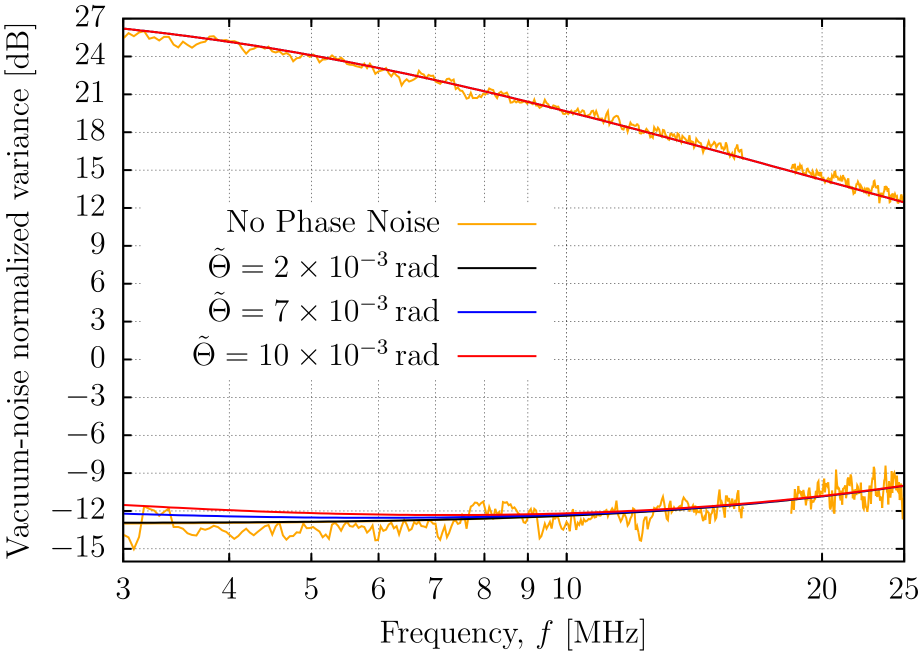

Figure 4.5: Effect of phase noise on the spectrum with $\epsilon = 85.7\,\%$. A deviation from the fit with zero phase noise occurs for values of $\tilde{\Theta} > 2 \times 10^{-3}\,\text{rad}$. This is the upper limit for phase noise in our experiment in the given frequency range. The picture shows that the black and yellow traces hardly deviate from each other. Thus, phase noise does not limit the observable squeezing, the optical losses are more significant. The anti-squeezing is not affected by phase noise and all traces overlay.

5 Squeezing in the audioband

The generation of squeezed vacuum states in the frequency range from a few Hz to several hundred Hz is especially interesting for gravitational wave detection, as already mentioned in the introduction. Other potential applications that profit from squeezing at low frequencies are optomechanical experiments, in which the vibrations of oscillators are coupled to a laser [Kau13, Saw17]. In this section, we present the detection system that we used to characterize the squeezed vacuum source in this frequency range as well as the squeezing measurements.

5.1 Audioband balanced homodyne detector

For the detection of squeezed light in the acoustic frequency range, a new homodyne detector was developed since the system that was used for the measurements presented in chapter 4 was designed for the detection of squeezing in the MHz range in other experiments of the working group.
The new detector was designed such that the electronic dark noise is as small and as flat as possible in a frequency range from 10 Hz to 100 kHz. The design and further information are presented in appendix 1. Figure 5.1 shows the darknoise floor of our detector in black. It is flat between 300 Hz and 10 kHz. For frequencies below 300 Hz, the darknoise increases. This behavior most likely results from noise of the operational amplifier that was used for the electronic transimpedance amplifier that converted the current resulting from the subtraction of the photocurrents of the two diodes to a voltage. For frequencies that are higher than 10 kHz, the noise increases as well. It is possible that this results from other electronic devices in the lab that couple into the detection system via the mains. However, the detector can be used to detect squeezing in the range from 10 Hz to 100 kHz if the relation between the local oscillator power and the respective vacuum noise power is linear.
In the audioband, it is more difficult to achieve such a quantum limited measurement for several reasons that are also explained in [Vah07, Ste12, McK07]. An important limitation is technical noise that originates from the laser source. Our filter cavities have a linewidth of 1 MHz and do not suppress any technical laser noise below this frequency. This noise couples into the measurement via the local oscillator of the homodyne detector and can only be suppressed with good balancing of the detection system. Good balancing means that the optical powers that are detected by both diodes of the homodyne detector are equal. In that case, the technical laser noise cancels out because it is common on both diodes. Figure 5.1 shows the noise powers from a local oscillator beam of 0.07 mW, recorded with each single photo diode of the

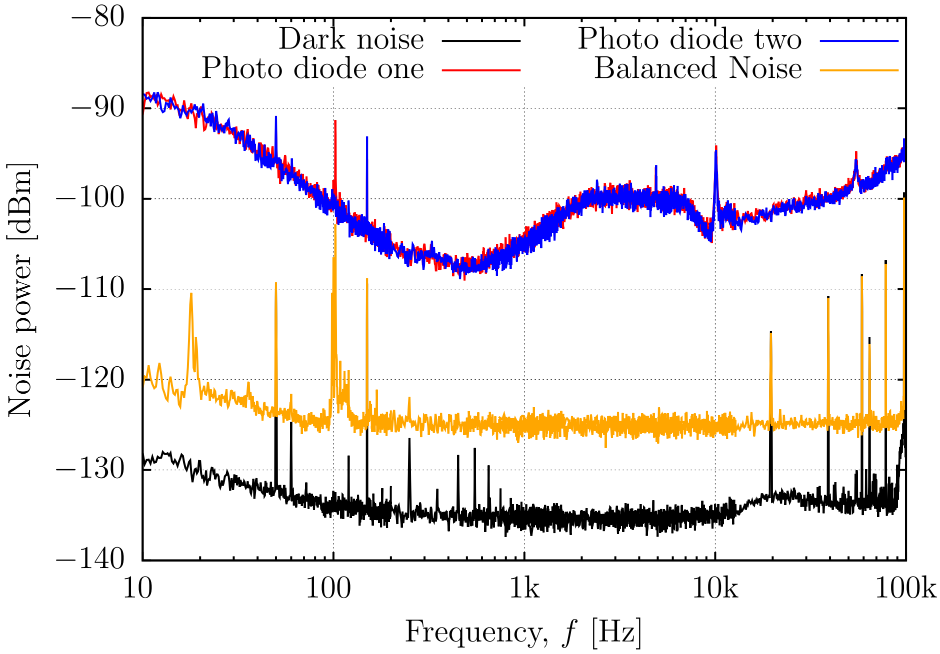

Figure 5.1: The picture illustrates how the balanced homodyne detector cancels out the technical noise resulting from the laser. The black trace shows the dark noise that is recorded without any light on the photo diodes. The red and the blue trace show the noise power that is recorded with each individual diode with 0.07 mW local oscillator power, which means that 0.035 mW is impinging on each diode. If both diodes detect that power simultaneously, the noise power shown in the orange trace results, representing a vacuum state. The traces were pieced together from five individual measurements with line widths of 128 Hz, 16 Hz, 8 Hz, 2 Hz, 0.25 Hz. Each trace was averaged 50 times, 800 FFT lines were recorded.

detector in red and blue and with the balanced setup in orange. Apart from that, the red and blue trace indicate that the noise from the laser is not flat across the entire frequency range. However, in the balanced homodyne system, the noise cancels out, resulting in the flat orange trace that shows the noise of a vacuum state, measured with a local oscillator power of 0.07 mW.

Figure 5.2 shows more spectra of vacuum noise measurements for different local oscillator powers. The traces were pieced together from five individual measurements with line widths of 128 Hz, 16 Hz, 8 Hz, 2 Hz, 0.25 Hz. Each trace was averaged 50 times, 800 FFT lines were recorded. Figure 5.3 shows the same measurements. Those traces were not only normalized to 1 Hz resolution bandwidth, but also to the local oscillator power according to:

$$P_{\text{normalized}}\,[\text{dBm}] = P_{\text{recorded}}\,[\text{dBm}] - 10\log\left(\frac{\text{RBW [Hz]}}{1\,\text{Hz}}\right) - 10\log\left(\frac{\text{P}_{\text{LO}}\,[\text{mW}]}{1\,\text{mW}}\right).$$

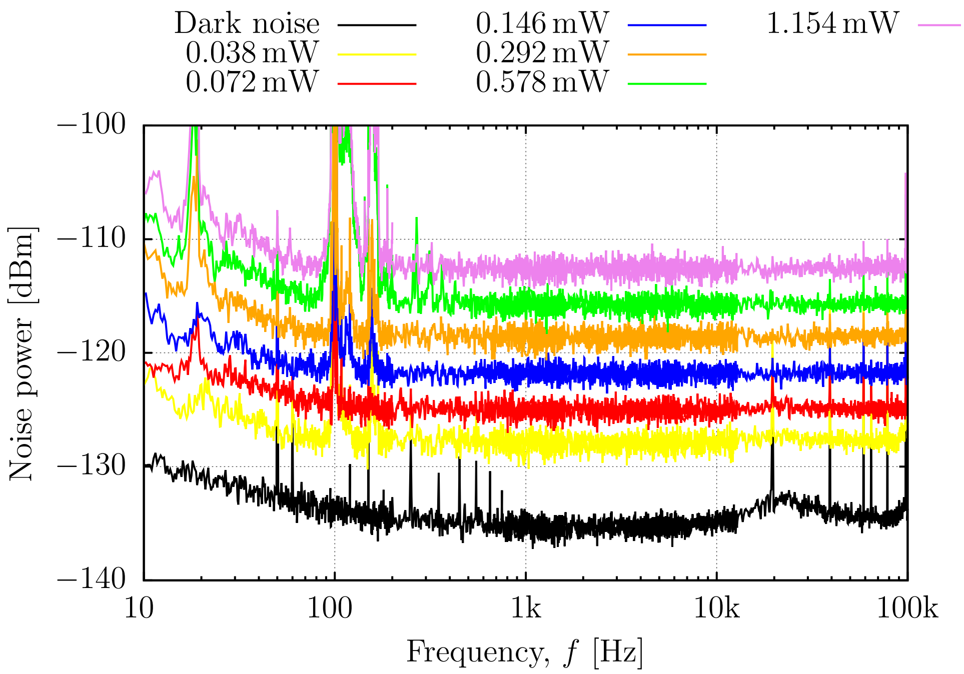

Figure 5.2: Vacuum noise power between 10 Hz and 100 kHz measured with different local oscillator powers. Doubling the local oscillator power leads to a 3 dB increase in noise power, indicating the linearity of the detection system. The traces were pieced together from five measurements taken with line widths of 128 Hz, 16 Hz, 8 Hz, 2 Hz, 0.25 Hz and normalized to 1 Hz resolution bandwidth. 800 FFT lines were recorded for every measurement and the measurements were averaged 50 times.

As already discussed in chapter 4.2, the fact that the traces overlay from 30 Hz to 90 Hz and from 200 Hz to 100 kHz indicates the linearity of the balanced homodyne system within this region. The peaks between 20 kHz and 100 kHz most likely result from electronic devices in the lab that couple into the experiment. Between 90 Hz and 200 Hz, further peaks are visible. The peak centered around 100 Hz can arise from a higher harmonic of the peak that is visible at 50 Hz. It originates from the frequency of the mains. The irregularity of the traces between 90 Hz and 200 Hz indicates that noise, potentially coupling in from stray light, is limiting the measurement within this region. This limitation arises from scattering and parasitic interferences. As described in [Ste12], light can be scattered out of the beam path by dust particles or surface imperfections and reenter it later, resulting in an intensity modulation. If the light is not scattered out of the path, it can travel back and forth between optical components, for example lenses, leading to parasitic cavities. If the scattering occurs in the local oscillator path before it impinges on the beam splitter, good balancing can suppress the resulting disturbances since they will be common on both diodes. Scattering that occurs after the beamsplitter or in the signal path is more critical.

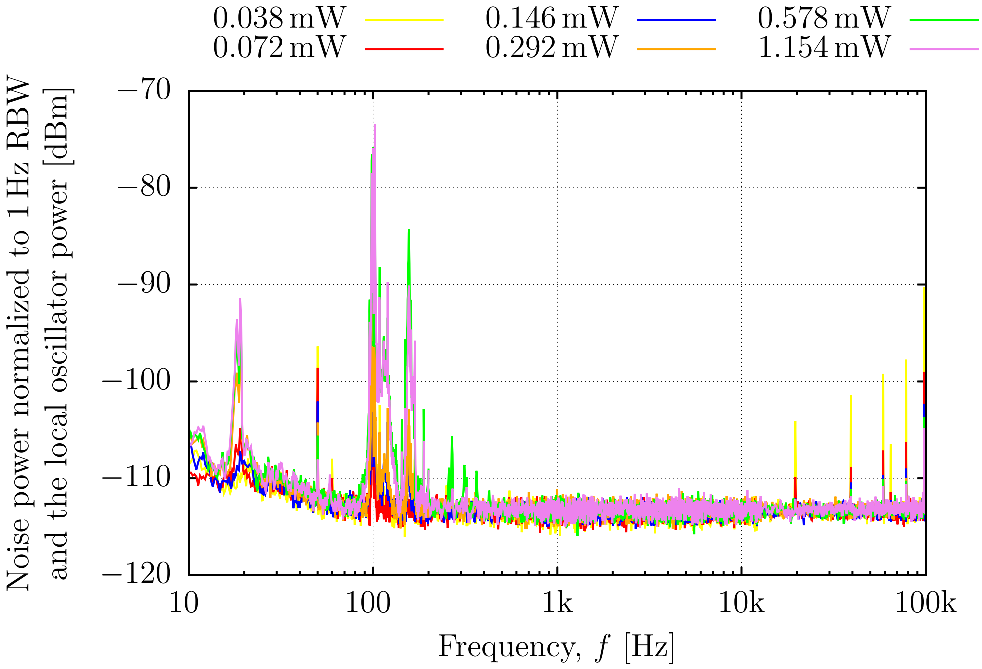

Figure 5.3: Same data as in figure 5.2, not only normalized to 1 Hz resolution bandwidth, but also to the local oscillator power that was used for the respective measurement. The fact that the traces overlay also indicates the linearity of the system. The traces were pieced together from five measurements taken with line widths of 128 Hz, 16 Hz, 8 Hz, 2 Hz, 0.25 Hz. 800 FFT lines were recorded for every measurement and the measurements were averaged 50 times.

If the scattering occurs in only one of the two paths after the beam splitter, it is not common on both diodes and cannot be canceled by the common mode rejection. Stray light that couples into the signal path and travels back to the homodyne detector is even more crtical. In a squeezing experiment, where the measured quantum state only contains very little pairs of correlated photons, every additional photon leads to a reduced quantum noise suppression. For the measurements presented in figure 5.2 and 5.3, we blocked the path from the beamsplitter to the parametric down-conversion cavity. If it was not blocked, we measured shot noise spectra as shown in figure 5.4 and it becomes apparent that our setup was limited by stray light that does not leave the optical path. The red trace was recorded with the path to the parametric down-conversion cavity being open and the blue trace with the path being blocked. The additional noise between 10 Hz and 900 Hz results from light that is reflected off the surfaces of our diodes and the lenses in front of the diodes, travels along the signal path to the parametric down-conversion cavity and reenters the homodyne detector after being reflected off the incoupling mirror of the parametric down-conversion cavity.
There are two reasons for the significant scattering. First, the lenses used in this experiment were not superpolished and thus did not have a well specified micro roughness. Instead, we used standard optics.

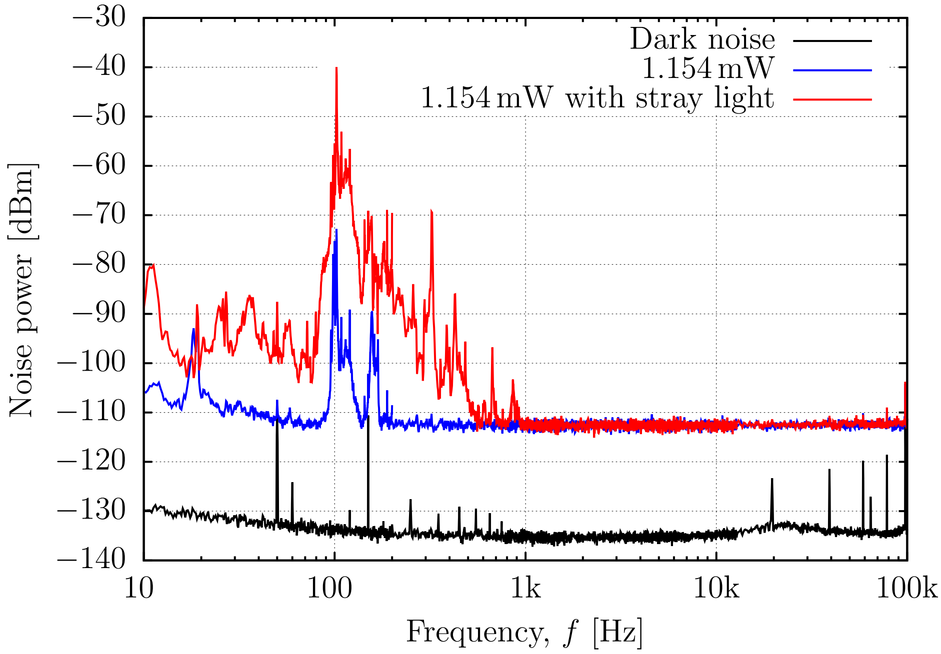

Figure 5.4: The figure illustrates how stray light limits the frequency range in which the homodyne detector can be used for the characterization of the squeezed states. The vacuum noise level was determined with 1.154 mW local oscillator power with the path to the parametric down-conversion cavity being blocked (blue trace) and open (red trace). When the path is opened, additional noise between 10 Hz and 900 Hz becomes apparent. This noise results from scattered light that is back reflected to the homodyne detector by the incoupling mirror of the parametric down-conversion cavity.

Second, the diameter of the active area of the high efficiency photo diodes used for the low frequency measurements was only 100 μm. Thus, it was not possible to tilt the diodes such that the residual reflections from the anti-reflective coating of the active area were scattered out of the original beam path. Other issues that can limit the detection of squeezing at small frequencies are acoustics that couple into the experiment and beam pointing. Acoustic noise in the laboratory, for example from fans or closing doors, can move mirror mounts and thus couple into the measurement. We observed noise coupling to the experiment especially when squeezing was measured. Moving around in the lab or doors to other labs that were closed were visible as peaks in our spectra. The data were taken when the oscillations due to this acoustic coupling had declined. Lowering the power of the air conditioning did not lead to a significant improvement of our experiment, indicating that this was not the most significant noise source. Moving mirror mounts due to acoustics that couple into the setup can also result in beam jitter. This can lead to a movement of the focus of the laser beam on the diodes of the homodyne detector. If the active surface is not homogeneous, the quantum efficiency depends on where the laser beam impinges on the diodes and the movement of the beam adds additional noise. Since this noise is not common, it cannot be canceled out with good balancing. However, a large spot size can average out the inhomogeneities. Varying the spot size was not possible in our experiment since a diameter of 100 μm is already very limiting. The homodyne detector was aligned such that cutting off parts of the beam due to a too large spot and jitter was unlikely.

5.2 Squeezing from 1 kHz to 100 kHz

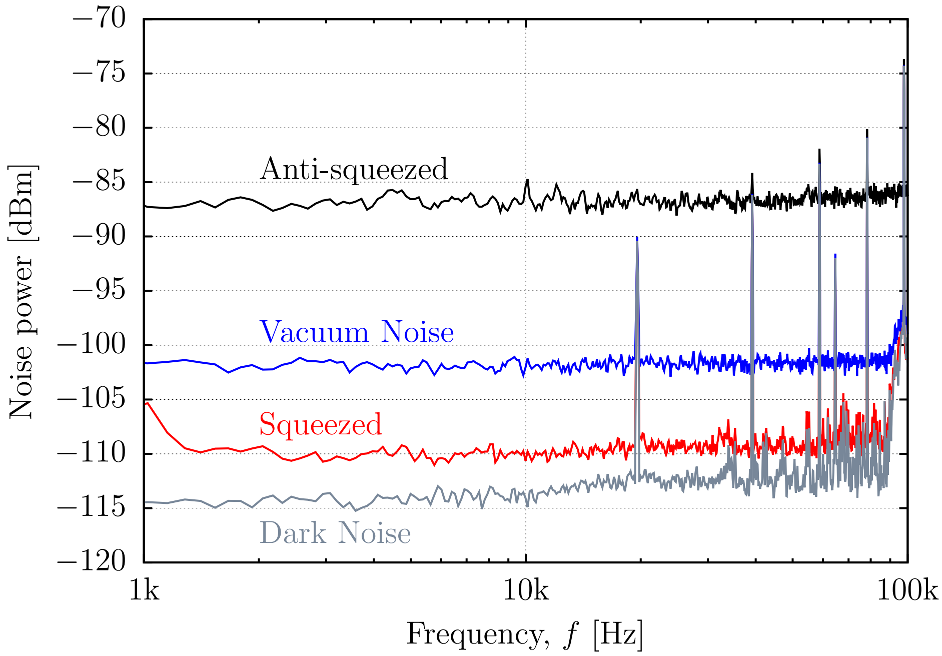

Figure 5.5: Squeezing measurement between 1 kHz and 100 kHz. 8.2 dB of squeezing were directly observed with 15.1 dB anti-squeezing. The pump power was 8.5 mW and the maximal dark noise clearance 12.1 dB. Each trace was recorded with a bandwidth of 128 Hz. 800 FFT lines and 50 averages were taken.

Figure 5.5 shows a squeezing spectrum between 1 kHz and 100 kHz. About 8.1 dB squeezing with 15.1 dB anti-squeezing were directly observed between 2 kHz and 10 kHz. Above 10 kHz, the slightly higher dark noise level decreases the observable squeezing. Figure 5.6 shows the same measurement, but the data were corrected from dark noise and normalized to the vacuum level. The dark noise corrected squeezing level is about 10.17 dB and the corresponding anti-squeezing level 15.44 dB. Those values were obtained from linear fits to the data in the range from 3 kHz to 80 kHz. Data below 3 kHz were omitted to ensure that the stray light does not impact the fits. Above 80 kHz, the dark noise is too close to the measured squeezing and too much noise from the electronics in the lab couples into the measurement.
The local oscillator power was chosen such that the effects due to incoupling stray light were minimized and high squeezing levels were still observable. However, in both figures 5.5 and 5.6, a peak around 1 kHz is still visible that results from stray light. As for the measurements at MHz frequencies, these data were recorded without using the coherent control lock but by aligning the relative phases of the squeezed state and the local oscillator manually. The temperature settings were also not changed. For the measurements, we used a pump power of 8.5 mW at 775 nm.

It was not possible to use higher pump powers for the measurements since the dark noise clearance of 12.1 dB is limiting the squeezing that can be observed. For the direct observation of higher squeezing levels, the local oscillator power has to be increased. This, however, increased the amount of stray light coupling into the parametric down-conversion cavity which made the measurements unstable. As before, the vacuum level was recorded immediately after the squeezing and anti-squeezing spectra were taken with the path to the parametric down-conversion cavity being blocked, minimizing the effect of power fluctuations that could change the vacuum reference level. The traces were recorded with a bandwidth of 128 Hz. 800 FFT lines and 50 averages were taken.

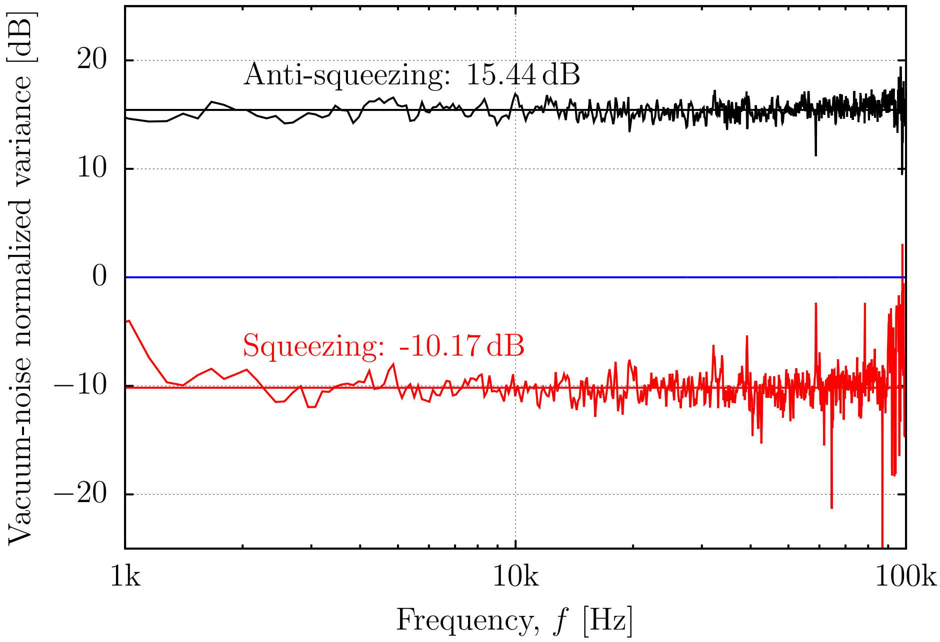

Figure 5.6: Dark noise corrected squeezing spectrum of the data presented in figure 5.5. Subtracting the dark noise from the vacuum, the squeezing spectrum and the anti-squeezing spectrum result in 10.17 dB squeezing with 15.44 dB anti-squeezing, respectively. Those values were deduced from fits between 3 kHz and 80 kHz.

5.3 Loss analysis

Figures 5.6, 5.7 and 5.8 show dark noise corrected squeezing measurements that were obtained for different pump powers. The squeezing and anti-squeezing levels were deduced from linear fits as explained before. In chapter 2.2.3, we described a model for squeezing measurements with losses. We recall that the squeezing and anti-squeezing spectra that include losses can be expressed as:

$$S_{\eta,\mathrm{sqz}}(f) = \eta S_{\mathrm{in,sqz}}(f) + (1-\eta)\, S_{\mathrm{vac}}(f)\,, \tag{5.1}$$

$$S_{\eta,\mathrm{asqz}}(f) = \eta S_{\mathrm{in,asqz}}(f) + (1-\eta)\, S_{\mathrm{vac}}(f)\,. \tag{5.2}$$

Here, $S_{\mathrm{in,sqz}}$ and $S_{\mathrm{in,asqz}}$ describe the initial squeezing and anti-squeezing values that would be measured if the state did not experience any losses. Recalling that

$$S_{\mathrm{in,sqz}}(f) = \frac{1}{S_{\mathrm{in,asqz}}(f)},$$

and inserting it in equation 5.1 we get:

$$\frac{S_{\eta,\mathrm{sqz}}(f) - (1-\eta)}{\eta} = \frac{1}{S_{\mathrm{in,asqz}}(f)}.$$

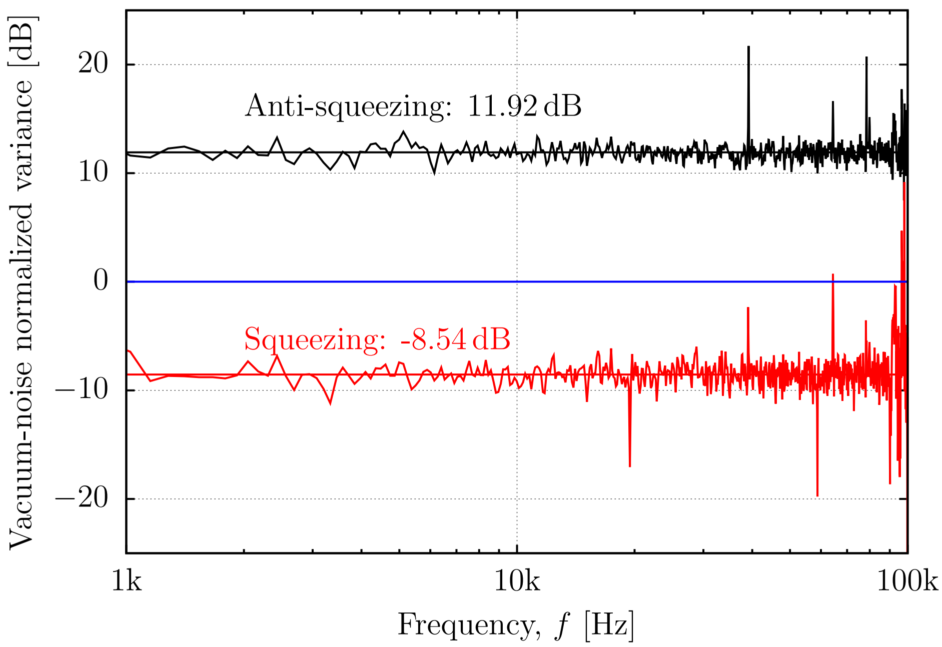

Figure 5.7: Squeezing measurement with 5.4 mW pump power. This pump power led to a squeezing strength of 8.54 dB with 11.92 dB anti-squeezing. These values were obtained from fits between 3 kHz and 80 kHz. 800 FFT lines and 50 averages were taken with a bandwidth of 128 Hz.

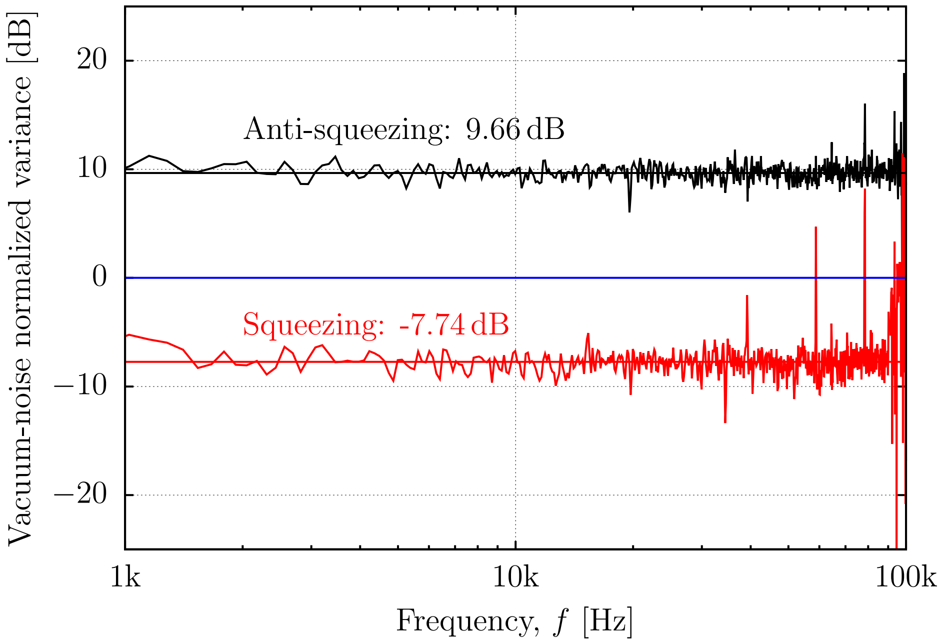

Figure 5.8: Squeezing measurement with 3.9 mW pump power. This pump power led to a squeezing strength of 7.74 dB with 9.66 dB anti-squeezing. These values were obtained from fits between 3 kHz and 80 kHz. 800 FFT lines and 50 averages were taken with a bandwidth of 128 Hz.

With equation 5.2, we obtain:

$$\frac{\eta}{S_{\eta,\mathrm{sqz}}(f)-(1-\eta)}=\frac{S_{\eta,\mathrm{asqz}}(f)-(1-\eta)}{\eta}.$$

From this equation, we get:

$$\eta^2=\left[S_{\eta,\mathrm{asqz}}(f)-(1-\eta)\right]\left[S_{\eta,\mathrm{sqz}}(f)-(1-\eta)\right]$$

and finally for the efficiency η:

$$\begin{aligned}\eta &= \frac{1+S_{\eta,\mathrm{sqz}}(f)\,S_{\eta,\mathrm{asqz}}(f)-S_{\eta,\mathrm{sqz}}(f)-S_{\eta,\mathrm{asqz}}(f)}{2-S_{\eta,\mathrm{sqz}}(f)-S_{\eta,\mathrm{asqz}}(f)}\\ &= 1-\frac{1-S_{\eta,\mathrm{sqz}}(f)\,S_{\eta,\mathrm{asqz}}(f)}{2-S_{\eta,\mathrm{sqz}}(f)-S_{\eta,\mathrm{asqz}}(f)}.\end{aligned} \tag{5.3}$$

With this equation, the total detection efficiency can be calculated from the dark noise corrected squeezing and anti-squeezing values. For the data in figure 5.6, we get $\eta \approx 0.93$ and for those in figure 5.7 and 5.8, $\eta \approx 0.91$ and $\eta \approx 0.93$, respectively. Table 5.1 summarizes data obtained from more measurements. The average detection efficiency is $\eta = 0.928$.
Compared to the value of $\eta = 0.952$ for the measurements at MHz frequencies, the losses increased by 2.4%. The quantum efficiency of the new diodes is also specified

to be around $\eta_{\mathrm{PD}} \approx 0.99$. However, due to the small diameter of the active area of only 100 μm, additional lenses had to be used to focus the beam down to a sufficiently small spot size, introducing more anti-reflectively coated surfaces and increasing the losses and scattering. Apart from that, the anti-reflective coating of the active area is designed such that an efficiency of $\eta_{\mathrm{PD}} \geq 0.99$ is only guaranteed by the manufacturer for s-polarized light and an angle of incidence of 10 degrees. We positioned the diodes under a smaller angle to avoid an elliptical beam shape on the active surface and to ensure that the entire laser spot impinges on the surface. This most likely also increased the losses, resulting in a the total additional loss of 2.4 %.

Measurement	Squeezing [dB]	Anti-squeezing [dB]	η
1	-10.17	15.44	0.929
2	-10.3	14.44	0.938
3	-8.34	11.3	0.916
4	-8.26	10.67	0.924
5	-10.06	15.46	0.926
6	-8.54	11.92	0.914
7	-7.74	9.66	0.925
8	-10.25	14.66	0.936
9	-10.21	14.83	0.933
10	-10.48	15.18	0.937
11	-10.06	15.24	0.927
12	-10.36	14.77	0.937
13	-10.2	15.39	0.93
14	-10.34	16.12	0.929
15	-10.57	15.94	0.935
16	-10.38	15.97	0.93
17	-10.21	16.23	0.925
18	-10.05	15.89	0.923
19	-10.29	16.28	0.927
20	-10.19	15.77	0.927
Average:			0.928

Table 5.1: Total detection efficiencies that were calculated with equation 5.3 from different measurements. Measurement three, four, six and seven were performed with smaller pump powers. The squeezing and anti-squeezing values were deduced from fits to the dark noise corrected spectra as described before.

5.4 Squeezing below 1 kHz

Squeezing measurements below 1 kHz were limited by stray light, as already indicated by figure 5.4. Figure 5.9 shows a squeezing measurement that also includes the range from 50 Hz to 1 kHz. It is possible to observe a noise reduction below the vacuum level down to a frequency of 500 Hz. Below that frequency, the stray light not only limits the observable squeezing but also increases the anti-squeezing. Above 3 kHz, we observed 5.7 dB of squeezing with 11.06 dB of anti-squeezing in this measurment. The shot noise was measured with the path from the parametric down-conversion cavity to the homodyne detector being blocked. The traces presented in this section were recorded with 800 FFT lines and a resolution bandwidth of 8 Hz. The dark noise and the vacuum were averaged 100 times, the squeezing and anti-squeezing traces 50 times.

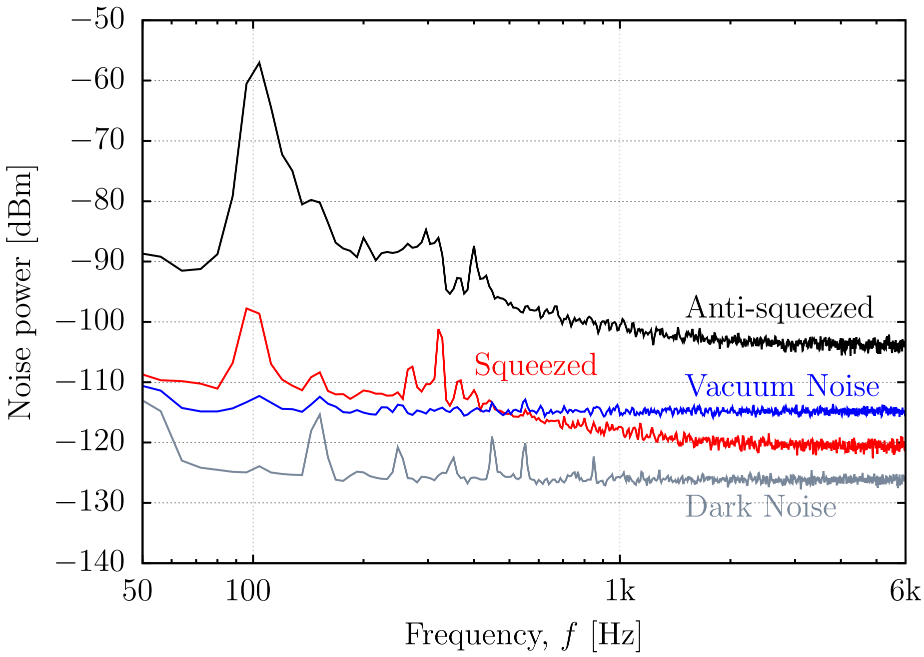

Figure 5.9: Squeezing spectrum between 50 Hz and 6 kHz. Squeezing can be observed down to frequencies of 500 Hz. Below that frequency, the stray light introduces too much noise. To decrease the coupling of the stray light to the measurement via parametric amplification, the pump power was reduced. Above 3 kHz, 5.7 dB squeezing and 11.06 dB anti-squeezing were observed. The traces were recorded with 800 FFT lines and a resolution bandwidth of 8 Hz. The dark noise and the vacuum were averaged 100 times, the squeezing and anti-squeezing traces 50 times.

The corresponding dark noise corrected spectrum is shown in figure 5.10. From linear fits between 3 kHz and 6 kHz, we inferred an overall detection efficiency of $\eta = 0.843$.

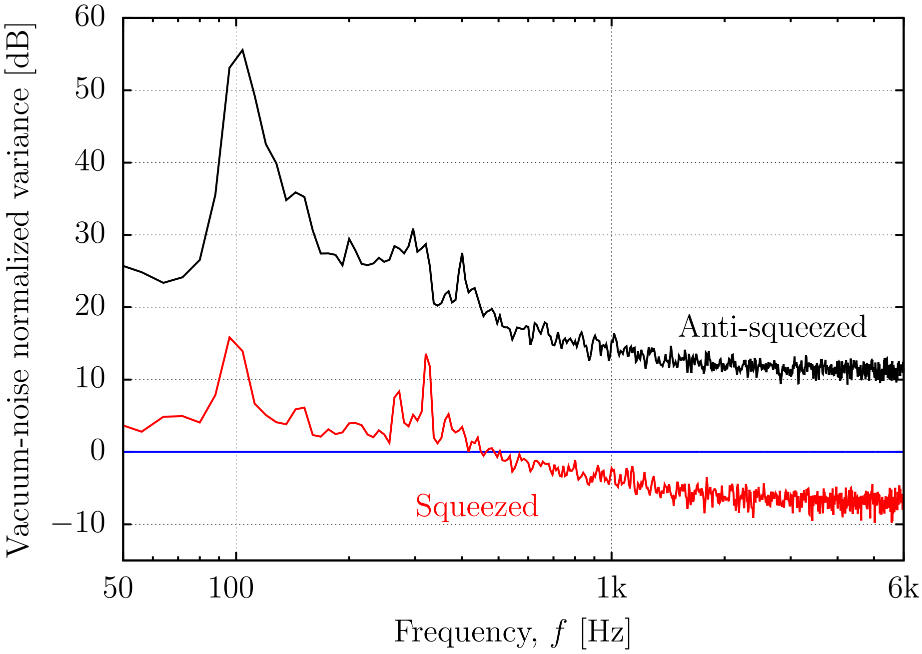

Figure 5.10: The spectrum presented in figure 5.9 with dark noise correction and normalized to the vacuum noise level. From linear fits to the data in the range from 3 kHz to 6 kHz, we inferred an efficiency of $\eta = 0.843$. The data were taken with the same setup as the measurements above 1 kHz. Instabilities in the coherent control scheme that was used to lock the homodyne readout phase as well as the phase of the pump field due to the stray light that couples into the parametric down-conversion cavity reduce the observable squeezing. These effects resemble optical losses in appearance in the spectrum. The traces were recorded with 800 FFT lines and a resolution bandwidth of 8 Hz. The dark noise and the vacuum were averaged 100 times, the squeezing and anti-squeezing traces 50 times.

Compared to the average detection efficiency calculated in table 5.1, the efficiency decreased by 0.085. Compared to measurements number 3,4 and 6 presented in the table, we also see that we observed less squeezing with similar anti-squeezing values in this measurement. The anti-squeezing values are similar because equal pump powers were chosen for these three measurements and the data presented in this subsection. However, we used the coherent control locking loop to record the data below 1 kHz. Most likely, the stray light that couples into the cavity introduced noise into the locking loop, which influences its stability. Thus, the noise was fed back to the measurement, reducing the observable squeezing. Apart from that, the stray light can initiate an optical parametric amplification in the cavity, introducing more noise into the measurement [McK04]. We minimized the effect of optical parametric amplification in the cavity by reducing the pump power at 775 nm to the value of measurement number 3,4 and 6 in table 5.1. To further mitigate the issues that are introduced by stray light, a Farady isolator can be placed between the homodyne detector and the parametric down-conversion cavity, as described in [McK04]. This way, the stray light can be suppressed at the expense of additional losses from the isolator. Unfortunately, the limited space in our compact setup did not allow for the integration of an isolator for comparison without rearranging other major components.

6 Outlook

The analysis and characterization of the squeezing source developed within this thesis point out steps that can be implemented to improve the squeezing strength, further reduce the footprint and simplify the setup. Within this chapter, these steps will be presented for future developments.

6.1 Digital locking scheme for squeezed vacuum states

The implementation of the coherent control scheme not only enables squeezing measurements below 1 kHz, but also the stable application of the quantum state in downstream experiments, for example laser interferometers. As already described, the pump phase determines the quadrature that is squeezed. By locking the pump phase, this quadrature can be chosen and fixed over time. By locking the local oscillator phase, the quadrature that is read out is chosen and can be aligned with the squeezed quadrature. Within this thesis, the squeezed vacuum states were not applied to a downstream experiment, but the compact and transportable setup can be used for that purpose.
An alternative to the coherent control scheme to choose the correct quadrature is depicted in figure 6.1. The acousto-optic modulator that generates the single sideband has been removed and the phase shifter used to adjust the pump phase has been replaced by a phase shifter in the path that guides the squeezed state from the parametric down-conversion cavity to the homodyne detector. To align the squeezed quadrature with the homodyne readout quadrature or a downstream experiment, it is sufficient to adjust the phase of the squeezed state. The pump phase does not have to be stabilized if squeezed vacuum is generated. Thus, for applications that require squeezing in only one quadrature across the entire bandwidth of the parametric down-conversion cavity, it is only necessary to lock the phase of the squeezed field.
This can be done without a single sideband, which significantly reduces the footprint of the squeezed-light source. Instead, digital locking techniques can be applied, further simplifying the setup. Digital locking techniques have been investigated recently and are of interest because of their flexibility and low cost. In [Spa11], a locking scheme based on the Pound-Drever-Hall method is described. Here, the error signal is generated using phase modulation sidebands imprinted on the field that interacts with the cavity to be locked, but processing of this error signal is done digitally with a field programmable gate array and a LabView software. In [Hua14], a microcontroller is used to lock a Mach-Zehnder interferometer, a cavity with a finesse of 100 and a cavity with a finesse of 1000.

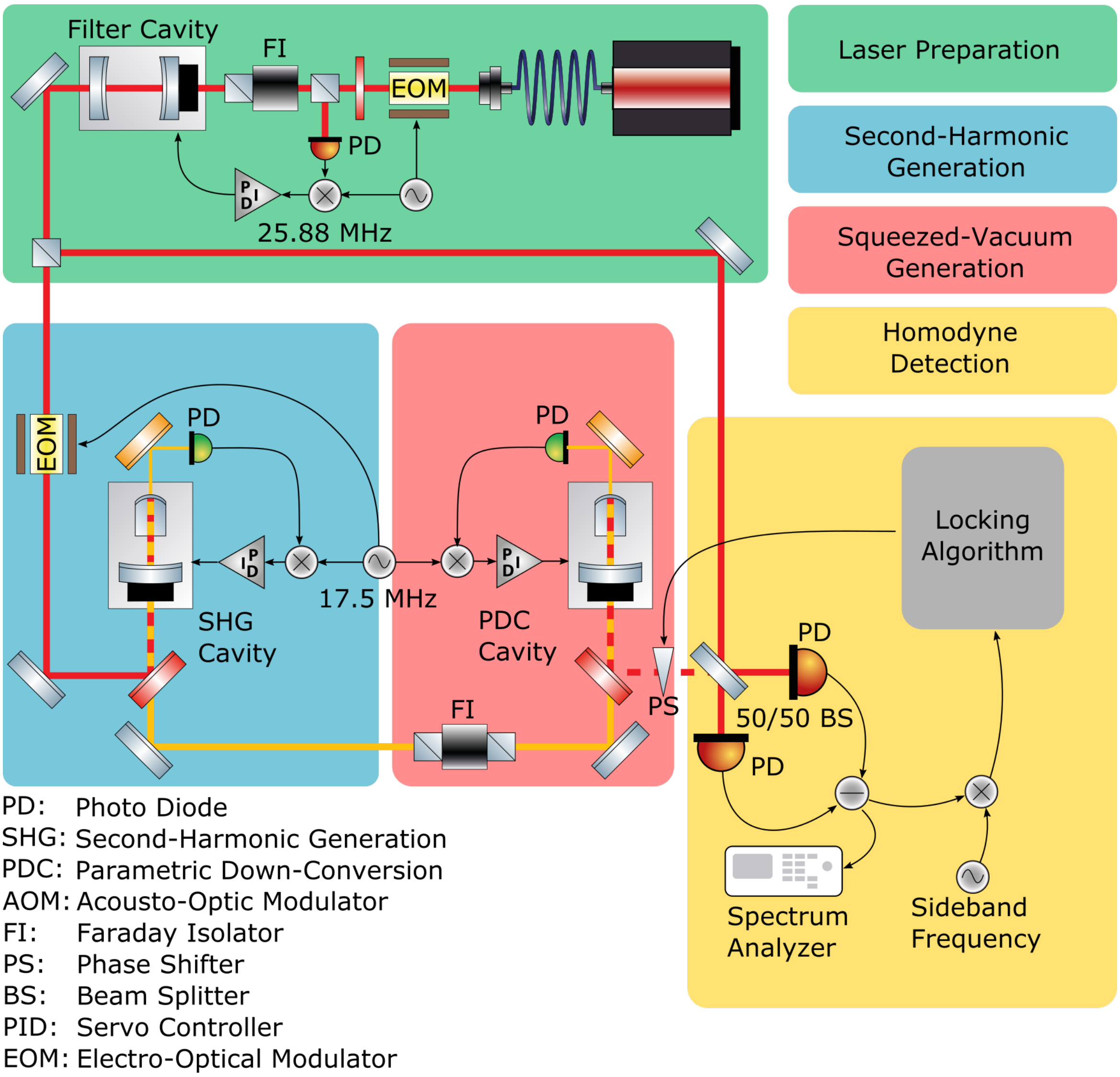

Figure 6.1: Illustration how a digital locking algorithm can further reduce the footprint of the experimental setup and enable locking the squeezed quadrature to a downstream experiment. Compared with figure 3.2, the single sideband generation section as well as the analog locking loops for the pump phase and the local oscillator phase have been removed. Instead, only the phase of the squeezed field is adjusted with a phase shifter. The phase shifts of the local oscillator and pump field are due to temperature drifts. Since these drifts are slow, it is sufficient to align the phase of the squeezed quadrature with the local oscillator to enable the detection or application of the squeezed state.

The techniques described in this publication do not rely on the Pound-Drever-Hall method to generate an error signal, reducing the number of required optical components even further while retaining comparable results. The lock is based on an algorithm that searches the maximum or minimum of a time dependent signal instead. A similar procedure can be used to lock the squeezed quadrature of a squeezed vacuum state to an experiment or, as depicted in figure 6.1, to a homodyne detector. The working principle of such a lock is illustrated in figure 6.2. It combines the measurement principle of a spectrum analyzer as described in [Rau11] with the searching algorithm described in [Hua14]. To determine the noise power of a signal at the frequency f_{LO}, the input signal is multiplied with an electronic local oscillator with a frequency f_{LO}. Mathematically, this multiplication results in a signal given by:

$$
\begin{aligned}
&\delta\alpha_{\mathrm{sig}} \sin\left(2\pi f_{\mathrm{sig}} t\right) \alpha_{\mathrm{LO}} \sin\left(2\pi f_{\mathrm{LO}} t\right) \propto \\
&\delta\alpha_{\mathrm{sig}} \alpha_{\mathrm{LO}} \left[\cos\left(2\pi\left(f_{\mathrm{sig}} - f_{\mathrm{LO}}\right) t\right) - \cos\left(2\pi\left(f_{\mathrm{sig}} + f_{\mathrm{LO}}\right) t\right)\right]
\end{aligned}
$$

with $\delta\alpha_{\mathrm{sig}}$ and $\delta\alpha_{\mathrm{LO}}$ representing the noise of the signal and the local oscillator, respectively. For the locking scheme, the term proportional to $\cos\left(2\pi\left(f_{\mathrm{sig}} + f_{\mathrm{LO}}\right) t\right)$ is filtered out with a low pass. The remaining term $\delta\alpha_{\mathrm{sig}}\delta\alpha_{\mathrm{LO}} \cos\left(2\pi\left(f_{\mathrm{sig}} - f_{\mathrm{LO}}\right) t\right)$ provides the input signal for the algorithm that searches the minimal noise power at f_{LO} since it contains information about the fluctuation of the signal.
For $f_{\mathrm{LO}} < f_{\mathrm{sig}}$, the noise at f_{LO} is mixed down to a smaller intermediate frequency. For example, a signal at a few MHz can be multiplied with a local oscillator with a smaller frequency. The resulting difference frequency is easier to analyze electronically since it is much smaller than f_{LO}, avoiding limitations due to finite electronic bandwidths. For $f_{\mathrm{LO}} = f_{\mathrm{sig}}$, we obtain a constant signal that contains information about both the amplitudes of the local oscillator and the signal.
The power of the electronic local oscillator noise $\delta\alpha_{\mathrm{LO}}$ is not time dependent and does not change. However, the noise power of the signal $\delta\alpha_{\mathrm{sig}}$ does vary when the phase of the squeezed field changes. It is minimal when the homodyne detector measures the squeezed quadrature and maximal when it measures the anti-squeezed quadrature. This fact can be used for the locking algorithm.
Two implementations are possible. First, the voltage that results from the multiplication with f_{LO} is low pass filtered and measured multiple times. Afterwards, the variance of this data stream is calculated. It is the smallest when the phase of the optical local oscillator of the homodyne detector is aligned with the squeezing angle, resulting in the minimal variance. Slightly changing the phase of the squeezed field, repeating the measurement and the calculation of the variance and comparing the old value with the new one gives an error signal. If the change of the squeezing phase results in a smaller variance and thus a smaller noise power than before, the same step has to be repeated. If the variance increases, the step has to be reversed. This way, it is possible to lock the phase of the squeezed field to the local oscillator and perform a long term squeezing measurement or lock the squeezed state to a downstream experiment. However, it is important to perform only small variations on the phase of the squeezed field. If the steps are too large, the lock adds additional phase noise to the squeezed state, reducing the maximal detectable squeezing. A first implementation of this principle was demonstrated in [Abd17] to lock two squeezed fields on two balanced homodyne detectors orthogonally to each other, that is to say one detector measured

the squeezed quadrature while the other one measured the anti-squeezed quadrature. The local oscillator frequency used to demodulate the signal that was obtained from the homodyne detectors was chosen to be $f_{\mathrm{LO}} = 5\,\mathrm{MHz}$.

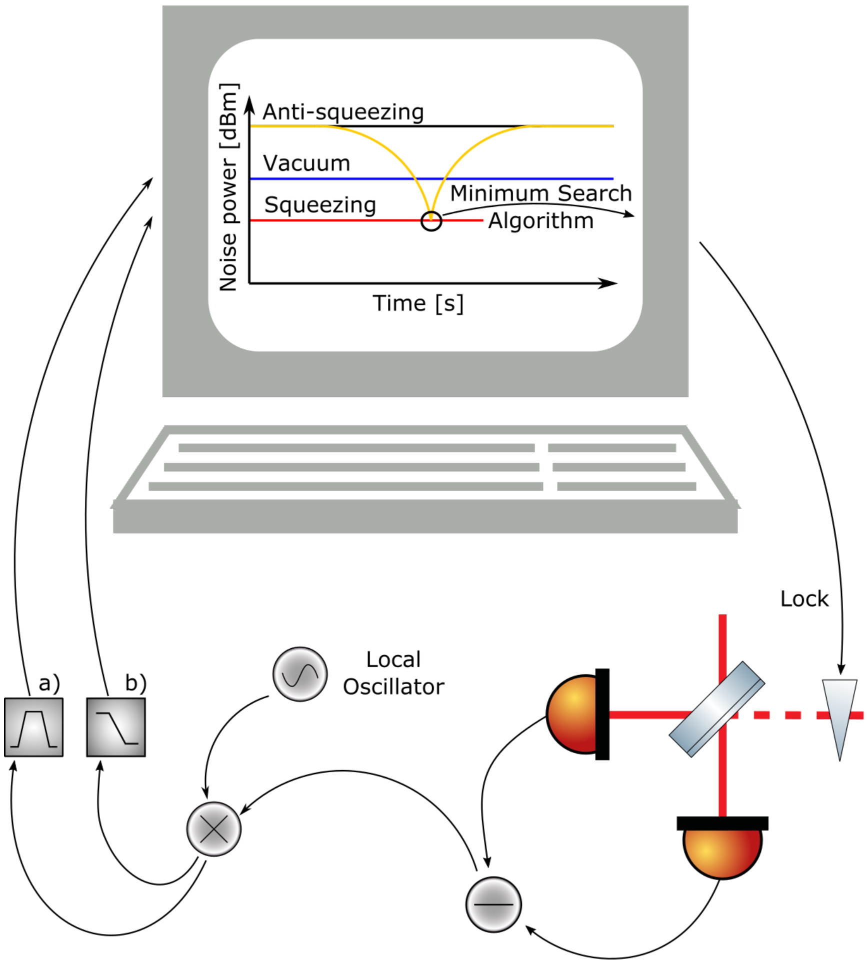

Figure 6.2: Illustration of the algorithm that can be used to lock the phase of the squeezed state. The signal of the homodyne detector, or alternatively the signal coming from a downstream experiment, is electronically mixed with a frequency at which strong squeezing can be expected. The signal that has been mixed down can either be low pass filtered (b, tested in [Abd17]) or band pass filtered (a). Depending on the phase of the squeezed field, the values shown in the yellow trace in the upper scheme are recorded. An algorithm, equivalent to the one described in [Hua14], can search for the minimum of this trace, representing the squeezed quadrature and lock the phase of the squeezed field correspondingly.

Secondly, instead of low pass filtering the signal that results from mixing the homodyne signal with 5 MHz, it can be bandpass filtered. The center frequency of the bandpass f_{center} can be chosen such that it is within the bandwidth of the data acquisition system used for the lock. If $f_{\mathrm{center}} = f_{\mathrm{sig}} - f_{\mathrm{LO}}$ holds, the local oscillator can be chosen such that the signal that is mixed down to f_{center} corresponds to the noise level at, for example, 5 MHz. This version of the locking scheme has not been tested yet, but the results obtained in [Abd17] indicate that it can successfully be integrated in a compact squeezed-light source.

6.2 Reduction of the external pump power for the generation of squeezed states

In the previous sections, we already described ways to reduce the optical losses and the influence of stray light and thus increase the squeezing strength. 13 dB squeezing were measured with only 12 ± 1 mW of optical pump power at 775 nm in this setup. A modification of the cavity incoupling mirror can reduce this pump power even further. As already described in [Sch18], the buildup factor of the power in the parametric down-conversion cavity is given by:

$$\frac{P_{\mathrm{cav}}}{P_{\mathrm{Pump}}} = \frac{(1 - R_1)}{\left(1 - \sqrt{R_1 R_2 V}\right)^2}. \tag{6.1}$$

R_1 is the power reflectivity of the incoupling mirror and R_2 the power reflectivity of the second cavity mirror, which is the highly reflectively coated backside of the nonlinear crystal in our setup. The propagation efficiency per half cavity roundtrip is given by V and includes all losses from absorption and scattering. From our own measurements and the measurement protocols of the coating company Laseroptik GmbH, we deduce values of $R_1 = 97.5 \pm 0.3\,\%$, $R_2 = 99.955 \pm 0.004\,\%$ and a total transmission of $V = 99.935 \pm 0.05\,\%$ with a contribution of $V_{\mathrm{AR}} = 99.95 \pm 0.05\,\%$ form the antireflective coating of the plane side of the crystal and $V_{\mathrm{KTP}} = 99.985 \pm 0.005\,\%$ resulting from the nonlinear material [Ste13a]. These values result in a power buildup factor of 140, as illustrated in figure 6.3. The blue curve shows how the buildup factor can be increased for larger values of R_1. With $R_1 = 99.8\,\%$, the buildup factor would already increase to 570. Thus, for the same intracavity power, an external pump power that is reduced by a factor of $570/140 \approx 4$ is sufficient. This means that it is feasible to achieve 13 dB squeezing with only 3 mW optical pump power. Optimizing the coatings in our setup even further to values of $R_1 = 99.9\,\%$, $R_2 = 99.98\,\%$ and $V_{\mathrm{AR}} = 99.98\,\%$, resulting in $V = 99.965\,\%$ increases the buildup factor to 1100, allowing for a reduction of the pump power at 775 nm to a value of only 1.5 mW. The red curve in figure 6.3 illustrates this result.

The traces in figure 4.4 were recorded with a local oscillator power of 12 mW at 1550 nm, except for the yellow trace, where we had to reduce the local oscillator power to 1 mW to keep the large anti-squeezing values within the linear regime of the homodyne detector. However, this shows that the required power at 1550 nm is limited by the homodyne detection scheme if the optical pump power for the parametric down-conversion cavity is reduced to 1.5 mW. The local oscillator power can be reduced by

developing electronics with a smaller dark noise level. Our low frequency homodyne detector exhibits a dark noise clearance of more than 20 dB with only 1.15 mW local oscillator power. With further development work, a similar result can be achieved for the MHz regime.
Due to the high conversion efficiency of our second-harmonic generation cavity and the potential to replace the coherent control scheme with a digital locking scheme in combination with further developments regarding the homodyne detector electronics, a compact squeezed-light source that is powered with only 15 mW at 1550 nm seams feasible.

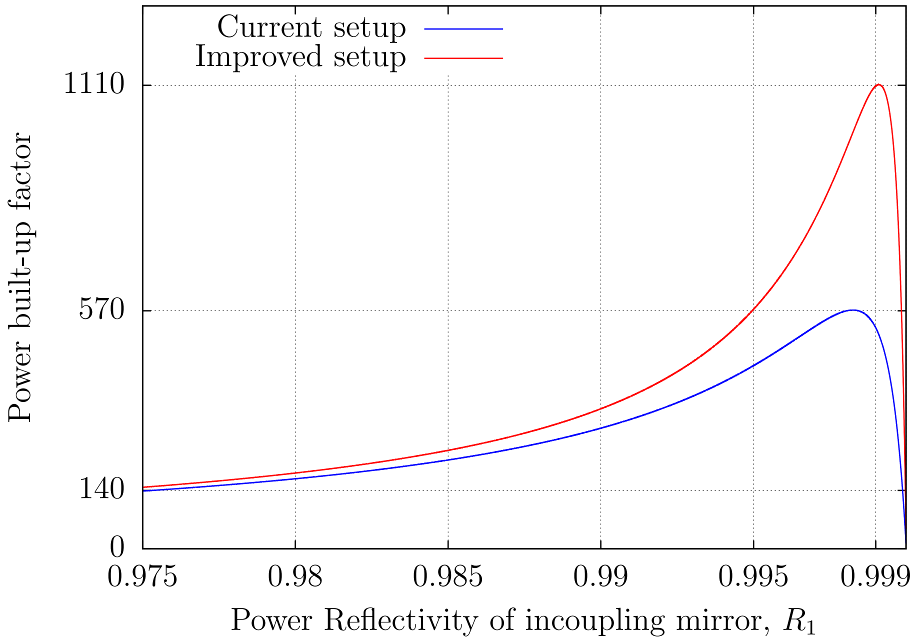

Figure 6.3: The figure illustrates the dependence of the intracavity power buildup of our parametric down-conversion cavity on the power reflectivity of the incoupling mirror for our current setup in blue and a future setup in red. Our setup required 12 ± 1 mW external pump power and produced 13 dB of squeezing with a buildup factor of 140. Simply increasing the power reflectivity of the incoupler already yields a buildup factor of 570, reducing the pump power to 3 mW. Increasing R_1 even further and reducing the intracavity losses with improved coatings increases the buildup factor to 1100 and thus decreases the pump power to only 1.5 mW, as the red curve shows.

7 Summary

Within the past years, sources for squeezed states of light became more and more mature and many different applications have been identified. The first portable and fully automatic source has been designed for the gravitational-wave detector GEO 600 and has successfully been implemented in the detector [Aba11]. Apart from that, squeezing levels of 15 dB have already been achieved [Vah16]. Both of these milestones in squeezing technology were achieved at the wavelength of 1064 nm.
The squeezed-light laser engineered within this project builds on these results and adds to the development of the squeezing technology. To the best of our knowledge, it is the first portable source at 1550 nm. With a footprint of 80 cm x 80 cm, it is the smallest source based on parametric down-conversion that has been built so far. The source is powered with coherent light coupled into the setup via a fiber connector, allowing for a flexible usage with already existing, highly stable laser systems and an easy integration in existing experimental setups. The squeezing level of 13 dB (at 5 MHz) is the strongest squeezing level that has been observed at a telecom wavelength. Apart from that, a multi-temperature scheme was developed and implemented in the second-harmonic generation cavity and the parametric down-conversion cavity for squeezed-light generation. This scheme demonstrates an approach for achieving simultaneous phase matching and double resonance for both the fundamental and second-harmonic wavelength in a linear cavity. A multi-temperature scheme was also developed in parallel by Zielińska and coworkers [Zie17, Zie18].
The squeezing generated with this source can be used for various applications. Squeezing of more than 12 dB can be observed up to a frequency of 10 MHz. This squeezing strength and frequency range allows for the usage of the squeezed-light for quantum key distribution experiments. However, these experiments need entangled states, which can be obtained by combining the squeezed states of two sources on a balanced beam splitter. Apart from that, the source can be used to improve the sensitivity of shot noise limited interferometers or optomechanical experiments in a frequency range from 1 kHz to a few MHz.
Future developments should further improve the technology presented in this thesis. The performance at low frequencies can be improved with higher quality optics, significantly reducing the influence of stray light in the optical paths. Another possibility to reduce the stray light is to increase the electronic gain of the homodyne detector, which reduces the optical local oscillator power that is needed for large dark noise clearance and also reduces the amount of stray light. After these measures have been taken, stray light that leaves the optical path and is scattered back can be reduced by using beam tubes and shields on the breadboard. By increasing the reflectivity for the 775 nm pump field of the incoupler of the squeezing source, the optical pump power

that is needed for the parametric down-conversion cavity that generates the squeezed states can also be reduced, allowing for a setup that works with even less power at 1550 nm. Thus, the experiment can be equipped with low power laser systems, which reduces the cost for squeezed-light sources. The implementation of a digital locking scheme for the phase of the squeezed-light field could reduce the footprint of the source even further. Replacing the acousto-optic modulator and the coherent control scheme by digital locking techniques reduces the number of optical components on the breadboard and enhances the portability and flexibility.
Additional applications of the source could arise from the implementation of these improvements. A better performance at low frequencies could facilitate the application for gravitational-wave detectors that are operated at 1550 nm. In this sense, the setup can be regarded as a proof-of-principle experiment for the integration of squeezing at this wavelength in gravitational-wave detectors that are operated at 1550 nm like the Einstein Telescope. Apart from that, precise reflectivity measurements of the optical components which guide the squeezed state along its path leads to an accurate assignment of the optical losses to each optical surface. Within this thesis, we relied on the specifications of the manufacturer. However, actual measurements allow for an even more accurate loss estimation. With this estimation, the losses which result from the photo diodes can be determined, enabling their absolute calibration at 1550 nm.

Appendix

1 Low frequency homodyne detector

In the following, the schematics of the low frequency homodyne detector that was used for the measurements presented in chapter 5 are depicted. It was developed in cooperation with Fabian Thies during his master thesis. It is combining designs by Henning Vahlbruch and Tobias Gehring. At Hz and kHz frequencies, the resistor that is used for the transimpedance amplifier can couple noise into the measurement. Different resistors were characterized in ([Sei09], p. 74). For our setup, we tried various resistors, but figured that they do not have an influence on the dark noise, especially not at frequencies below 100 Hz. We assume that the increasing noise in this frequency range, visible for example in figure 5.2, results from the operational amplifier.

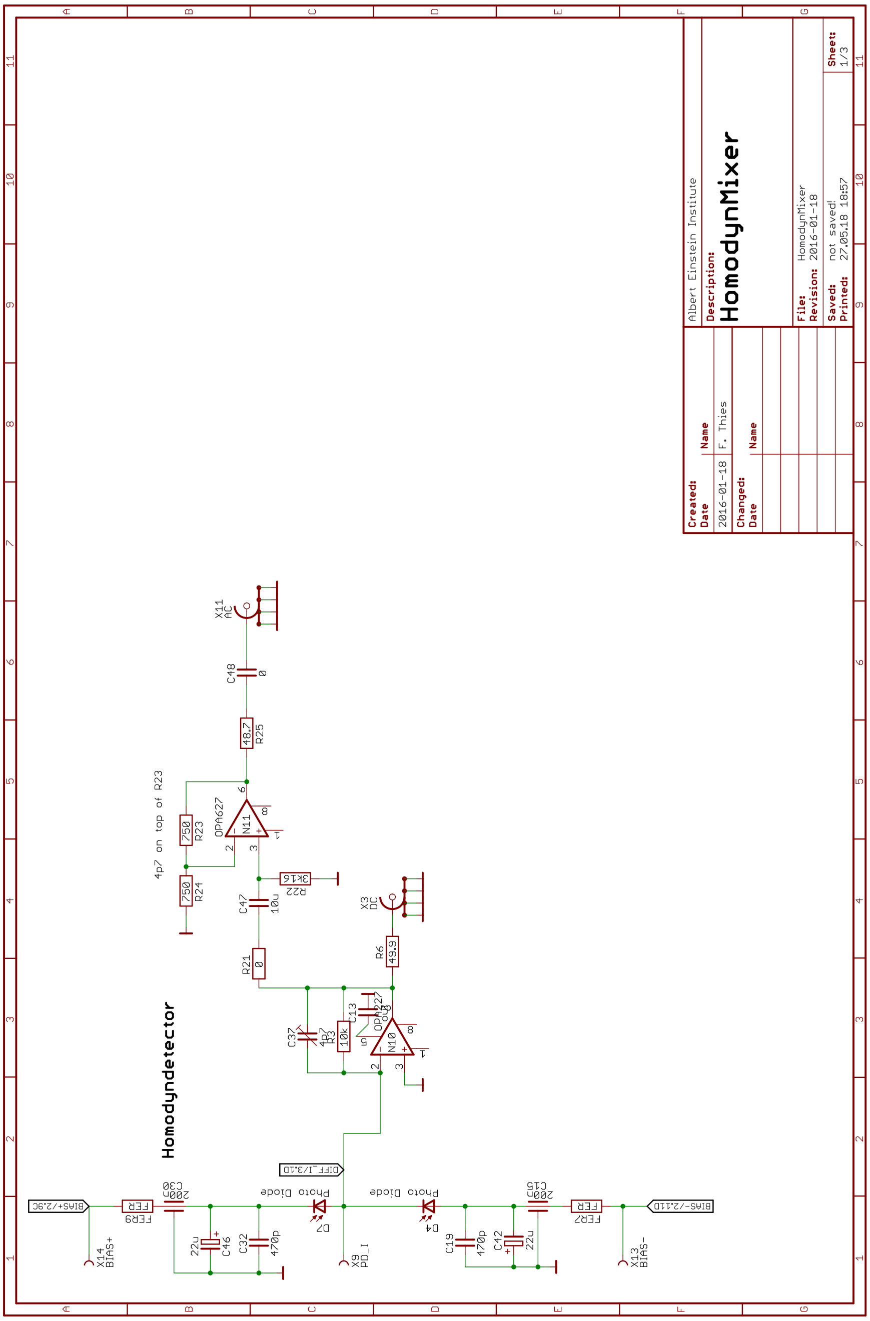

Figure 1: *Project schematics (sheet 1)*

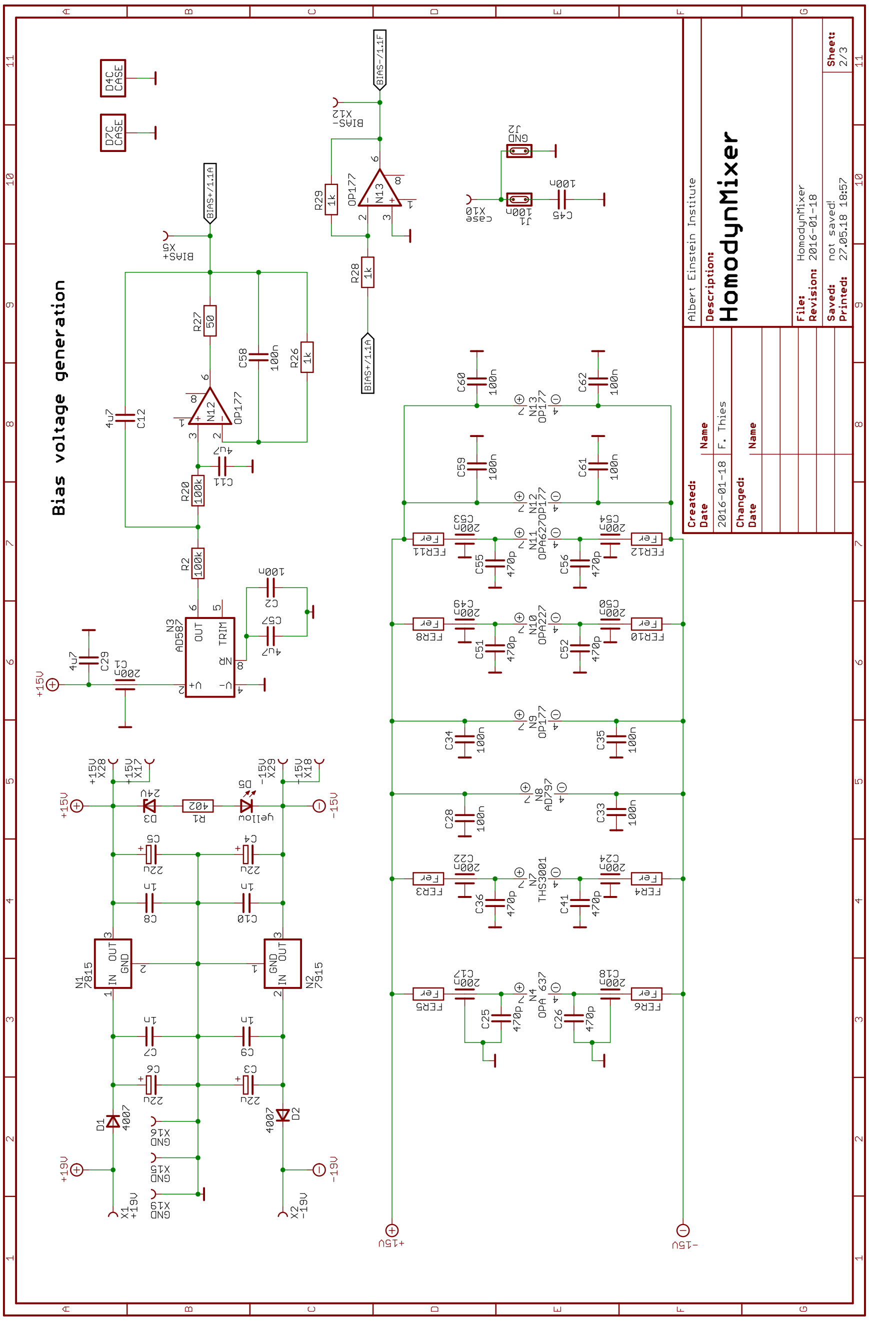

Figure 2: *Project schematics (sheet 2)*

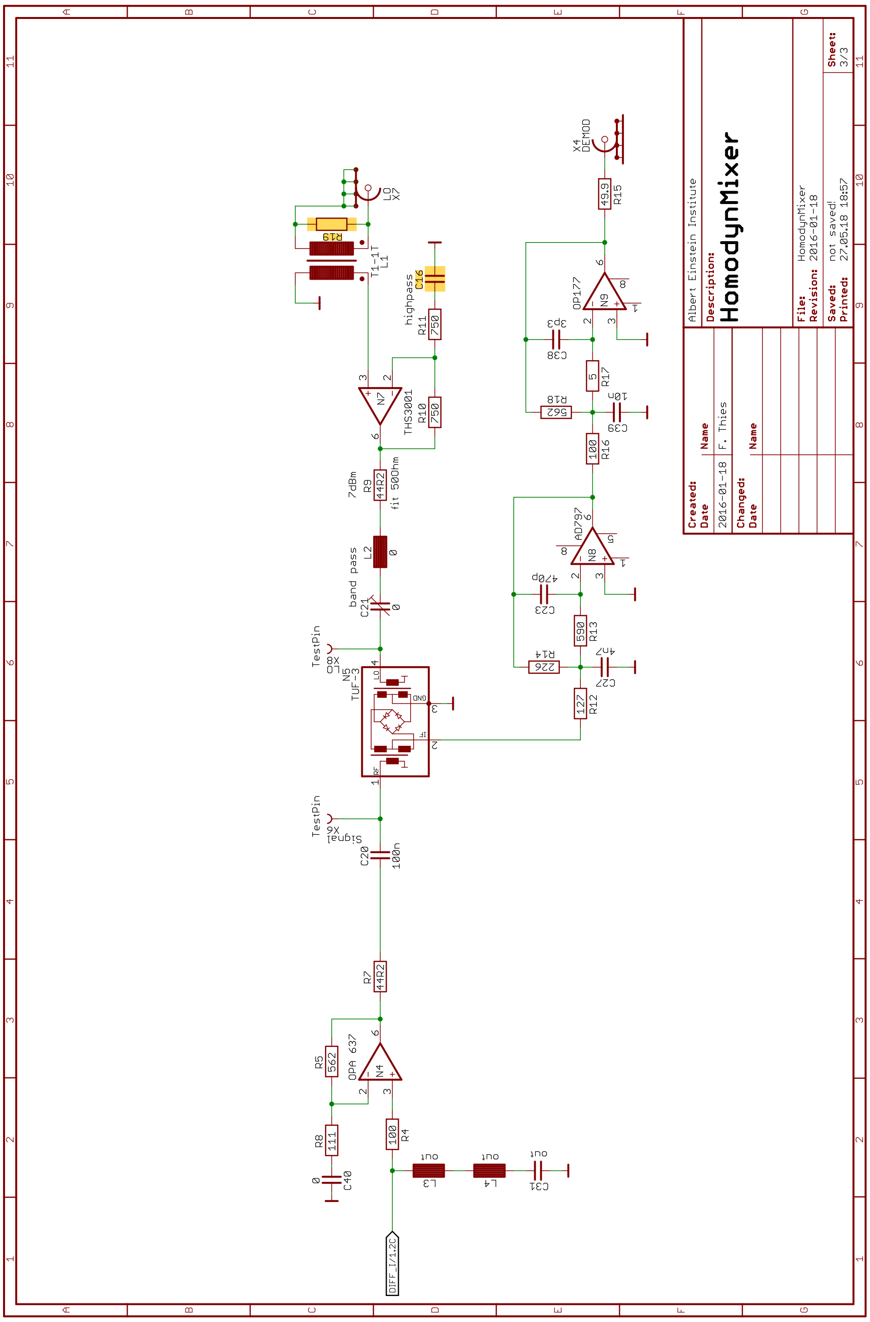

Figure 3: *Project schematics (sheet 3)*
Parts with undefined values are highlighted in orange

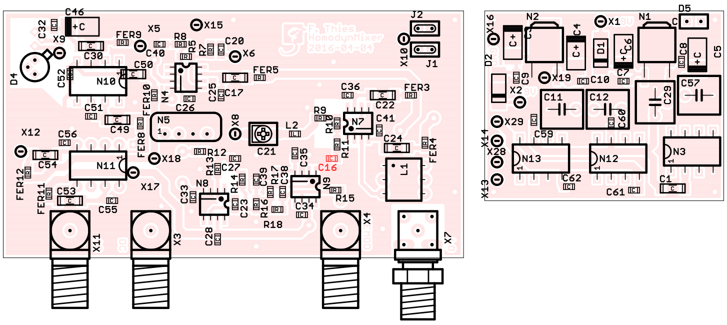

Figure 4: *Board top view showing placeplan with component names*
Components with undefined values are shown in red

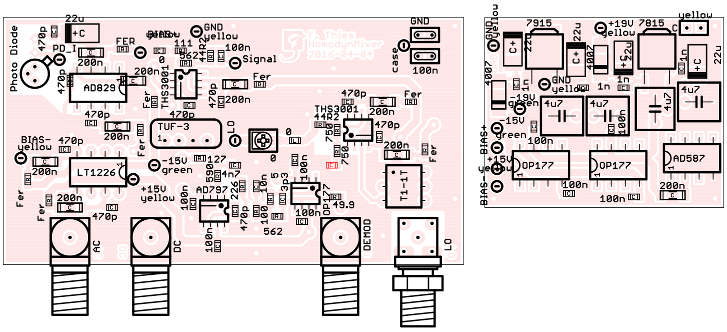

Figure 5: *Board top view showing placeplan with component values*
Components with undefined values are shown in red

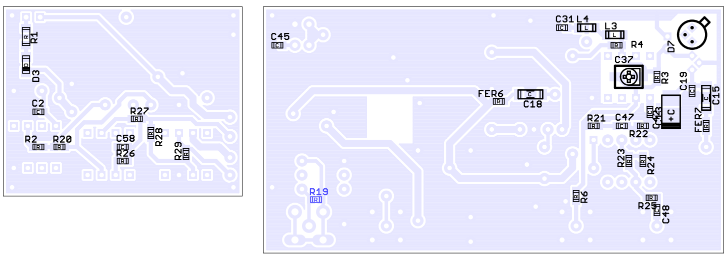

Figure 6: *Board bottom view showing placeplan with component names*
Components with undefined values are shown in blue

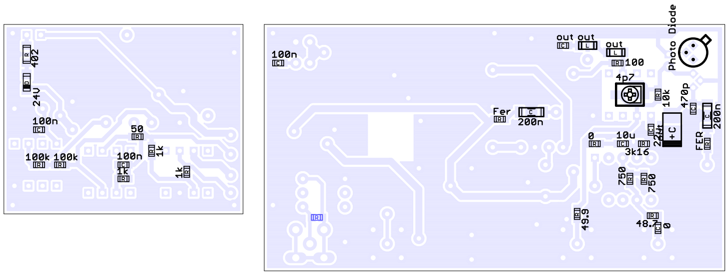

Figure 7: *Board bottom view showing placeplan with component values*
Components with undefined values are shown in blue

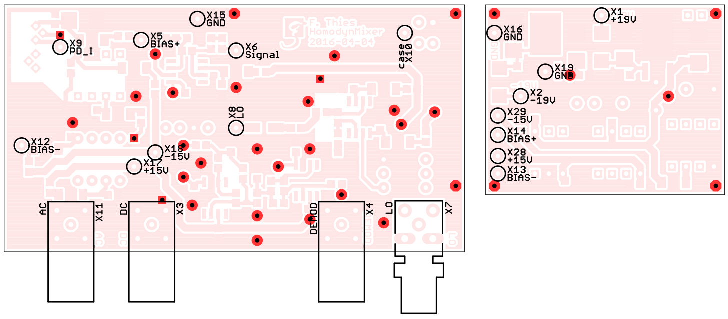

Figure 8: *Board top view showing connectors, test points, vias and wired components*

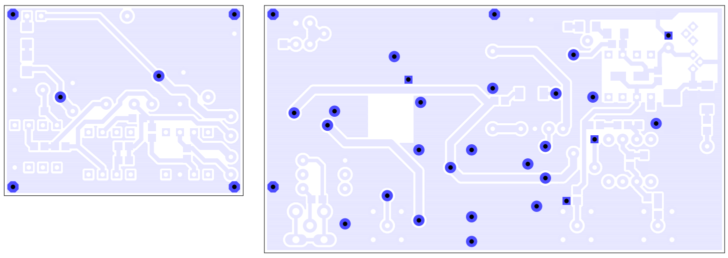

Figure 9: *Board bottom view showing connectors, test points, vias and wired components*

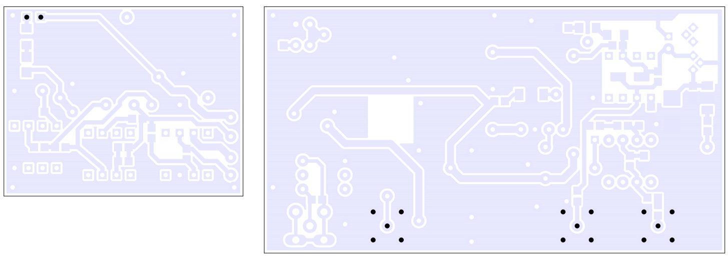

Figure 10: *Board bottom view showing drills with 0.9 mm (0.035 in) diameter*

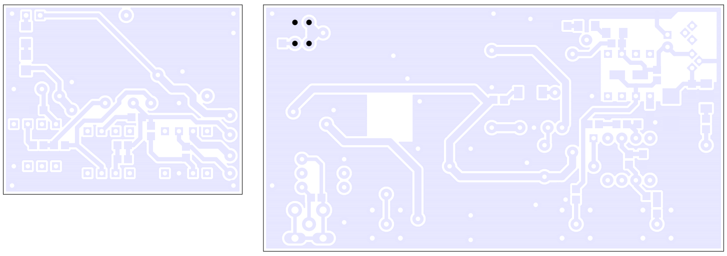

Figure 11: *Board bottom view showing drills with 1.0 mm (0.039 in) diameter*

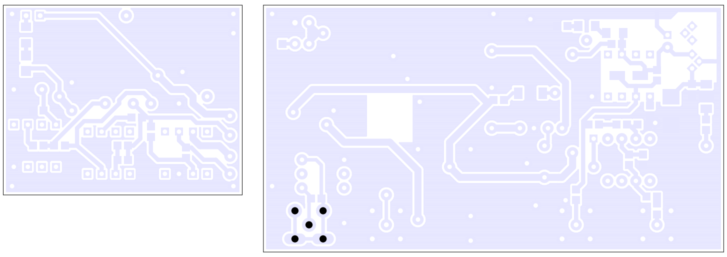

Figure 12: *Board bottom view showing drills with 1.3 mm (0.051 in) diameter*

Resources

The work presented in this thesis was done with the help of different computer programs. Three dimensional and technical drawings of custom made mechanical components like the linear filter cavities were made with Autodesk Inventor. Different versions from 2012 – 2016 were used. Electronics were designed with Eagle 6.6.0 and earlier versions using the component library of Andreas Weidner from the Albert Einstein Institute in Hannover. Simulations and calculations for this project were performed with Wolfram Mathematica 9 and Matlab R2014a. Apart from that, Python 3.5.2, which was run on the development environment Spyder 2.3.9 and in combination with jupyter, was used. Simulations regarding the optical design of the setup were done with N.L.C.S by Nico Lastzka [Las10] and Finesse by Andreas Freise [Fre18]. JamMT version 0.24, programmed by André Thüring and Nico Lastzka [Las10], was used for mode matching simulations. Microsoft Excel 2010 was also made use of. The schematic drawings in this thesis were done with Inkscape 0.91 and the component library designed by Alexander Franzen and Jan Gniesmer. Plots were generated with Gnuplot 5.0 and the thesis was written using MiKTeX 2.9 in conjunction with TeXnicCenter 2.02.
Electronic designs for standard components of a quantum optical experiment such as photodiodes, servos, high-voltage amplifiers, frequency generators, temperature controllers and peltier drivers, electro-optic modulators and drivers for the acousto-optic modulator existed within the group. They were made by Henning Vahlbruch, Sebastian Steinlechner, Tobias Gehring and Andreas Weidner. The electronic components on these boards were adapted to the needs of the experimental setup presented here.

Acknowledgements

The work presented in this thesis would not have been possible without the help and support of many people.
I thank my supervisor Prof. Dr. Roman Schnabel for offering me this topic and supporting and encouraging me during the entire project.
I would also like to thank all the people I worked with during my PhD studies for their help, fruitful discussions and fun times.
I am also grateful for my family and friends. Thanks for supporting me in everything I do, taking me through the rough times and enjoying the good ones with me!

Eidesstattliche Versicherung/Declaration on oath

Hiermit versichere ich an Eides statt, die vorliegende Dissertationsschrift selbst verfasst und keine anderen als die angegebenen Hilfsmittel und Quellen benutzt zu haben.

Die eingereichte schriftliche Fassung entspricht der auf dem elektronischen Speichermedium.

Die Dissertation wurde in der vorgelegten oder einer ähnlichen Form nicht schon einmal in einem früheren Promotionsverfahren angenommen oder als ungenügend beurteilt.

Hamburg, den

Unterschrift des Doktoranden

List of Figures

1.1 Illustration of a shot noise limited electric field 1

2.1 Wigner function of a coherent and a vacuum state 9
2.2 Coherent state and vacuum state in phase space 12
2.3 Squeezed state in phase space 13
2.4 Photon number distribution of squeezed vacuum states 14
2.5 Nonlinear processes of second-harmonic generation and parametric down-conversion 15
2.6 Schematic of second-harmonic generation 15
2.7 Conversion in second-harmonic generation 18
2.8 Model of squeezing cavity 21
2.9 Squeezing spectra 28
2.10 Model of optical losses 29
2.11 Squeezing spectra with losses 30
2.12 Domain structure of periodically poled nonlinear crystal 31
2.13 Frequency conversion with quasi phase matching 32

3.1 Photograph of the experimental setup 33
3.2 Schematics of the experimental setup 35
3.3 Three dimensional drawing of the linear filter cavity and photograph . 36
3.4 Bode plot of open loop gain measurements of the filter cavities 37
3.5 Three dimensional drawing of the nonlinear cavity and the incoupler . . 39
3.6 Calculation of the waist position and size in the nonlinear crystal . . . 40
3.7 Three dimensional drawing of the heating unit within the nonlinear cavity 41
3.8 Photograph of the nonlinear cavity with the crystal 42
3.9 Bode plot of the open loop gain of the nonlinear cavities 43
3.10 Second-harmonic generation conversion efficiency 44
3.11 Second-harmonic generation temperature settings 45
3.12 Optical parametric oscillation in high conversion efficiency second-harmonic generation 46
3.13 Homodyne detection scheme 47
3.14 Energy level diagram of single sideband interaction 50
3.15 Single sideband interaction in the coherent control scheme 52
3.16 Coherent control error signals 53
3.17 Bode plot of the open loop gain of the coherent control locks 54

4.1 Linearity of Homodyne detector at 5 MHz 55
4.2 13dB squeezing zero span measurement 56

4.3 Linearity of homodyne detector between 3 MHz and 25 MHz 57
4.4 Pump power dependant squeezing spectra 58
4.5 Phase noise estimation 61

5.1 Laser noise and balanced homodyne system 64
5.2 Low frequency homodyne detector, dependence of shot noise power on local oscillator power 65
5.3 Low frequency homodyne detector linearity 66
5.4 Homodyne detector with stray light 67
5.5 Low frequency squeezing spectrum 69
5.6 Dark noise corrected low frequency squeezing spectrum with 10 dB . . . 70
5.7 Dark noise corrected low frequency squeezing spectrum with 8.54 dB . . 71
5.8 Dark noise corrected low frequency squeezing spectrum with 7.74 dB . . 72
5.9 Squeezing spectrum below 1 kHz 74
5.10 Dark noise corrected squeezing spectrum below 1 kHz 75

6.1 Setup with digital lock for the squeezed quadrature 78
6.2 Locking algorithm for squeezed states 80
6.3 Power buildup in parametric down-conversion cavity 82

Bibliography

[Aas13] J. Aasi *et al.*, *Enhanced sensitivity of the LIGO gravitational wave detector by using squeezed states of light*, Nature Photonics **7**, 613 (2013).

[Aba11] J. Abadie *et al.*, *A gravitational wave observatory operating beyond the quantum shot-noise limit*, Nature Physics **7**, 962 (2011).

[Abb16] B. P. Abbott *et al.*, *Observation of gravitational waves from a binary black hole merger*, Phys. Rev. Lett. **116**, 061102 (2016).

[Abd17] D. Abdelkhalek, *Efficient entanglement distillation based on emulation*, Ph.D. thesis, Gottfried Wilhelm Leibniz Universität Hannover (2017).

[Abe11] M. Abernathy *et al.*, *Einstein gravitational wave telescope conceptual design study*, Online (2011), `https://tds.virgo-gw.eu/?call_file=ET-0106C-10.pdf` visited on march 3rd, 2018.

[And16] U. L. Andersen, T. Gehring, C. Marquardt, and G. Leuchs, *30 years of squeezed light generation*, Physica Scripta **91**, 053001 (2016).

[Aok06] T. Aoki, G. Takahashi, and A. Furusawa, *Squeezing at 946nm with periodically poled* $KTiOPO_4$, Optics Express **14**, 6930 (2006).

[Ast11] S. Ast, R. M. Nia, A. Schönbeck, N. Lastzka, J. Steinlechner, T. Eberle, M. Mehmet, S. Steinlechner, and R. Schnabel, *High-efficiency frequency doubling of continuous-wave laser light*, Opt. Lett. **36**, 3467 (2011).

[Ast12] S. Ast, A. Samblowski, M. Mehmet, S. Steinlechner, T. Eberle, and R. Schnabel, *Continuous-wave nonclassical light with gigahertz squeezing bandwidth*, Opt. Lett. **37**, 2367 (2012).

[Ast13] S. Ast, M. Mehmet, and R. Schnabel, *High-bandwidth squeezed light at 1550 nm from a compact monolithic PPKTP cavity*, Opt. Express **21**, 13572 (2013).

[Bac04] H.-A. Bachor and T. Ralph, *A Guide to Experiments in Quantum Optics*, Willey-VCH (2004).

[Bas14] M. Bassan, *Advanced Interferometers and the Search for Gravitational Waves*, Springer (2014).

[Bau15] C. Baune, J. Gniesmer, A. Schönbeck, C. E. Vollmer, J. Fiurášek, and R. Schnabel, *Strongly squeezed states at 532 nm based on frequency up-conversion*, Optics Express **23**, 16035 (2015).

[Bau16] C. Baune, *Frequency up-conversion of nonclassical states of light*, Ph.D. thesis, Gottfried Wilhelm Leibniz Universität Hannover (2016).

[Bla01] E. D. Black, *An introduction to Pound–Drever–Hall laser frequency stabilization*, American Journal of Physics **69**, 79 (2001).

[Boy08] R. Boyd, *Nonlinear Optics*, Academic Press (2008).

[Cav81] C. M. Caves, *Quantum-mechanical noise in an interferometer*, Phys. Rev. D **23**, 1693 (1981).

[Che07a] S. Chelkowski, *Squeezed Light and Laser Interferometric Gravitational Wave Detectors*, Ph.D. thesis, Gottfried Wilhelm Leibniz Universität Hannover (2007).

[Che07b] S. Chelkowski, H. Vahlbruch, K. Danzmann, and R. Schnabel, *Coherent control of broadband vacuum squeezing*, Phys. Rev. A **75**, 043814 (2007).

[Col84] M. Collett and C. Gardiner, *Squeezing of intracavity traveling-wave light fields produced in parametric amplification*, Physical Review A **30**, 1386 (1984).

[Dem06] W. Demtröder, *Experimentalphysik 2*, Springer (2006).

[Dre83] R. W. P. Drever, J. L. Hall, F. V. Kowalski, J. Hough, G. M. Ford, A. J. Munley, and H. Ward, *Laser phase and frequency stabilization using an optical resonator*, Applied Physics B **31**, 97 (1983).

[Dru14] P. Drummond and M. Hillery, *The Quantum Theory of Nonlinear Optics*, Cambridge University Press (2014).

[Dwy13] S. Dwyer *et al.*, *Squeezed quadrature fluctuations in a gravitational wave detector using squeezed light*, Opt. Express **21**, 19047 (2013).

[Ebe13] T. Eberle, *Realization of Finite-Size Quantum Key Distribution based on Einstein-Podolsky-Rosen Entangled Light*, Ph.D. thesis, Gottfried Wilhelm Leibniz Universität Hannover (2013).

[Fej92] M. M. Fejer, G. A. Magel, D. H. Jundt, and R. L. Byer, *Quasi-phase-matched second harmonic generation: tuning and tolerances*, IEEE Journal of Quantum Electronics **28**, 2631 (1992).

[Fre18] A. Freise, *Finesse 2*, Website (2018), online `http://www.gwoptics.org/finesse/` visited on may 25th, 2018.

[Fur15] A. Furusawa, *Quantum States of Light*, Springer (2015).

[Gar85] C. Gardiner and M. Collett, *Input and output in damped quantum systems: Quantum stochastic differential equations and the master equation*, Physical Review A **31**, 3761 (1985).

[Geh15] T. Gehring, V. Händchen, J. Duhme, F. Furrer, T. Franz, C. Pacher, R. F. Werner, and R. Schnabel, *Implementation of continuous-variable quantum key distribution with composable and one-sided-device-independent security against coherent attacks*, Nature Communications **6**, 8795 (2015).

[Ger05] C. Gerry and P. Knight, *Intorductory Quantum Optics*, Cambridge University Press (2005).

[Gro13] H. Grote, K. Danzmann, K. L. Dooley, R. Schnabel, J. Slutsky, and H. Vahlbruch, *First long-term application of squeezed states of light in a gravitational-wave observatory*, Phys. Rev. Lett. **110**, 181101 (2013).

[Hei27] W. Heisenberg, *Über den anschaulichen Inhalt der quantentheoretischen Kinematik und Mechanik*, Zeitschrift für Physik **43**, 172 (1927).

[Hua14] K. Huang *et al.*, *Microcontroller-based locking in optics experiments*, Review of Scientific Instruments **85**, 123112 (2014).

[Ime98] G. Imeshev, M. Proctor, and M. M. Fejer, *Phase correction in double-pass quasi-phase-matched second-harmonic generation with a wedged crystal*, Opt. Lett. **23**, 165 (1998).

[Kau13] H. Kaufer, *Opto-mechanics in a Michelson-Sagnac interferometer*, Ph.D. thesis, QUEST-Leibniz-Forschungsschule der Gottfried Wilhelm Leibniz Universität Hannover (2013).

[Kha11] A. Khalaidovski, *Beyond the Quantum Limit - A Squeezed-Light Laser in GEO 600*, Ph.D. thesis, Gottfried Wilhelm Leibniz Universität Hannover (2011).

[Kha12] A. Khalaidovski, H. Vahlbruch, N. Lastzka, C. Gräf, K. Danzmann, H. Grote, and R. Schnabel, *Long-term stable squeezed vacuum state of light for gravitational wave detectors*, Classical and Quantum Gravity **29**, 075001 (2012).

[Kni18] B. Knispel and H. Lück, *Hannoveraner Spitzentechnologie für Gravitationswellendetektor Virgo in Italien*, Website (2018), online `https://www.aei.mpg.de/2202087/virgo-squeezer` visited on february 27th, 2018.

[Las07] N. Lastzka and R. Schnabel, *The Gouy phase shift in nonlinear interactions of waves*, Optics Express **15**, 7211 (2007).

[Las10] N. Lastzka, *Numerical modelling of classical and quantum effects in nonlinear optical systems*, Ph.D. thesis, Gottfried Wilhelm Leibniz Universität Hannover (2010).

[Leo97] U. Leonhardt, *Measuring the Quantum State of Light*, Cambridge University Press (1997).

[Leo16] M. Leonardi, *Development of a squeezed light source prototype for Advanced Virgo*, Ph.D. thesis, University of Trento (2016).

[Lou87] R. Loudon and P. Knight, *Squeezed Light*, Journal of Modern Optics **34**, 709 (1987).

[Mü17] A. Müller, *10 Dinge, die Sie über Gravitationswellen wissen wollen*, Springer (2017).

[McK04] K. McKenzie, N. Grosse, W. P. Bowen, S. E. Whitcomb, M. B. Gray, D. E. McClelland, and P. K. Lam, *Squeezing in the audio gravitational-wave detection band*, Phys. Rev. Lett. **93**, 161105 (2004).

[McK06] K. McKenzie, M. B. Gray, S. Goßler, P. K. Lam, and D. E. McClelland, *Squeezed state generation for interferometric gravitational-wave detection*, Classical and Quantum Gravity **23**, S245 (2006).

[McK07] K. McKenzie, M. B. Gray, P. K. Lam, and D. E. McClelland, *Technical limitations to homodyne detection at audio frequencies*, Appl. Opt. **46**, 3389 (2007).

[Meh11] M. Mehmet, S. Ast, T. Eberle, S. Steinlechner, H. Vahlbruch, and R. Schnabel, *Squeezed light at 1550 nm with a quantum noise reduction of 12.3 dB*, Opt. Express **19**, 25763 (2011).

[Meh12] M. Mehmet, *Squeezed light at 1064 nm and 1550 nm with a nonclassical noise suppression beyond 10 dB*, Ph.D. thesis, Gottfried Wilhelm Leibniz Universität Hannover (2012).

[Mey07] P. Meystre and M. Sargent III, *Elements of Quantum Optics*, Springer (2007).

[Mik06] E. E. Mikhailov, K. Goda, and N. Mavalvala, *Noninvasive measurements of cavity parameters by use of squeezed vacuum*, Phys. Rev. A **74**, 033817 (2006).

[NN08] J. S. Neegaard-Nielsen, *Generation of single photons and Schrödinger kitten states of light*, Ph.D. thesis, University of Copenhagen (2008).

[Oel16] E. Oelker, G. Mansell, M. Tse, J. Miller, F. Matichard, L. Barsotti, P. Fritschel, D. E. McClelland, M. Evans, and N. Mavalvala, *Ultra-low phase noise squeezed vacuum source for gravitational wave detectors*, Optica **3**, 682 (2016).

[Pea99] S. Pearl, H. Lotem, Y. Shimony, and S. Rosenwaks, *Optimization of laser intracavity second-harmonic generation by a linear dispersion element*, J. Opt. Soc. Am. B **16**, 1705 (1999).

[Rau11] C. Rauscher, *Grundlagen der Spektrumanalyse*, Rohde & Schwarz GmbH & Co. KG (2011).

[Saw17] A. Sawadsky, *Optomechanical Coupling in an Interferometer with a SiN-Membrane*, Ph.D. thesis, Gottfried Wilhelm Leibniz Universität Hannover (2017).

[Sch06] H. Schulz, *Physik mit Bleistift*, Verlag Harri Deutsch (2006).

[Sch07] F. Schwabel, *Quantenmechanik (QM1)*, Springer (2007).

[Sch17] R. Schnabel, *Squeezed states of light and their applications in laser interferometers*, Physics Reports **684**, 1 (2017).

[Sch18] A. Schönbeck, F. Thies, and R. Schnabel, *13 dB squeezed vacuum states at 1550 nm from 12 mW external pump power at 775 nm*, Optics Letters **43**, 110 (2018).

[Scu97] M. Scully and M. Zubairy, *Quantum Optics*, Cambridge University Press (1997).

[Sei09] F. Seifert, *Power Stabilization of High Power Lasers for Second Generation Gravitational Wave Detectors*, Ph.D. thesis, Gottfried Wilhelm Leibniz Universität Hannover (2009).

[Slu85] R. E. Slusher, L. W. Hollberg, B. Yurke, J. C. Mertz, and J. F. Valley, *Observation of squeezed states generated by four-wave mixing in an optical cavity*, Phys. Rev. Lett. **55**, 2409 (1985).

[Spa11] H. M. Sparkes *et al.*, *A scalable, self-analyzing digital locking system for use on quantum optics experiments*, Review of Scientific Instruments **82**, 075113 (2011).

[Ste11] M. Stefszky, C. M. Mow-Lowry, K. McKenzie, S. Chua, B. C. Buchler, T. Symul, D. E. McClelland, and P. K. Lam, *An investigation of doubly-resonant optical parametric oscillators and nonlinear crystals for squeezing*, Journal of Physics B: Atomic, Molecular and Optical Physics **44**, 015502 (2011).

[Ste12] M. S. Stefszky *et al.*, *Balanced homodyne detection of optical quantum states at audio-band frequencies and below*, Class. Quantum Grav. **29**, 145015 (2012).

[Ste13a] J. Steinlechner, S. Ast, C. Krüger, A. P. Singh, T. Eberle, V. Händchen, and R. Schnabel, *Absorption Measurements of Periodically Poled Potassium Titanyl Phosphate (PPKTP) at 775 nm and 1550 nm*, Sensors (Basel, Switzerland) **13**, 565 (2013).

[Ste13b] S. Steinlechner, *Quantum metrology with squeezed and entangled light for the detection of gravitational waves*, Ph.D. thesis, Gottfried Wilhelm Leibniz Universität Hannover (2013).

[Tay13] M. A. Taylor *et al.*, *Biological measurement beyond the quantum limit*, Nature Photonics **7**, 229 (2013).

[The11] The LIGO Scientific Collaboration, *A gravitational wave observatory operating beyond the quantum shot-noise limit: Squeezed light in application*, Nature Physics **7**, 962 (2011).

[Vah07] H. Vahlbruch, S. Chelkowski, K. Danzmann, and R. Schnabel, *Quantum engineering of squeezed states for quantum communication and metrology*, New Journal of Physics **9**, 371 (2007).

[Vah08a] H. Vahlbruch, *Squeezed Light for Gravitational Wave Astronomy*, Ph.D. thesis, Gottfried Wilhelm Leibniz Universität Hannover (2008).

[Vah08b] H. Vahlbruch, M. Mehmet, S. Chelkowski, B. Hage, A. Franzen, N. Lastzka, S. Goßler, K. Danzmann, and R. Schnabel, *Observation of squeezed light with 10-dB quantum-noise reduction*, Phys. Rev. Lett. **100**, 033602 (2008).

[Vah10] H. Vahlbruch, A. Khalaidovski, N. Lastzka, C. Gräf, K. Danzmann, and R. Schnabel, *The GEO600 squeezed light source*, Classical and Quantum Gravity **27**, 084027 (2010).

[Vah16] H. Vahlbruch, M. Mehmet, K. Danzmann, and R. Schnabel, *Detection of 15 dB squeezed states of light and their application for the absolute calibration of photoelectric quantum efficiency*, Phys. Rev. Lett. **117**, 110801 (2016).

[Vol13] C. E. Vollmer, *Non-Classical State Engineering for Quantum Networks*, Ph.D. thesis, Gottfried Wilhelm Leibniz Universität Hannover (2013).

[Wad15] A. R. Wade, G. L. Mansell, S. S. Y. Chua, R. L. Ward, B. J. J. Slagmolen, D. A. Shaddock, and D. E. Mcclelland, *A squeezed light source operated under high vacuum*, Scientific Reports **5**, 18052 (2015).

[Wad16] A. Wade, *Quantum Limited Measurements in Gravitational Wave Detectors*, Ph.D. thesis, The Australian National University (2016).

[Wal08] D. Walls and G. Milburn, *Quantum Optics*, Springer (2008).

[Wil98] B. Willke, N. Uehara, E. K. Gustafson, R. L. Byer, P. J. King, S. U. Seel, and R. L. Savage, *Spatial and temporal filtering of a 10-W Nd:YAG laser with a Fabry–Perot ring-cavity premode cleaner*, Opt. Lett. **23**, 1704 (1998).

[Win91] W. Winkler, K. Danzmann, A. Rüdiger, and R. Schilling, *Heating by optical absorption and the performance of interferometric gravitational-wave detectors*, Phys. Rev. A **44**, 7022 (1991).

[Wu86] L.-A. Wu, H. J. Kimble, J. L. Hall, and H. Wu, *Generation of squeezed states by parametric down conversion*, Phys. Rev. Lett. **57**, 2520 (1986).

[Zie17] J. A. Zielińska, A. Zukauskas, C. Canalias, M. A. Noyan, and M. W. Mitchell, *Fully-resonant, tunable, monolithic frequency conversion as a coherent UVA source*, Optics Express **25**, 1142 (2017).

[Zie18] J. A. Zielińska and M. W. Mitchell, *Atom-resonant squeezed light from a tunable monolithic ppRKTP parametric amplifier*, Opt. Lett. **43**, 643 (2018).